Galaxy And Mass Assembly (GAMA): deconstructing the galaxy stellar mass function in the low-redshift Universe

Dissertation

zur Erlangung des Doktorgrades
an der Fakultät für Mathematik, Informatik und Naturwissenschaften
Fachereich Physik
der Universität Hamburg

vorgelegt von

Antonio Sbaffoni

Hamburg
2025

Gutachter der Dissertation:	Prof. Dr. Jochen Liske Prof. Dr. Aaron S. G. Robotham
Zusammensetzung der Prüfungskommission:	Prof. Dr. Jochen Liske Prof. Dr. Aaron S. G. Robotham Prof. Dr. Marcus Brüggen Prof. Dr. Peter H. Hauschildt Prof. Dr. Jan-Torge Schindler
Vorsitzender der Prüfungskommission:	Prof. Dr. Peter H. Hauschildt
Datum der Disputation:	05.12.2025
Vorsitzender des Fach-Promotionsausschusses PHYSIK:	Prof. Dr. Wolfgang J. Parak
Leiter des Fachbereichs PHYSIK:	Prof. Dr. Markus Drescher
Dekan der Fakultät MIN:	Prof. Dr.-Ing. Norbert Ritter

Declaration on oath

I hereby declare and affirm that this doctoral dissertation is my own work and that I have not used any aids and sources other than those indicated.
If electronic resources based on generative artificial intelligence (gAI) were used in the course of writing this dissertation, I confirm that my own work was the main and value-adding contribution and that complete documentation of all resources used is available in accordance with good scientific practice. I am responsible for any erroneous or distorted content, incorrect references, violations of data protection and copyright law or plagiarism that may have been generated by the gAI.

Hamburg, den 03.10.2025

Antonio Sbaffoni

Zusammenfassung

In dieser Doktorarbeit dekonstruieren wir die stellare Massenfunktion von Galaxien (GSMF) im niedrig-rotverschobenen Universum unter Verwendung der Daten der Galaxy and Mass Assembly (GAMA) Durchmusterung. Insbesondere untersuchen wir, wie sich die GSMF in Abhängigkeit von der großräumigen Struktur (z.B. Gruppen, Filamente und Voids), der Halomasse und der Galaxienpopulation (sternbildende vs. passive Galaxien, Zentral- vs. Satellitengalaxien) verändert. Zu diesem Zweck verwenden wir die Modified Maximum Likelihood (MML) Methode, einen bayesschen Ansatz zur Anpassung von Verteilungsfunktionen ohne Binning, wobei Messfehler, Selektionseffekte und großräumige Strukturen berücksichtigt werden.

Aus einer sorgfältig ausgewählten Stichprobe von 52 089 Galaxien und 10 429 Gruppen untersuchen wir zunächst die Veränderung der GSMF im niedrig-rotverschobenen Universum als Funktion von vier verschiedenen Umgebungseigenschaften, nämlich der orthogonalen Entfernung zum nächsten Filament, der Gruppenzugehörigkeit, der Halomasse der Gruppe, und einer Kombination aus der Zweigordnung der Gruppe sowie der Anzahl der Verbindungen der Gruppe. Wir stellen Folgendes fest: (i) Die GSMF wird nicht signifikant von der Entfernung zum nächsten Filament beeinflusst, sondern vielmehr von der Gruppenzugehörigkeit. (ii) Massereichere Halos beherbergen tendenziell massereichere Galaxien und zeigen eine steileren Abhängigkeit der Anzahl mittelgroßer Galaxien von der Sternmasse. Dieses Ergebnis ist robust gegenüber der Wahl dynamischer und leuchtkraftbasierter Messungen der Gruppenhalomasse. (iii) Die GSMF von Gruppengalaxien hängt nicht von der Position innerhalb eines Filaments ab, aber für Gruppen außerhalb von Filamenten ist die charakteristische Masse der GSMF geringer. Schließlich lässt sich unsere globale GSMF gut durch eine doppelte Schechter-Funktion mit den folgenden Parametern beschreiben: $\log[M^\star/(M_\odot\, h_{70}^{-2})] = 10.76 \pm 0.01$, $\Phi_1^\star = (3.75 \pm 0.09) \times 10^{-3}$ Mpc^{-3} h_{70}^3, $\alpha_1 = -0.86 \pm 0.03$, $\Phi_2^\star = (0.13 \pm 0.05) \times 10^{-3}$ Mpc^{-3} h_{70}^3 and $\alpha_2 = -1.71 \pm 0.06$. Dieses Ergebnis ist in Bezug auf $M^\star$ mit früheren GAMA-Studien konsistent, wenngleich wir für α_1 und α_2 niedrigere Werte finden.

Wir dekonstruieren die GSMF im niedrig-rotverschobenen Universum weiter, indem wir Galaxien nach ihrer Sternentstehungsaktivität und Umgebung trennen und untersuchen, wie sie sich über verschiedene Galaxienpopulationen (sternbildende vs. passive Galaxien sowie Zentral- vs. Satellitengalaxien) und in Abhängigkeit von der Halomasse verändert. Wir stellen Folgendes fest: (i) Die GSMFs passiver und sternbildender Galaxien lassen sich gut durch eine doppelte bzw. eine einfache Schechter-Funktion beschreiben, wenngleich die Einbeziehung einer zweiten Komponente für die sternbildende Population eine genauere Beschreibung ermöglicht. Darüber hinaus dominieren sternbildende Galaxien das niedrige Massenende der gesamten GSMF, während passive Galaxien hauptsächlich den mittleren bis hohen Massenbereich prägen. (ii) Die GSMF von Zentralgalaxien dominiert das hohe Massenende, während Satelliten und nicht gruppierte Galaxien den mittleren bis niedrigen Massenbereich prägen. Zudem stellen wir einen relativen

Anstieg der Häufigkeit von Galaxien niedriger Masse fest, wenn man von dichten Gruppenumgebungen zu isolierten Systemen übergeht. (iii) Massereichere Halos beherbergen massereichere Galaxien, weisen einen höheren Anteil passiver Systeme auf und zeigen einen steileren Rückgang der Anzahl von Galaxien mittlerer Masse. Schließlich zeigen unsere Ergebnisse größere Unterschiede zwischen passiven und sternbildenden GSMFs als vom Modell von Peng et al. (2010) vorhergesagt, bestätigen jedoch im Allgemeinen die in anderen Arbeiten berichteten Trends der mit der Umgebung assoziierten Verminderung von Sternentstehungsaktivität von Zentral- und Satellitengalaxien.

Abstract

In this doctoral thesis, we deconstruct the galaxy stellar mass function (GSMF) in the low-redshift Universe using the equatorial Galaxy and Mass Assembly (GAMA) dataset. Specifically, we explore how the GSMF varies as a function of the large-scale structure (e.g. groups, filaments, and voids), halo mass, and galaxy population (e.g. star-forming vs passive galaxies, centrals vs satellites). To this end, we employ the Modified Maximum Likelihood (MML) method, a Bayesian approach to fitting distribution functions without binning, while accounting for measurement errors, selection effects, and large-scale structure.

From a carefully selected sample of 52 089 galaxies and 10 429 groups, we first investigate the variation of the low-redshift GSMF as a function of four different environmental properties, namely the orthogonal distance to the nearest filament, group membership, group halo mass, and a combination of the group's branch order and the group's number of connecting links. We find that: (i) The GSMF is not strongly affected by distance to the nearest filament, but rather by group membership. (ii) More massive halos tend to host more massive galaxies and exhibit a steeper decline with stellar mass in the number of intermediate-mass galaxies. This result is robust against the choice of dynamical and luminosity-based group halo mass estimates. (iii) The GSMF of group galaxies does not depend on the position within a filament, but for groups outside of filaments the characteristic mass of the GSMF is lower. Finally, our global GSMF is well described by a double Schechter function with the following parameters: $\log[M^\star/(M_\odot\, h_{70}^{-2})] = 10.76 \pm 0.01$, $\Phi_1^\star = (3.75 \pm 0.09) \times 10^{-3}$ Mpc^{-3} h_{70}^3, $\alpha_1 = -0.86 \pm 0.03$, $\Phi_2^\star = (0.13 \pm 0.05) \times 10^{-3}$ Mpc^{-3} h_{70}^3 and $\alpha_2 = -1.71 \pm 0.06$. This result is consistent with previous GAMA studies in terms of $M^\star$, although we find lower values for both α_1 and α_2.

We further deconstruct the low-redshift GSMF by separating galaxies according to their star formation activity and environment, examining how it varies across different galaxy populations (star-forming vs passive galaxies, and centrals vs satellites) and as a function of halo mass. We find that: (i) The GSMFs of passive and star-forming galaxies are well described by a double and a single Schechter function, respectively, although the inclusion of a second component for the star-forming population yields a more accurate description. Furthermore, star-forming galaxies dominate the low-mass end of the total GSMF, whereas passive galaxies mainly shape the intermediate-to-high-mass regime. (ii) The GSMF of central galaxies dominates the high-mass end, whereas satellites and ungrouped galaxies shape the intermediate-to-low-mass regime. Additionally, we find a relative increase in the abundance of low-mass galaxies moving from dense group environments to isolated systems. (iii) More massive halos host more massive galaxies, have a higher fraction of passive systems, and show a steeper decline in the number of intermediate-mass galaxies. Finally, our results reveal larger differences between passive and star-forming GSMFs than predicted by the model of Peng et al. (2010), but generally confirm the environmental quenching trends for centrals and satellites reported in other works.

List of publications

This thesis is based on the following publications:

First author publications:

- **Sbaffoni, A.**, J. Liske, S. P. Driver, A. S. G. Robotham, and E. N. Taylor. *Galaxy And Mass Assembly (GAMA): Environment-dependent galaxy stellar mass functions in the low-redshift Universe*, A&A 696, A89 (2025).
  Results presented in Chapter 6 of this thesis (referred to as Project I).
- **Sbaffoni, A.**, J. Liske, A. S. G. Robotham, L. J. M. Davies, S. P. Driver, and E. N. Taylor. *Galaxy And Mass Assembly (GAMA): deconstructing the galaxy stellar mass function by star formation and environment*, submitted to A&A.
  Results presented in Chapter 7 of this thesis (referred to as Project II).

Contents

1 Introduction

According to the Λ Cold Dark Matter (ΛCDM) cosmological paradigm, structures in the present Universe arise from hierarchical clustering, whereby smaller dark matter halos (DMHs) form first through gravitational instability and progressively merge into larger ones (Press & Schechter 1974; Blumenthal et al. 1984; Davis et al. 1985; Mo & White 1996). Baryons gather in the centres of these haloes, a small fraction of which cools and subsequently condenses into stars to form galaxies (White & Rees 1978; White & Frenk 1991; Navarro et al. 1997).

The rate at which new stars form in galaxies is a crucial aspect of understanding the initial formation and subsequent evolution of galaxies. Galaxies grow primarily through two mechanisms, namely star formation (SF; Kennicutt 1998a) and hierarchical merging (Baugh 2006), which are not independent. The first process is closely related to a galaxy's internal properties, such as its atomic and molecular gas content (Kennicutt 1998a; Kereš et al. 2005), stellar (Brinchmann et al. 2004; Daddi et al. 2007a; Elbaz et al. 2007; Noeske et al. 2007) and dust mass (da Cunha et al. 2010), morphology (Kauffmann et al. 2003; Guglielmo et al. 2015), activity of active galactic nuclei (AGN; Netzer 2009; Thacker et al. 2014) and metallicity (Ellison et al. 2008; Mannucci et al. 2010; Lara-López et al. 2013). In contrast, galaxy mergers are driven by external factors, particularly the local environment in 6D phase space, which determines how galaxies interact in pairs, groups, or clusters (McIntosh et al. 2008; Ellison et al. 2010; de Ravel et al. 2011). In addition, galaxy mergers and other close interactions with nearby galaxies can enhance or inhibit SF (Davies et al. 2015). Measuring the star formation rate (SFR) across different galaxy types and environments is therefore essential to understanding how galaxies accumulate mass through SF and how their surroundings shape this process.

However, DMHs – and hence the galaxies residing within them – are not isolated systems; rather, they are embedded within the large-scale structure (LSS; Kaiser 1984; Efstathiou et al. 1988), a vast and complex network also known as the *cosmic web* (Jõeveer et al. 1978; Bond et al. 1996). Under the effect of gravity across cosmic time, the cosmic web emerges from the anisotropic collapse of the initial fluctuations of the matter density field (Zel'dovich 1970). This web consists of voids, sheet-like walls, filaments, and dense clusters or knots, where filaments intersect, representing the maxima of the universal density field and the culmination of the hierarchical formation model. On large scales, matter flows out of underdense voids toward surrounding sheets, then streams along filaments and eventually accumulates in dense knots. On smaller, nonlinear scales, virialised DMHs populate the cosmic web, and galaxies form and evolve within their gravitational potential wells (e.g. Mo et al. 2010). While voids dominate the volume of the Universe, filaments and knots host the majority of the mass, haloes, and galaxies (Pimbblet et al. 2004; Aragón-Calvo et al. 2010).

Galaxies tend to group within this web, forming structures ranging from small groups to massive superclusters, all interconnected by long, linear filaments that can span up to 60-100

h^{-1} Mpc or beyond (Bharadwaj et al. 2004; Colberg et al. 2005; Novikov et al. 2006; Gott et al. 2005). Although filaments occupy only ~ 6% of the cosmic volume, they contain nearly half of the total dark matter content of the Universe (Bond & Myers 1996; Pogosyan et al. 1996; Cautun et al. 2014), highlighting their critical role in shaping the cosmic web. In contrast, voids are vast underdense regions, typically spanning 20–50 h^{-1} Mpc, populated by only a sparse population of galaxies and exhibiting densities roughly 10% below the cosmic mean (Pan et al. 2012).

Consequently, galaxies can be broadly classified by the large-scale environments they inhabit into clusters, filaments, and voids, each of them offering distinct physical conditions that may influence their formation and evolution. Whereas galaxies within clusters experience frequent interactions and strong environmental effects, those in voids evolve in relative isolation, making them ideal laboratories for studying galaxy evolution in the absence of processes associated with dense environments. The very few galaxies populating voids are subject to dynamics that are unique to those underdense regions (Blumenthal et al. 1992; Sheth & van de Weygaert 2004), and as such, voids serve as powerful tools for constraining cosmological parameters and testing cosmological simulations (Dekel & Rees 1994; Lavaux & Wandelt 2010; Park et al. 2012).

Within this large-scale cosmic framework, the formation and evolution of DMHs occur through two well-established mechanisms: the accretion of diffuse material from the surrounding medium, and the incorporation of matter during halo mergers. Galaxies evolve within these haloes, where a range of physical processes — such as gas cooling, SF, and feedback — regulate their growth and shape their observable properties. Since haloes and galaxies evolve simultaneously, the assembly history of a halo plays a key role in setting the evolutionary path of its galaxy. For instance, when a halo is accreted by a more massive one, its associated galaxy may be subjected to environmental processes such as the stripping of its diffuse hot gas reservoir, thereby suppressing future SF (e.g. Larson et al. 1980; Weinmann et al. 2006; van den Bosch et al. 2008). Naturally, this framework implies that galaxy properties are intimately linked to the evolution of their host haloes (Somerville & Davé 2015).

Understanding which DMH properties primarily govern galaxy formation remains a key challenge in astrophysics. The simplest assumption made by many models is that a single property (e.g. halo virial mass $M_{\rm vir}$) fully determines the statistical properties of the galaxies they host. This assumption is supported by early studies showing that halo properties correlate strongly with the large-scale environment, primarily through changes in halo mass (e.g. Lemson & Kauffmann 1999). However, it is now well established that halo properties are influenced by more than just mass, a phenomenon known as *halo assembly bias* (Gao et al. 2005; Gao & White 2007; Li et al. 2008; Faltenbacher & White 2010; Lacerna & Padilla 2011). In particular, Wechsler et al. (2006) showed that for haloes with $M_{\rm vir} \lesssim 10^{13} M_{\odot}$, early-forming haloes are more clustered than their late-forming counterparts, whereas the trend reverses for more massive haloes. Despite such environmental dependencies, it remains possible that certain galaxy properties can still be reliably predicted from halo mass alone. This assumption supports empirical models such as the *halo occupation distribution*, which assumes that galaxy distributions depend solely on halo mass (e.g. Mo et al. 2004; Abbas & Sheth 2006; van den Bosch et al. 2007), and have successfully reproduced galaxy clustering not only as a function of mass or luminosity, but also as a function of colour and other properties (e.g. Berlind & Weinberg 2002; Zheng et al. 2005; Tinker et al. 2013; Rodríguez-Puebla et al. 2015).

Recent studies have shown that the cosmic web itself plays a role in modulating the halo assembly bias, highlighting the non-trivial connection between halo evolution and the large-scale environment (e.g. Borzyszkowski et al. 2017; Tojeiro et al. 2017; Yang et al. 2017; Musso et al. 2018; Ramakrishnan et al. 2019). In this context, it is useful to distinguish between internal and environmental halo properties. The link between galaxy properties and internal halo characteristics, such as concentration or formation time, is known as *galaxy assembly bias* (e.g. Croton et al. 2007). This phenomenon impacts galaxy clustering, and has been confirmed in observations (e.g. Cooper et al. 2010; Wang et al. 2013; Zentner et al. 2019). On the other hand, environmental halo properties, such as the matter density on intermediate scales, are naturally associated with halo clustering. Any dependence of galaxy properties on these environmental factors will be reflected in galaxy clustering as well (e.g. Artale et al. 2018; Zehavi et al. 2018; Xu et al. 2021). Since internal and environmental halo properties are typically correlated, their respective impacts on galaxy properties are also mutually dependent.

Our understanding of the cosmic web has significantly advanced thanks to the advent of wide-field spectroscopic surveys such as the Two-degree Field Galaxy Redshift Survey (2dFGRS; Colless et al. 2001), the Millennium Galaxy Catalogue (MGC; Liske et al. 2003), the Sloan Digital Sky Survey (SDSS; Abazajian et al. 2009), the Six-degree Field Galaxy Survey (6dFGS; Jones et al. 2009), and the Galaxy And Mass Assembly (GAMA; Driver et al. 2011; Liske et al. 2015). Together with sophisticated structure-finding algorithms (e.g. Doroshkevich et al. 2004; Pimbblet 2005; Eardley et al. 2015), these surveys have enabled the identification and characterization of clusters, filaments, and voids.

N-body simulations reveal a dynamic flow of matter within the cosmic web, progressing from voids to sheets, then to filaments, and eventually into clusters (Aragón-Calvo et al. 2010; Cautun et al. 2014; Ramachandra & Shandarin 2015; Wang et al. 2024). Hydrodynamical simulations indicate that over 40% to 50% of baryonic matter resides within filaments as the warm-hot intergalactic medium (WHIM) (Tuominen et al. 2021; Galárraga-Espinosa et al. 2021). The WHIM acts as a gas reservoir that can eventually accrete onto galaxies, influencing their growth and SFRs. Depending on their location within the cosmic web, galaxies experience different levels of gas accretion. For example, those near the centers of filaments and sheets receive a steady inflow of cold gas, which fuels SF and increases their mass (Chen et al. 2017; Singh et al. 2020; Pandey & Sarkar 2020; Das et al. 2023; Hoosain et al. 2024). Clusters typically form at the intersections of filaments and are characterized by frequent interactions with neighboring galaxies and extreme environmental conditions, leading to relatively rapid transformations of cluster galaxies (Gunn & Gott 1972; Roediger & Brüggen 2007; Ruggiero & Lima Neto 2017). In contrast, galaxies in lower-density regions such as sheets and voids tend to follow more gradual evolutionary paths with suppressed SF (Einasto et al. 2022; Rodríguez-Medrano et al. 2024). Thus, the different environments within the cosmic web are thought to play a crucial role in shaping the diverse evolutionary trajectories of galaxies across the universe. In this context, Aragon Calvo et al. (2019) introduced the so-called *cosmic web detachment*, whereby galaxies disconnect from the cold gas-supplying filaments of the primordial web, thus halting their gas inflow. Other works suggest that galaxies located near the centers of filaments may experience suppressed gas inflows due to reduced angular momentum supply, preventing the transport of cold gas from the outer parts of halos to galactic centers (Song et al. 2021). Pasha et al. (2023) showed that cosmological

accretion shocks at $z \sim 2$–5 can generate a hot ($T > 10^6$ K) intergalactic medium (IGM) at the edges of sheets, which can quench low-mass central galaxies at these epochs, analogous to the effect of shocks around filaments, groups, and clusters observed at lower redshifts (Birnboim et al. 2016; Zinger et al. 2018; Li et al. 2023).

Filaments, in particular, have been extensively studied as key structures of the cosmic web. Tempel & Libeskind (2013) applied a marked point process to model filaments in SDSS data as sequences of narrow connected cylinders, finding typical lengths of 60 h^{-1} Mpc and showing that galaxies in filaments account for 35-40% of the total luminosity function. Alpaslan et al. (2014) further expanded this structural framework by introducing *tendrils*, i.e. narrow coherent structures spanning up to 10 h^{-1} Mpc and often bridging between filaments or connecting to voids. Employing filament detection methods, numerous studies have explored cosmic filaments to understand their influence on galaxy formation and evolution (e.g. Darvish et al. 2014; Vulcani et al. 2019; Sarron et al. 2019; Parente et al. 2024). A key focus has been on how galaxy properties vary with respect to their distance from filament axes. Many investigations suggest that galaxies tend to increase in stellar mass as they approach filaments, based on both simulations (e.g. Bulichi et al. 2024) and observational data (e.g. Chen et al. 2017; Malavasi et al. 2017; Hoosain et al. 2024). However, some studies have found contrasting results; for example, Kuutma et al. (2017) reported no significant increase in stellar mass near filaments. Galaxy sizes represent another crucial observational aspect relevant for advancing theories of galaxy evolution. Using data from two cosmological hydrodynamical simulations, Jiang et al. (2019) showed that galaxy size does not depend on halo spin but inversely correlates with halo concentration. Considering the substantial influence of cosmic filaments on galaxy and halo spin orientations, statistical alignments between galaxy orientation and the cosmic web have been detected (e.g. Zhang et al. 2009, 2013, 2015), while correlations between galaxy spins and the surrounding structure, largely driven by tidal torques, have been confirmed in both simulations and observations (e.g. Navarro et al. 2004; Paz et al. 2008; Tempel & Libeskind 2013). These findings emphasize the dynamic interplay between galaxies and their environment, further supporting the idea that the cosmic web shapes not only galaxy properties such as mass and size, but also their angular momentum and orientation.

However, the exact role of the cosmic web in regulating SF remains uncertain. While several observational studies have found that quenched galaxies tend to reside near nodes and filaments (Kuutma et al. 2017; Kraljic et al. 2018; Laigle et al. 2018; Winkel et al. 2021), others report enhanced SF in similar environments (Darvish et al. 2014; Vulcani et al. 2019). Therefore, consensus is yet to be reached on the impact of cosmic web environment on galaxy quenching, and how this varies with stellar mass and redshift.

Consequently, the exact role of the LSS in shaping galaxy properties remains an open question. To what extent does the large-scale environment ($\gtrsim 1$ h^{-1} Mpc) influence the formation, evolution, and observable properties of galaxies? In other words, is a galaxy embedded in a filament systematically different from a similar-mass galaxy in a void? A growing number of observational and theoretical works suggest that the answer is yes: galaxy properties such as SFR, colour, morphology, and stellar mass all show significant and non-trivial dependence on the type and density of the surrounding environment (e.g. Dressler 1980; Kodama et al. 2001; Blanton et al. 2005; González & Padilla 2009; Sobral et al. 2011; Eardley et al. 2015; Kraljic et al. 2018; Alam et al. 2019; Aragon Calvo et al. 2019). Understanding these dependencies is essential for bridging

the gap between simulations and observations, refining empirical models of galaxy formation, and constraining the physical processes governing the cosmic web's influence on galaxies.

The Galaxy Stellar Mass Function (GSMF; Bell et al. 2003; Baldry et al. 2008, 2012; Wright et al. 2017; Driver et al. 2022), which quantifies the number density of galaxies as a function of stellar mass, is one of the most fundamental measurements in extragalactic astronomy. In addition to constraining the baryonic content of galaxies, the GSMF is the result of the hierarchical mass assembly of DMHs, gas accretion, SF, feedback, and environmental effects over cosmic time (Brinchmann & Ellis 2000). As such, the GSMF provides a powerful diagnostic to test galaxy formation models and to compare galaxy populations across different redshifts and environments.

Initial measurements of the GSMF were conducted in the optical, and subsequently extended to the near-infrared (NIR), where the light more accurately traces the older, low-mass stellar populations that dominate the stellar mass reservoir (Bell et al. 2003). In fact, the stellar masses of galaxies may be estimated either from optical and/or NIR photometry (Larson & Tinsley 1978; Jablonka & Arimoto 1992; Bell & de Jong 2001) where, generally speaking, a broader wavelength coverage will result in a higher precision, or derived through spectral energy distribution (SED) fitting or spectroscopy (Kauffmann et al. 2003; Panter et al. 2004; Gallazzi et al. 2005). Multi-wavelength photometric and spectroscopic surveys such as SDSS and GAMA are thus able to estimate stellar masses with a typical uncertainty of ∼0.2 dex (Taylor et al. 2011), and the most significant measurements of the GSMF obtained from SDSS (Bell et al. 2003; Baldry et al. 2008) and GAMA (Baldry et al. 2012; Wright et al. 2017), in which the GSMF was probed to a stellar mass limit of 10^8 $M_\odot$, are in reasonable agreement. These efforts have led to a general consensus on the shape of the local GSMF and its variation with galaxy properties such as colour, morphology, and SF activity (Baldry et al. 2012; Kelvin et al. 2014; Moffett et al. 2016a,c).

Beyond the local Universe, the GSMF has become a key tracer of stellar mass growth over cosmic time. Numerous studies have extended its measurement out to redshifts of $z \sim 1$–2 (e.g. Fontana et al. 2004; Conselice et al. 2005; Borch et al. 2006; Bundy et al. 2006; Pannella et al. 2006), and even to $z \sim 4$–5 and beyond (e.g. Drory et al. 2005; Fontana et al. 2006; Pérez-González et al. 2008; Caputi et al. 2011; González et al. 2011; Lee et al. 2012; Duncan et al. 2014). These works have revealed a steepening of the low-mass slope at higher redshifts, indicating a large population of low-mass galaxies at early epochs (e.g. Marchesini et al. 2009a; Kajisawa et al. 2009; Mortlock et al. 2011; Santini et al. 2012; Tomczak et al. 2014). At the same time, wide-area surveys have provided robust constraints on the high-mass end of the GSMF, whose turnover appears to evolve only mildly with redshift (e.g. Ilbert et al. 2010, 2013; Pozzetti et al. 2010; Davidzon et al. 2013; Moustakas et al. 2013; Muzzin et al. 2013). Moreover, it is now established that roughly half of the present-day stellar mass density was already in place by $z \sim 1$ (e.g., Rudnick et al. 2003; Bundy et al. 2005; Borch et al. 2006; Fontana et al. 2006; Pozzetti et al. 2007; Pérez-González et al. 2008; Marchesini et al. 2009b; Ilbert et al. 2010), with both the high- and low-mass ends of the GSMF evolving mostly in normalization rather than shape. This gradual evolution supports a scenario in which massive galaxies experience rapid early growth followed by efficient quenching, likely due to AGN feedback (Bower et al. 2006; Croton et al. 2006).

From a theoretical perspective, reproducing the observed GSMF and its redshift evolution remains a critical test for galaxy formation models. These models connect the hierarchical growth of DMHs predicted by the ΛCDM cosmological framework with the observable properties of

galaxies via simplified, physically motivated prescriptions for the formation of baryonic systems. Within this context, galaxies are expected to assemble in a bottom-up fashion, reflecting the merging history of their host halos. However, observations indicate that the most massive galaxies assembled their stellar mass early and rapidly, suggesting a top-down trend in stellar mass buildup often referred to as *downsizing*. This apparent discrepancy is partly resolved by the prediction that massive galaxies form most of their stellar mass through dry mergers (i.e., gas-poor and thus SF-inefficient events) at $z < 1$ (De Lucia et al. 2006), which are challenging to detect observationally (e.g., Hopkins et al. 2008). In this context, semi-analytic models (SAMs) and hydrodynamical simulations (e.g., Bower et al. 2006; Kitzbichler & White 2007; Fontanot et al. 2009) have made substantial progress in reproducing the GSMF across redshifts, thereby reconciling the bottom-up assembly of DM structures with the early formation of stellar mass in massive galaxies (Cimatti et al. 2006).

While the integral of the GSMF defines the density of baryonic mass currently bound in stars, and thus the global SF efficiency, its shape, characterized by a power-law with an exponential cut-off at high masses, is related to the evolutionary processes governing SF. In particular, it reflects the combined effects of SF, feedback, and merging across a wide range of halo masses. Consequently, the GSMF has been widely used to constrain galaxy formation models, from empirical approaches to numerical simulations (Peng et al. 2010; Behroozi et al. 2013; Henriques et al. 2015; Pillepich et al. 2018; Schaye et al. 2015; Davé et al. 2019; Schaye et al. 2023). A widely used model to describe the shape of the GSMF is the Schechter function (Schechter 1976), which captures its characteristic truncated power-law behaviour:

$$\phi(M)dM = e^{-\frac{M}{M^\star}}\phi^\star\left(\frac{M}{M^\star}\right)^\alpha \frac{dM}{M^\star}, \tag{1.1}$$

where $\phi^\star$ is the normalisation factor, $M^\star$ the mass at the normalisation point, i.e. near the exponential break, and α the faint-end slope parameter. However, the shape of the GSMF is not always well represented by a single Schechter function, due to an often observed steepening below $10^{10}\ M_\odot$, giving rise to a double Schechter function (Baldry et al. 2008):

$$\phi(M)dM = e^{-\frac{M}{M^\star}}\left(\phi_1^\star\left(\frac{M}{M^\star}\right)^{\alpha_1} + \phi_2^\star\left(\frac{M}{M^\star}\right)^{\alpha_2}\right)\frac{dM}{M^\star}, \tag{1.2}$$

where $\phi_1^\star$, $\phi_2^\star$ and α_1, α_2 describe the normalization and slope parameters, respectively, for the two components. Without loss of generality, we can always choose $\alpha_1 > \alpha_2$ such that the second term in Equation 5.2 dominates at lower masses (Baldry et al. 2012).

Explaining the shape of the GSMF, especially in comparison to that of the robustly predicted halo mass function (HMF), is one of the major challenges in galaxy formation theory. Unlike the HMF, which exhibits a simple power-law form with a break only at the very high-mass end, the GSMF is significantly shallower at low masses and shows an exponential turnover at lower masses. This discrepancy highlights the necessity of baryonic feedback processes that regulate or suppress SF with different efficiencies at different mass scales. The shape of the GSMF is generally interpreted as the result of two primary feedback mechanisms that suppress SF. At low halo masses, supernova feedback creating galactic winds plays a crucial role in regulating SF

(Larson 1974; Dekel & Silk 1986; Pillepich et al. 2018; Scharré et al. 2024), while Oppenheimer et al. (2010) claimed that the re-accretion of these winds is essential in shaping the GSMF. At higher masses, initially infalling gas is heated by a virial shock (Dekel & Birnboim 2006) and subsequently prevented from cooling by feedback from AGN, thereby suppressing SF (Kereš et al. 2005; Croton et al. 2006; Pillepich et al. 2018; Scharré et al. 2024). Both of these feedback processes have a mass dependence, i.e. the efficiency with which they suppress SF depends on halo mass. Additionally, galaxy mergers also contribute to shaping the GSMF by shifting galaxies to higher stellar masses, potentially becoming the dominant mechanism at masses greater than $10^{10.8}$ $M_{\odot}$ (Robotham et al. 2014). Thus, the GSMF encodes both the cumulative effects of in-situ SF and the ex-situ assembly history of galaxies through mergers. Since all of these processes depend on halo mass and are expected to vary with environment, the shape of the GSMF is likewise expected to exhibit environmental dependence.

In galaxy evolution theory, it is often assumed that galaxy properties (including their stellar mass) are determined solely by the mass of the DMH in which they reside, and not by any other environmental properties (Moster et al. 2010, and references therein). In this context, Moster et al. (2010) found a tight correlation between the stellar mass of central galaxies and the mass of their host DMHs, using N-body simulations to show that galaxy clustering is largely driven by the clustering of the underlying halos and subhaloes. Their model also provides a means to predict galaxy clustering as a function of stellar mass at any redshift. These findings suggest that the total stellar mass function could depend on environment, given that halo clustering and assembly histories vary within the LSS. However, a direct investigation of the relation between the total GSMF and the mass of the parent halo remains largely unexplored. Understanding whether simulations predict a segregation of stellar mass with environment, as a function of both initial and evolved halo mass, would offer critical insight into the role of halo mass in shaping the GSMF across cosmic time.

Characterizing the role of environment in galaxy evolution theory is complicated by the variety of definitions adopted in the literature. One approach relies on geometry, according to which galaxies are classified into categories such as voids (i.e. 3-dimensional structures), sheets (2-dimensional), filaments (1-dimensional) and clusters, groups or knots (0-dimensional). A second approach considers the distinction between grouped and ungrouped galaxies, where the latter are often referred to as field galaxies. A third approach classifies galaxies based on halo mass. A fourth approach describes the environment through measurements of the local density (averaged over some scale), which can be parametrized in several ways and following different techniques, e.g. by counting the number of neighbours of a galaxy within a specific aperture or measuring the distance to the n^{th} nearest neighbour. Although these definitions of environment are often correlated, they cannot be considered equivalent, and different choices may lead to different conclusions.

In contrast to theoretical expectations, several recent studies have not confirmed a dependence of the GSMF on halo mass. For example, Calvi et al. (2013) and Vulcani et al. (2013) both found that the GSMFs of the general field and of clusters are essentially indistinguishable, at low and intermediate redshifts respectively, suggesting that halo mass may not significantly influence the shape of the mass function. Similarly, Guglielmo et al. (2018) failed to find a difference between the field and cluster GSMFs, or a dependence of the cluster GSMF on X-ray luminosity,

which serves as a proxy for halo mass. Another line of investigation has focused on the relation between the GSMF and local density. For example, Vulcani et al. (2012), using both 5th and 10th nearest neighbour approaches, found that lower-density environments host proportionally more low-mass galaxies compared to denser regions. Furthermore, the most massive galaxies are preferentially found in the highest-density environments and are nearly absent in low-density regions. More recently, O'Kane et al. (2024), using a 3rd nearest neighbour estimator, showed that, when controlling for both stellar mass and local density, the apparent variations in the GSMF across different large-scale environments vanish. This result suggests that local density, rather than halo mass or cosmic web position, is the main driver of environmental effects on the GSMF.

In summary, our current understanding of galaxy formation and evolution suggests that the influence of environment on the GSMF strongly depends on how *environment* is defined. The apparently contradictory results reported in the literature largely arise from the variety of definitions and observational tracers employed, as well as the underlying complexity of the physical processes driving galaxy growth. Consequently, a consensus on the environmental dependence of the GSMF has not yet been reached, even at low redshift. The first primary goal of this doctoral thesis, extensively discussed in Chapter 6, is thus to help clarify this issue by providing a meticulous characterization of the GSMF as a function of different environmental measures using GAMA which, arguably, is the survey that offers the most comprehensive coverage of galaxy environments across a wide range of scales at low redshift.

Certain galactic properties, such as morphology or radial profiles, integrated or central colours, and total luminosity or stellar mass, exhibit well-defined correlations. Examples include colour–morphology (Roberts & Haynes 1994) and colour–magnitude relations separately for early-type (Faber 1973) and late-type galaxies (Chester & Roberts 1964). As a result, the traditional classification of galaxies has distinguished spirals from ellipticals and lenticulars (Tully et al. 1982). However, the advent of large-scale galaxy surveys, such as 2dFGRS and SDSS, has revealed additional features in galaxy properties, most notably the bimodal distribution in galaxy colour (Strateva et al. 2001; Baldry et al. 2004). This dichotomy reflects two major evolutionary stages, each characterized by distinct morphologies, SFRs, and environments. Galaxies in the local Universe can be broadly classified into two populations: at fixed stellar mass, the early-type elliptical galaxies can be interpreted as old, red, quiescent (or passive) systems, which have more spheroidal morphologies and little or no active SF, whereas the late-type spiral galaxies as blue star-forming systems, which have typically disk-like morphologies and are actively converting gas into new stars (i.e. high SFR; Shen et al. 2003; Blanton et al. 2003; Baldry et al. 2004; Balogh et al. 2004a; Bell et al. 2004a; Brinchmann et al. 2004; Ellis et al. 2005; Driver et al. 2006; Papovich et al. 2012; Taylor et al. 2015). Observations show that galaxy SF activity peaked around redshift $z \sim 2$–3 (Tran et al. 2010; Gupta et al. 2020), a period commonly referred to as *cosmic noon*. Since then, the cosmic SFR has declined sharply from $z = 1$ to the present day (Madau et al. 1996). Meanwhile, the number of massive red galaxies with fixed stellar masses has steadily increased since $z \sim 1$ (Bell et al. 2004b; Faber et al. 2007). These trends suggest significant changes in galaxy properties in recent times, which could be crucial in explaining the observed bimodality in galaxy distributions.

Since colour is more easily measured than morphology in large imaging surveys, it is now preferable to classify galaxies as belonging to the red or blue sequence rather than as early- or late-

type systems. In this context, the colour-magnitude diagram (CMD) is a fundamental diagnostic tool. On the one hand, the colour provides key insights into galaxies' stellar populations, acting as a proxy for the dust-corrected, luminosity-weighted mean stellar age. This, in turn, reflects the average specific SFR (sSFR) over long ($\sim$ Gyr) timescales. In other words, a galaxy's colour is directly tied to its SF activity, dust content, and chemical enrichment history, making it easier to interpret within theoretical models. On the other hand, a galaxy's absolute magnitude represents its total integrated starlight and often serves as a proxy for its stellar mass. As a result, the CMD effectively traces the evolution of SF as a function of stellar mass. However, a key challenge arises from the significant overlap in the (optical) colour distributions of the red and blue populations (Baldry et al. 2004; Taylor et al. 2015). This introduces both a practical issue in separating the two populations and a deeper conceptual ambiguity in defining red and blue galaxies. Nevertheless, this overlap is often statistically modelled as the sum of two Gaussian components, corresponding to the red and blue sequences, respectively (e.g. Strateva et al. 2001; Taylor et al. 2015). This statistical bimodality is found to persist across different environments, with increasing density primarily affecting the relative fractions of red and blue galaxies, but not significantly altering the intrinsic properties of each sequence (Baldry et al. 2006).

A clearer bimodality emerges when considering the SFR or sSFR versus stellar mass (Balogh et al. 2004a; Moustakas et al. 2013; Davies et al. 2016, 2019a), separating galaxies into passive and star-forming ones, and suggesting that these populations may represent distinct and possibly sequential evolutionary stages. In particular, investigations of this bimodality across different redshifts show that the passive population has nearly doubled in terms of stellar mass, stellar mass density, and number density over the past $\sim$ 7 Gyr, although the two populations seem to be roughly equivalent in terms of total stellar mass at z $\sim$ 1 (Bell et al. 2004a; Arnouts et al. 2007; Foltz et al. 2018). At earlier cosmic times, blue galaxies are more prevalent due to the rising gas fractions at higher redshifts. Their SF is fueled by these abundant gas reservoirs, which are gradually depleted through sustained SF activity. As the gas is exhausted, and the SFR gradually ceases with natural aging, the galaxy eventually becomes a red, quiescent system dominated by older and cooler stellar populations. However, the existence of two distinct colour distributions, with relatively few galaxies occupying the so-called *green valley*, implies that the transition from blue to red must occur across a broad range of stellar masses and on relatively short timescales ($\sim$ 1 Gyr or less; Balogh et al. 2004b). This colour bimodality has been confirmed up to at least $z \sim 2$ by several studies (e.g. Balogh et al. 2004b; Bell et al. 2004a; Williams et al. 2009; Taylor et al. 2015; Foltz et al. 2018), supporting its fundamental role in galaxy evolution. Besides stellar mass, environmental factors play a crucial role in shaping the transition from actively star-forming to passive quiescent systems. Late-type galaxies are more abundant at low stellar masses and at earlier cosmic times (Kauffmann et al. 2004; Baldry et al. 2006; Peng et al. 2010; Muzzin et al. 2013), whereas early-type galaxies tend to be more massive and are preferentially found in dense environments such as groups or clusters (Dressler 1980; Kauffmann et al. 2003; Blanton et al. 2005; van der Wel 2008; Woo et al. 2013). At fixed stellar mass, galaxies in denser environments are more likely to be red (Kauffmann et al. 2004; Baldry et al. 2006; van der Burg et al. 2018; Reeves et al. 2021) and quiescent (Dressler 1980; Blanton et al. 2005; Woo et al. 2013) than their field counterparts. Additionally, increased local environmental density is often correlated with lower SFR (Schaefer et al. 2017, 2019), a lower fraction of star-forming galaxies (Barsanti et al.

2018), and changes in their stellar kinematics (van de Sande et al. 2021).

To reproduce the observed bimodal colour distribution and its evolution with redshift, cosmological models incorporate mechanisms that rapidly suppress or halt SF in galaxies (Bell et al. 2003; Baldry et al. 2004; Balogh et al. 2004b; Taylor et al. 2015). This suppression, commonly referred to as *quenching* (e.g. Peng et al. 2010), is thought to transform star-forming galaxies into passive systems with very low or negligible SF. Quenching is distinct from the gradual decline in the sSFR of star-forming galaxies observed since $z \sim 2$, which may reflect a slowly decreasing gas supply. Instead, it represents a more abrupt transition, associated with the emergence of the red sequence and the bimodal nature of the galaxy population (Bell et al. 2004b; Arnouts et al. 2007; Drory et al. 2009; Peng et al. 2010; Ilbert et al. 2010; Brammer et al. 2011). In these models, quenching primarily affects more massive galaxies and/or galaxies in groups or clusters, by either depleting their existing gas reservoirs or preventing the inflow of new material.

Observationally, the star-forming GSMF shows constant values for both the characteristic stellar mass $M^\star$ and the low-mass slope α out to redshifts of at least $z \sim 2$ (Bell et al. 2003; Peng et al. 2010; Pozzetti et al. 2010; Ilbert et al. 2013). This implies that, despite substantial stellar mass growth in individual galaxies across this redshift range, its overall shape remains unchanged. The only parameter that evolves significantly with redshift is the normalization, $\phi^\star$. Star-forming galaxies are generally well described by a single Schechter function, whereas quiescent galaxies often follow a double Schechter form, highlighting the impact of quenching processes on the build-up of the passive population (e.g., Li & White 2009; Peng et al. 2010, 2012; Pozzetti et al. 2010; Baldry et al. 2012; Ilbert et al. 2013; Muzzin et al. 2013). In addition, the sSFR of star-forming galaxies shows only a weak dependence on stellar mass, but exhibits a strong decline from $z \sim 2$ to the present day (Daddi et al. 2007b; Elbaz et al. 2007; Noeske et al. 2007); this decline appears to be largely independent of environment up to at least $z \sim 1$ (Peng et al. 2010).

In the local Universe, environmental effects and internal quenching mechanisms have been argued to act independently of each other, at least out to z$\sim$ 1 (Baldry et al. 2006; Peng et al. 2010; Kovač et al. 2014). Specifically, Peng et al. (2010) distinguished between mass quenching, which depends on SFR and predominantly affects massive galaxies regardless of their environment, and environmental quenching, which acts independently of stellar mass and preferentially affects galaxies in dense environments such as groups or clusters (Davies et al. 2016; Kawinwanichakij et al. 2017). Mass quenching is found to dominate at high stellar masses ($\log_{10}(M_\star/M_\odot) \gtrsim 10$), and correlates with internal properties such as bulge prominence (Fang et al. 2013; Bluck et al. 2016; Bremer et al. 2018), central velocity dispersion (Wake et al. 2012; Teimoorinia et al. 2016), or AGN activity (e.g. Nandra et al. 2007). In contrast, environmental quenching is more effective in low- to intermediate-mass galaxies ($\log_{10}(M_\star/M_\odot) \lesssim 10$), and is linked to local density (Peng et al. 2012; Treyer et al. 2018) and position (Wolf et al. 2009; Wetzel et al. 2012; Woo et al. 2015; Barsanti et al. 2018) within group or cluster environments.

The exact mechanisms responsible for quenching are still under debate. Mass quenching is commonly attributed to feedback mechanisms, including supernovae and galactic winds (Oppenheimer et al. 2010), differences between hot and cold accretion modes due to the presence or absence of persistent shocks in infalling gas (Kereš et al. 2005; Dekel & Birnboim 2006; Cattaneo et al. 2008; van den Bosch et al. 2008), and AGN activity, especially in high-mass systems (Benson

et al. 2003; Croton et al. 2006; Menci et al. 2006; Bower et al. 2006, 2008; Tremonti et al. 2007; Somerville et al. 2008; Davies et al. 2025b). In fact, AGN feedback was originally introduced in SAMs to better reproduce both the GSMF and the observed colour bimodality, by suppressing the overproduction of massive, star-forming central galaxies (e.g. Bower et al. 2006; Croton et al. 2006). Although different cosmological models implement these mechanisms in various ways, they generally agree that mass quenching correlates strongly with halo mass, primarily through the suppression of gas cooling in massive haloes. In particular, theoretical models suggest that haloes with masses $\log(M_{\rm vir}/M_{\odot}) \gtrsim 11.5$–$12$ can support stable virial shocks that heat the infalling gas, leading to the formation of a hot, hydrostatically stable circumgalactic medium (CGM). This hot CGM prevents the accretion of cold gas onto the interstellar medium (ISM), thereby halting the supply of fuel needed for SF (Birnboim & Dekel 2003; Dekel & Birnboim 2006; Kereš et al. 2005, 2009; Dekel et al. 2009).

At the same time, other processes have been proposed as drivers of environmental quenching. These include the removal of cold gas through ram pressure stripping and tidal interactions (Gunn & Gott 1972; Moore et al. 1999; Brough et al. 2013; Brown et al. 2017; Poggianti et al. 2017; Barsanti et al. 2018), as well as galaxy harassment and mergers (Moore et al. 1996; Bialas et al. 2015). In the hot, dense haloes of galaxy groups and clusters, hydrodynamical interactions between the halo medium and satellite galaxies (Bahé & McCarthy 2015; Boselli et al. 2022), along with tidal forces between galaxies or with the halo potential (Boselli & Gavazzi 2006; Marasco et al. 2016), can effectively remove the star-forming ISM. On longer timescales, SF can be suppressed via strangulation or starvation, where gas accretion is halted either from the IGM to the CGM, or from the CGM to the ISM (Larson et al. 1980; Balogh & Morris 2000; Peng et al. 2015). These mechanisms gradually deplete the cold gas reservoir, particularly in dense environments (Barsanti et al. 2018; Trussler et al. 2020; Sotillo-Ramos et al. 2021). In the most extreme environments, such as massive clusters, quenching mechanisms are expected to be more intense, resulting in significantly higher fractions of quenched galaxies compared to the field at similar redshifts (De Lucia et al. 2004; van der Burg et al. 2013; Annunziatella et al. 2014; Balogh et al. 2016; Nantais et al. 2016, 2017; Wagner et al. 2017). In these environments, dynamical interactions become increasingly relevant at later times and may act largely independently of galaxy mass. For example, ram-pressure stripping can quickly remove a galaxy's cold gas reservoir, halting SF on short timescales (Fossati et al. 2016; Bellhouse et al. 2017; Zinger et al. 2018; Jaffé et al. 2018).

An important approach to studying environmental quenching involves linking the evolutionary histories of galaxies to the environments defined by their host DMHs. Group catalogues are powerful tools in this context, as they provide a crucial bridge between astrophysical observations and DMHs predicted by the ΛCDM cosmological paradigm (Zheng et al. 2024). Since galaxy groups represent the observable counterparts of DM haloes, they provide direct insight into the physical processes shaping these structures over cosmic time. For example, these catalogues allow for the study of DM dynamics (Plionis et al. 2006; Robotham et al. 2008), and reveal how galaxies are distributed within halos (Cooray & Sheth 2002; Yang et al. 2003; Cooray 2006; Robotham et al. 2006, 2010b).

Environmental mechanisms primarily affect satellite galaxies, whereas central galaxies remain largely unaffected. A *central* galaxy is often defined as the most massive and luminous

galaxies within a DMH, regardless of its precise spatial location inside the halo. Other galaxies within the same halo are called *satellites*. Centrals are generally expected to reside near the centers of their gravitational potential wells, while satellites reside in sub-haloes that have been accreted onto larger haloes and orbit the central galaxy. As a result, centrals are less susceptible to gas stripping, harassment, and tidal effects, and are better able to retain their gas reservoirs. Consequently, centrals and satellites undergo different quenching pathways, resulting in distinct passive fractions even at fixed stellar mass (van den Bosch et al. 2008; Weinmann et al. 2009; Peng et al. 2012; Wetzel et al. 2012; Knobel et al. 2013; Robotham et al. 2014; Grootes et al. 2017; Davies et al. 2025a). In particular, van den Bosch et al. (2008) showed that satellites are systematically redder than centrals of the same stellar mass, and estimated that approximately 40% of star-forming satellites had been quenched. This framework represents the accepted model of environmental quenching, where satellite galaxies experience additional suppression of SF in groups and clusters (Wetzel et al. 2013; Treyer et al. 2018; Davies et al. 2025a), particularly when they are significantly less massive than their central galaxy. This model is both used in SAMs (e.g. Cole et al. 2000; Henriques et al. 2015; Stevens & Brown 2017; Cora et al. 2018; Lagos et al. 2018) and observed in hydrodynamic simulations (e.g. Bahé & McCarthy 2015). Empirical support comes from the study by Davies et al. (2019b), based on the GAMA galaxy group catalogue (G^3C; Robotham et al. 2011), which found that the fraction of passive galaxies increase with halo mass at fixed stellar mass, and with stellar mass at fixed halo mass, for both centrals and satellites. Importantly, satellites display significantly higher passive fractions than centrals, particularly at low stellar masses and in high-mass halos.

In contrast to this picture, several studies have suggested that central and satellite galaxies may exhibit similar passive fractions when controlled for both stellar and halo mass, implying that quenching might occur independently of a galaxy's central/satellite status (e.g. Hirschmann et al. 2014; Knobel et al. 2015). Notably, Wang et al. (2018a) analysed SDSS galaxies using the group catalogue of Yang et al. (2007), finding no significant difference in passive fraction once mass was controlled. They argued that satellite quenching may not be a dominant process in forming passive galaxies. However, they also noted that this similarity is most apparent at high stellar masses, where environmental effects are expected to be weaker, and that their results may be affected by group-finder biases. Indeed, Campbell et al. (2015) showed that some group-finders often misclassify centrals and satellites, leading to increased artificial central–satellite similarity. Wang et al. (2018b) confirmed this using simulations that intrinsically predict different passive fractions for centrals and satellites: when mock light cones were processed with the Yang et al. (2007) group-finder, these differences largely disappeared. This highlights the importance to account for uncertainties in group identification when comparing centrals and satellites.

While this framework is well established in the local Universe, it appears to break down at higher redshifts ($z \gtrsim 1$), where environmental and mass quenching are no longer fully independent (Papovich et al. 2018). In particular, a starvation or strangulation scenario, in which the supply of hot gas is halted, may become especially effective under the intense SF and outflow conditions typical of high-redshift galaxies. This so-called *overconsumption* model suggests a mass-dependent effect, as more massive galaxies deplete their gas more quickly (McGee et al. 2014). Observationally, this is supported by the fact that for low-mass galaxies ($M_\star \lesssim 10^{9.5}$ $M_\odot$), quenching timescales are comparable to gas depletion timescales (Davies et al. 2016).

These quenching processes leave distinct imprints on the GSMFs of different galaxy populations. For instance, star-forming and passive galaxies, as well as centrals and satellites, exhibit significant differences in their mass distributions. Peng et al. (2010) proposed a phenomenological model in which the combination of mass and environment quenching naturally produces a quasi-static single Schechter function for star-forming galaxies, governed entirely by the mass quenching rate, and a double Schechter function for passive galaxies, with its components corresponding to the two distinct quenching mechanisms. In a follow-up study, Peng et al. (2012) showed that environmental quenching affects only satellite galaxies, whereas central galaxies are subject to mass-driven quenching. As a result, the GSMF of passive centrals is well described by a single Schechter function, while that of passive satellites requires a double Schechter form because of the combined effects of mass and satellite quenching. In addition, halo mass is a fundamental driver of galactic properties, including their stellar mass. Vázquez-Mata et al. (2020) showed that the mass functions of centrals and satellites vary systematically with halo mass, and that the red galaxy fraction increases with halo mass, highlighting the ongoing suppression of SF in galaxy groups. The other main goal of this doctoral thesis, extensively discussed in Chapter 7, is thus to help clarify the respective contributions of mass and environmental quenching in shaping the GSMF. To this end, we present a detailed characterisation of the mass functions for star-forming and passive galaxies, centrals and satellites, and their dependence on halo mass, using GAMA, which offers robust measurements of galaxy properties and group environments at low redshift.

This thesis is organised as follows. In Chapter 2, we present an overview of the GAMA survey, including its motivations, phases, spectroscopic completeness, scientific goals, and the specific data products that have been used in this analysis. In Chapters 3 and 4, we explain in detail the complexities of our target selection and the derivation of various galaxy subsamples, respectively. In Chapter 5, we describe our precise method of deriving the GSMF. In Chapter 6, we present our environment-dependent GSMFs, analysing variations in filaments, voids, grouped and ungrouped galaxies, and dependence on group halo mass and filamentary structure (Project I). In Chapter 7, we present our GSMFs deconstruced by SF activity and environment, focusing on star-forming vs passive and central vs satellite galaxies, including their halo mass dependence (Project II). In both chapters, results are compared with previous GAMA, SDSS, and other relevant studies on environmental effects on the GSMF. Finally, in Chapter 8, we draw our conclusions. Throughout this doctoral thesis, we assume a '737' cosmology, with $(H_0, \Omega_M, \Omega_\Lambda) = (70, 0.3, 0.7)$, corresponding to the same cosmological model used in most GAMA studies on the GSMF. For all physical quantities that depend on H_0 we include this dependency using $h_{70} = H_0/(70 \text{ km s}^{-1} \text{ Mpc}^{-1})$.

2 Data

In this chapter, we describe the provenance of the data used in this doctoral thesis.

2.1 The Galaxy And Mass Assembly survey

Our data are part of both the Galaxy And Mass Assembly[1] (GAMA) II (Liske et al. 2015) and the GAMA III (Bellstedt et al. 2020a; Driver et al. 2022) surveys. GAMA is a large, low-redshift spectroscopic survey covering ~238 000 galaxies down to the extinction-corrected Petrosian magnitude limit of $r < 19.8$ mag. This limit yields an average target density of 1050 galaxies per square degree, up to an order of magnitude higher than the SDSS (90 deg^{-2}, Strauss et al. 2002) and the 2dFGRS (140 deg^{-2}). As a result, galaxies that might previously have been considered to be isolated field objects are now part of an underlying group of faint galaxies. Similarly, regions once thought to contain few galaxies now host more galaxies as well as a considerable number of structures.

GAMA spans over ~286 deg^2 of the sky, split into 3 equatorial regions measuring 12×5 deg^2 = 60 deg^2 each, out to a redshift of approximately 0.6, centred at $\alpha = 9\,h$, $\delta = 0.5$ deg (G09), $\alpha = 12\,h$, $\delta = -0.5$ deg (G12) and $\alpha = 14.5\,h$, $\delta = -0.5$ deg (G15), and 2 southern regions centred at $\alpha = 2\,h$, $\delta = -7$ deg (G02) and $\alpha = 23\,h$, $\delta = -32.5$ deg (G23). The observations were completed in 2014, using the AAOmega spectrograph (Saunders et al. 2004; Smith et al. 2004; Sharp et al. 2006) on the 3.9-m Anglo-Australian Telescope. The survey strategy and spectroscopic data reduction are described in detail in Baldry et al. (2010); Robotham et al. (2010a); Driver et al. (2009, 2011); Hopkins et al. (2013); Baldry et al. (2014); Liske et al. (2015); Baldry et al. (2018); Driver et al. (2022).

In addition, the GAMA team collected imaging data for the same survey regions from a number of independent surveys in more than 20 bands, with wavelengths between 1 nm and 1 m. Details of these imaging surveys and the photometry derived from them are given in Liske et al. (2015), Driver et al. (2016, 2022), and references therein. The combined spectroscopic and multi-wavelength photometric data at the depth, imaging resolution, area and spectroscopic completeness of GAMA provide a uniquely comprehensive survey of the low redshift galaxy population, capturing a wide range of scales relevant to galaxies.

In the rest of this chapter, we describe the motivations for choosing GAMA for the work presented in this doctoral thesis (Sect. 2.2), outline the distinctions between its three main phases (Sect. 2.3), summarise its primary scientific goals (Sect. 2.4), and describe its various data products that we use in our study (Sect. 2.5).

[1] https://www.gama-survey.org/

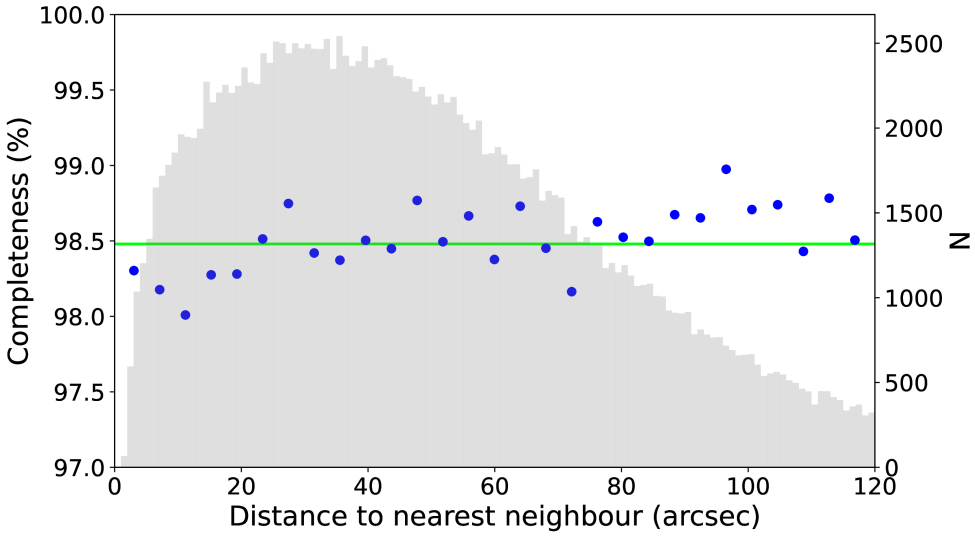

Figure 2.1: Redshift completeness of the three equatorial GAMA regions G09, G12 and G15, as a function of the distance to the nearest neighbour among main survey targets (blue dots). As in Liske et al. (2015), the horizontal green line and the grey shaded histogram show the overall average redshift completeness and the distribution of all nearest neighbour distances, respectively.

2.2 Why GAMA?

GAMA was built on the foundation of the SDSS, which provided high-quality spectroscopic data as well as five-band optical CCD imaging and photometry over ~14 000 deg^2 of the sky (York et al. 2000). The SDSS input catalogue is based on flux-limited samples, with minimal pre-selection other than the application of strict star–galaxy separation criteria (Strauss et al. 2002); the result is a complete flux-limited sample with relatively high spectroscopic completeness (> 80%).

Building upon this, GAMA introduces several key enhancements: (i) an extension of the spectroscopic survey depth by 2 magnitudes, enabling the detection of dwarf galaxies and improving the characterization of galaxy environments; (ii) significantly higher spectroscopic completeness for galaxy pairs, groups, and clusters, which is crucial for robust measurements of halo masses and merger rates; (iii) a factor of ~2 higher resolution in both optical and NIR imaging, allowing detailed analyses of internal galaxy structure; (iv) extensive multi-wavelength coverage with 21 broadband photometric filters, ranging from far-UV to far-IR (Driver et al. 2016).

In this study we only consider the three equatorial GAMA survey regions G09, G12 and G15, for which the overall redshift completeness is ~98.5% down to the magnitude limit of $r = 19.8$ mag. One of the unique features of GAMA is that this exceptionally high average redshift completeness is maintained even in the densest environments such as pairs, groups, and clusters of galaxies (Robotham et al. 2010a; Baldry et al. 2010; Liske et al. 2015). To illustrate this point, we show in Fig. 2.1 the redshift completeness of GAMA as a function of the distance to the nearest neighbour among main survey targets (see also Liske et al. 2015). Thanks to the large number of visits to each patch of sky during the spectroscopic campaign, the redshift

completeness stays roughly constant with nearest neighbour separation. The only residual effect is a tiny reduction of the completeness by ~0.5% at nearest neighbour distances of ~10 and ~70 arcsec. This is a huge advance on the capabilities of previous large spectroscopic surveys like SDSS and 2dFGRS that are almost single pass and hence suffer seriously from spectroscopic incompleteness in clustered regions.

2.3 GAMA I vs GAMA II vs GAMA III

While GAMA I refers to all data and data products collected during the first three years of survey operations (February 2008 – May 2010, see Driver et al. 2011), GAMA II refers to the entire GAMA dataset which includes both GAMA I and subsequent data. GAMA I extended over the 3 equatorial survey regions of 48 deg^2 each, down to the magnitude limits of $r < 19.4$ mag in both G09 and G15, and $r < 19.8$ mag in G12; the target selection was performed by SDSS DR6 photometry (Adelman-McCarthy et al. 2008).

GAMA II significantly extended the spectroscopic survey by: (i) expanding each GAMA I equatorial region from $\sim 12 \times 4$ to $\sim 12 \times 5$ deg^2; (ii) extending to $r < 19.8$ mag the depths of G09 and G15; (iii) updating the target selection in the equatorial regions to SDSS DR7 (Abazajian et al. 2009). Despite these changes, all objects identified as targets in GAMA I were maintained as targets in GAMA II for consistency.

In contrast to the earlier phases, GAMA III (also known as GAMA-KiDS-VIKING or GKV) did not contribute additional spectroscopic data to the survey. Instead, the input catalogue for the equatorial survey regions was retrospectively replaced with a new photometric catalogue, based on KiDS and VIKING imaging data, as described by Bellstedt et al. (2020a) and Driver et al. (2022).

Throughout this doctoral thesis, all the data products (Sect. 2.5) are taken from GAMA II, with the exception of the stellar mass measurements and uncertainties of Project II, which are based on GAMA III.

2.4 GAMA's main objectives

The main scientific goals that motivated the GAMA joint project are the following:

(i) measurements of DM HMFs down to 10^{12} $M_\odot$. The HMF represents a robust and precise prediction of the ΛCDM model in the *non-linear* regime, as it depends solely on the cosmological parameters, the nature of gravity and the DM particle mass, with negligible dependence on the baryonic physics (e.g. Springel et al. 2005);

(ii) measurement of the recent galaxy merger rate. Although observational measurements of DM halo merger rates are less accurate than predictions by simulations (e.g. Hopkins et al. 2010; Fakhouri et al. 2010), they can still be used to constrain the role of mergers in driving galaxy evolution. Examples include the build-up of stellar mass in galaxies, particularly in today's giant elliptical galaxies (e.g. De Lucia et al. 2006), morphological transformations (e.g. Toomre 1977; Cox et al. 2006; Hopkins et al. 2009), triggering (e.g. Hopkins et al.

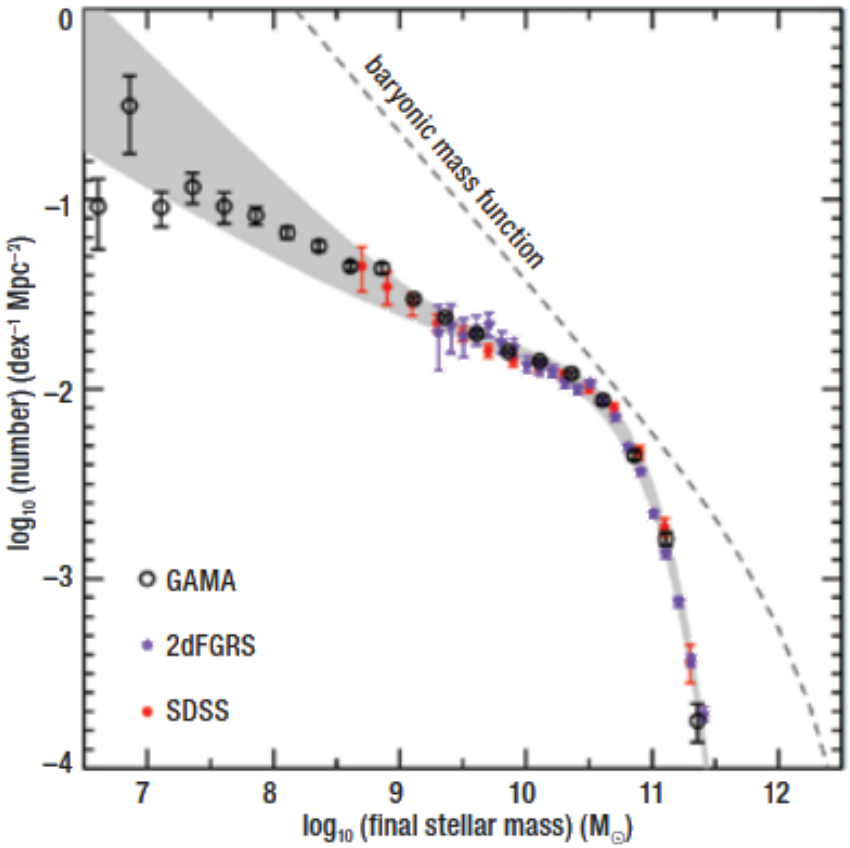

Figure 2.2: The GSMF from various earlier studies, including preliminary results (open circles) and error range (grey shaded region) from the first two years of GAMA I observations (Driver et al. 2009). Also shown as a dashed line is the expected GSMF from numerical simulation coupled with a basic halo occupation distribution model. These two distributions combined fully constrain the SF efficiency.

2013; Patton et al. 2013) and quenching of SF (e.g. Hopkins et al. 2008), fuelling of central supermassive black holes (e.g. Di Matteo et al. 2005; Ellison et al. 2011), and structural evolution (e.g. Naab et al. 2009);

(iii) investigation of SF efficiency and feedback mechanisms. The properties of galaxy population residing in a DM halo depend on both halo mass and baryonic processes. Galaxy formation models generally incorporate feedback mechanisms to account for the observed variation of SF efficiency as a function of halo mass (e.g. Bower et al. 2006; De Lucia et al. 2006). By considering different feedback effects for low- and high-mass halos, these models predict a peak in the stellar-to-halo mass ratio around the mass of the Local Group. GAMA aims to characterize this peak, and thus improve our understanding of feedback mechanisms.

Fig. 2.2 shows the preliminary measurement of the GSMF from GAMA I performed by Driver et al. (2009) and its earlier theoretical prediction (dashed line) from Shankar et al. (2006). The latter represents an attempt to predict the mass distribution of DM halos that host single galaxies, scaled by the global baryon-to-DM density ratio. If SF were equally efficient at all halo masses,

these two functions would mirror each other with a constant baryonic M/L ratio. However, this is clearly not the case. The discrepancy between the two distributions strongly indicates that SF efficiency must vary with halo mass. This seems plausible, as lower-mass haloes struggle to retain their baryons when heated and accelerated by SN winds during episodes of intense SF (Baldry et al. 2008). These results suggest that ∼1% or less of the total progenitor baryonic mass in low-mass halos is converted into stars. Where the remaining ∼ 99% of baryons associated with such systems reside, and in what form they exist, has to be yet fully investigated.

2.5 GAMA data products

2.5.1 Stellar masses

For the stellar mass measurements and uncertainties of Project I we make use of the table *StellarMassesLambdarv24* (Taylor et al. 2011), which provides stellar masses, restframe photometry, and other ancillary stellar population parameters from stellar population fits to multi-band spectral energy distributions for all objects across the five GAMA survey regions. The values in this catalogue were derived using a '737' cosmology and distances that were computed using the flow-corrected redshifts derived from the Tonry et al. (2000) flow model for very low redshifts, and then tapering to a CMB-centric frame for $z > 0.03$, as described by Baldry et al. (2012). The broadband photometry that was modelled in order to derive the stellar masses (in the restframe wavelength range of 0.3 – 1.1 μm) is the LAMBDAR 21-band matched aperture photometry presented by Wright et al. (2016) (and published in the table *LambdarCatv01*).

In this step of the analysis, we corrected the masses derived from this aperture photometry for the light lying outside of the apertures used for the SEDs. Specifically, we made use of the GAMA Sérsic profile fits to our sample. The correction factor, already described in Taylor et al. (2011) and often referred to as the *fluxscale* parameter, is generally equal to $10^{-0.4(\mathrm{m_{total}}-\mathrm{m_{aperture}})}$. In our study, $\mathrm{m_{total}}$ and $\mathrm{m_{aperture}}$ are the r-band magnitudes of the Sérsic model and of the final deblended flux coming from the Sérsic and LAMBDAR photometric catalogues, respectively, and thus the fluxscale parameter simply gives the ratio of total (Sérsic) to LAMBDAR flux. The rescalings for mass values are then given by:

$$\log \mathrm{M_{total}} = \log \mathrm{M} + \log_{10}(\mathrm{fluxscale}). \tag{2.1}$$

Note that the fluxscale parameter introduces an additional source of uncertainty in the total masses. However, following the approach of Vázquez-Mata et al. (2020), we only applied this correction if the fluxscale parameter is in the range 0.8 – 10; otherwise, no correction is applied and $fluxscale = 1$ is assumed. We note that we repeated our analyses with different limits for the correction factor and found that our results do not change qualitatively.

We here point out that since the inception of Project I, the GAMA collaboration has updated both their preferred multi-band photometry, now derived using the the source finding and image analysis software ProFound (Robotham et al. 2018 and published by Bellstedt et al. 2020a), and their preferred method of deriving stellar masses, now using the code ProSpect (Robotham et al. 2020). ProSpect is a generative galaxy spectral energy distribution (SED) package, which

is used to fit the far-UV to far-IR (0.15 – 500 μm; Driver et al. 2016) photometry of GAMA III galaxies. As shown by Robotham et al. (2020), the joint net effect of these changes is a global shift of the stellar masses by +0.1 dex (with a scatter of 0.11 dex), approximately independent of stellar mass. This shift is of course irrelevant when performing purely internal comparisons of the GSMF as a function of different environmental properties (Sect. 6.1) but should be kept in mind when comparing our GSMF to literature values (Sect. 6.2).

Using ProSpect instead of the method presented in Taylor et al. (2011) on the previously preferred LAMBDAR photometry yields systematically higher stellar masses, with a median offset of 0.06 dex and scatter of 0.13 dex. This is attributed to the greater flexibility of ProSpect in modelling star formation history (SFH), allowing for older stellar populations and consequently higher M/L values, which in turn require more stellar mass to reproduce the observed flux (Robotham et al. 2020, Fig. 33). When combining our new ProFound photometry with our new stellar mass estimation method using ProSpect, the offset relative to Taylor et al. (2011) increases to 0.10 dex, with a scatter of 0.11 dex, indicating improved consistency with the data and enhanced sensitivity to older stellar populations (Robotham et al. 2020, Fig. 34).

For the stellar mass measurements and uncertainties of Project II we hence make use of the table *ProSpectv03* (Bellstedt et al. 2020b), which provides stellar masses, star formation rates, metallicities, and dust parameters derived with the ProSpect SED-fitting code for all GAMA III galaxies with a redshift in the equatorial survey regions. The values in this catalogue were derived using $H_0 = 67.8$ km s^{-1} Mpc^{-1}, $\Omega_M = 0.308$ and $\Omega_\Lambda = 0.692$ (consistent with a Planck 15 cosmology: Planck Collaboration XIII 2016).

2.5.2 Group Catalogue

The GAMA Galaxy Group Catalogue (G^{3}C)[2] is one of the major data products of the GAMA project (Robotham et al. 2011). The G^{3}C was constructed by employing a modified Friends-of-Friends (FoF) grouping algorithm that considers galaxies to be in a group if they are 'close' both along the line of sight and when projected on to the sky; this successfully accounts for redshift space distortions caused by the peculiar velocities of galaxies in groups. This FoF algorithm was first run on mock GAMA lightcones in order to tune the grouping parameters and to test the quality of the grouping, before applying it to the real GAMA data.

In particular, we make use of the following tables: (i) *G3CGalv08*[3], which lists the 184 081 galaxies on which the FoF algorithm was run. The exact selection of these galaxies is given by: $nQ \geq 2$, SURVEY_CLASS ≥ 4, and $0.003 < z_{CMB} < 0.6$ (Baldry et al. 2012), as taken from the tables *TilingCatv46* and *DistancesFramesv14*. (ii) *G3CFoFGroupv09*[3], which lists the properties of the 23 654 groups comprising 2 or more members that were identified among the galaxy sample above and which contain ~40% of these galaxies.

[2]We note for completeness that the cosmological parameters used in the construction of the G^{3}C differed somewhat from the model used here: $\Omega_M = 0.25$, $\Omega_\Lambda = 0.75$, $H_0 = 100$ km s^{-1} Mpc^{-1}, corresponding to the cosmology of the Millennium ΛCDM N-body simulations that were used to construct the mock GAMA lightcones.

[3]Newer versions of this catalogue are available, but in order to be more consistent with the Filament Catalogue (see below) we use this slightly older version. In any case, the differences between the version used here and the latest version are irrelevant for both Project I and Project II.

2.5.3 Filament Catalogue

The Filament Catalogue (FC)[4] identifies the LSS in the three equatorial survey regions (Alpaslan et al. 2014). Using a volume-limited subsample of the G^{3}C with a redshift cut of $z \leq 0.213$ and an absolute magnitude cut of $M_r = -19.77 + 5 \log h_{100}$, and discarding all groups with fewer than two members remaining after these cuts, Alpaslan et al. (2014) used the remaining groups as nodes to generate a minimal panning tree (MST), thus identifying 643 individual filaments spanned by 5152 groups. They also introduce other coherent structures on a much smaller scale than filaments, and which are formed entirely by galaxies. These are detected in much the same way as filaments: all unassociated galaxies remaining after the first pass are once again put into another MST. The resulting structures are defined as *tendrils*. Finally, all the galaxies remaining after this second pass define voids. This whole process is described in much greater detail in Sect. 3 of Alpaslan et al. (2014). The 45 468 galaxies of their subsample were then classified as belonging to either filaments, tendrils or voids. However, since we do not want to restrict our analysis to this volume-limited subsample, we will not make use of these classifications here. Instead, we will only use the group-defined filaments and make use of our own environmental classification as described in Sect. 4.1.

The filaments identified in this catalogue are composed of an average of eight groups and span up to $100\,h_{100}^{-1}$ Mpc. In particular, groups in filaments are connected through straight lines called links. All groups that are in the same set of unbroken links are considered to be part of the same filament. Additional substructures are defined within a filament. The backbone refers to the combination of the two paths with the most links that begin from the edges of the filament and meet at its centre, defined as the group which is furthest away from all edges. In other words, the backbone is the longest path that travels from one end of a filament to the other through its most central group. All other paths that are connected to the backbone are referred to as branches, and their order determines how close they are to the backbone. A branch of order n always connects to a branch of order $n-1$, which connects to a branch of order $n-2$, and so on, where the backbone is considered a branch of order 1.

2.5.4 Star formation rates

The Hα emission represents a direct tracer of a galaxy's present-day SFR, reflecting SF activity over short timescales (less than $10-20$ Myr) and being thus minimally affected by the galaxy's past SFH (Kennicutt 1998a). Therefore, for the SFRs we make use of the Hα-derived values as described in Davies et al. (2016).

Following the approach of Hopkins et al. (2003), the stellar absorption-corrected Hα luminosity can be written as:

$$\frac{L_{\mathrm{H}\alpha}}{1\mathrm{W}} = \frac{EW_{\mathrm{H}\alpha} + EW_{\mathrm{c}}}{1\text{Å}} \times \frac{10^{-0.4(M_{\mathrm{r}}-34.1)}}{1\mathrm{W/Hz}} \times \frac{3\times10^{18}\mathrm{Hz}}{6564.1\text{Å}(1+z)^2}\,\frac{1\text{Å}}{1\mathrm{Hz}} \times \left(\frac{F_{\mathrm{H}\alpha}/F_{\mathrm{H}\beta}}{2.86}\right)^{2.36}. \tag{2.2}$$

In the equation above, $\mathrm{EW}_{\mathrm{H}\alpha}$ represents the Hα equivalent width, EW_{c} the equivalent width

[4]The cosmological parameters used in the construction of this catalogue were the same as those used in the construction of the G^{3}C.

correction for stellar absorption, M_r the galaxy rest-frame absolute r-band AB magnitude and $F_{H\alpha}/F_{H\beta}$ the Balmer decrement. Here, we use a single value for the stellar absorption corrections, i.e. $EW_c = 2.5$ Å (Gunawardhana et al. 2011, 2013; Hopkins et al. 2013; Davies et al. 2016). We note that the third factor converts the continuum luminosity from per unit frequency (as determined by the second factor) to per unit wavelength.

In this way, the $SFR_{H\alpha}$ are determined from Kennicutt (1998b) as

$$\frac{SFR_{H\alpha}}{1 M_{\odot} yr^{-1}} = \frac{L_{H\alpha}}{1.27 \times 10^{34} W} \times 1.53, \tag{2.3}$$

where the last factor converts from a Salpeter to a Chabrier initial mass function (IMF) (Driver et al. 2013). $SFR_{H\alpha}$ uncertainties are computed by propagating the observational errors of EW, flux and r-band absolute magnitude in equation 2.2.

We note that ProSpect (see Sect. 2.5.1) provides not only stellar masses but also SFRs. However, we choose to use the Hα-based SFRs rather than the SED-based SFRs from ProSpect, because the bimodality between star-forming and passive galaxies is more clearly defined in the Hα SFR–stellar mass plane than in the SED SFR–stellar mass plane. Consequently, we only use the SED-based SFRs in cases where the Hα-based SFR provides only an inconclusive upper limit (see Sect. 4.5).

3 Sample selection

In this chapter, we describe the selection defining our parent sample of galaxies. The final selection, which results from the application of the redshift-dependent stellar mass limit, is described in Sect. 5.2.

3.1 Parent sample selection

The spectroscopic GAMA observations targeted objects with dust-corrected Petrosian SDSS Data Release 7 (DR7) r-band magnitudes of $r < 19.8$ mag (Baldry et al. 2010). In this context, a redshift quality flag Q was adopted, following the scheme introduced by Colless et al. (2001), such that $Q = 1$ indicates very poor or no redshift, $Q = 2$ a possible but doubtful redshift, $Q = 3$ a probable redshift and $Q = 4$ or 5 a reliable redshift. Liske et al. (2015) then refined this classification by assigning each spectrum a best redshift estimate along with the probability that it is correct; these probability-based redshift quality values are referred to as nQ. If multiple spectra exist for a given source, the redshift from the spectrum with the highest nQ value is selected. The reference table *TilingCatv46* defines the class of each survey target (SURVEY_CLASS) as well as various redshift quality parameters (nQ and nQ2_FLAG, which records the result of tests of $nQ = 2$ redshifts against independent measurements). Our initial sample selection is defined as follows:

(i) Survey regions G09, G12 and G15;
(ii) $r < 19.8$ mag;
(iii) SURVEY_CLASS ≥ 4 to select only main-survey targets, excluding additional filler targets from the sample;
(iv) $nQ \geq 3$ or ($nQ = 2$ and nQ2_FLAG ≥ 1) to select targets with reliable redshifts.

Next, because we make use of the filaments identified by the FC, we apply the same upper redshift cut of $z = 0.213$. Because the various GAMA data products above used slightly different versions of the redshift data (i.e. *TilingCatv46*), small inconsistencies arise between these data products. As a result, our sample does not include one FC group because it is left with no members after our selection criteria were applied. Furthermore, 1088 galaxies catalogued in the G^{3}C with $nQ = 2$ are not included in our sample because of our additional requirement of $nQ2_{\rm FLAG} \geq 1$ (see above). Note that the redshift cut applied above is based on different measurements: for ungrouped galaxies we consider the CMB frame redshift $z_{\rm CMB}$ coming from the table *DistanceFramev14*; for a grouped galaxy we just take the median redshift $z_{\rm FOF}$ of the galaxy's group coming from *G3CFoFGroupv09*. Therefore, either all or none of the galaxies in a group will be considered as being part of our sample.

In Fig. 3.1 we show the distribution of the absolute r-band magnitude as a function of redshift

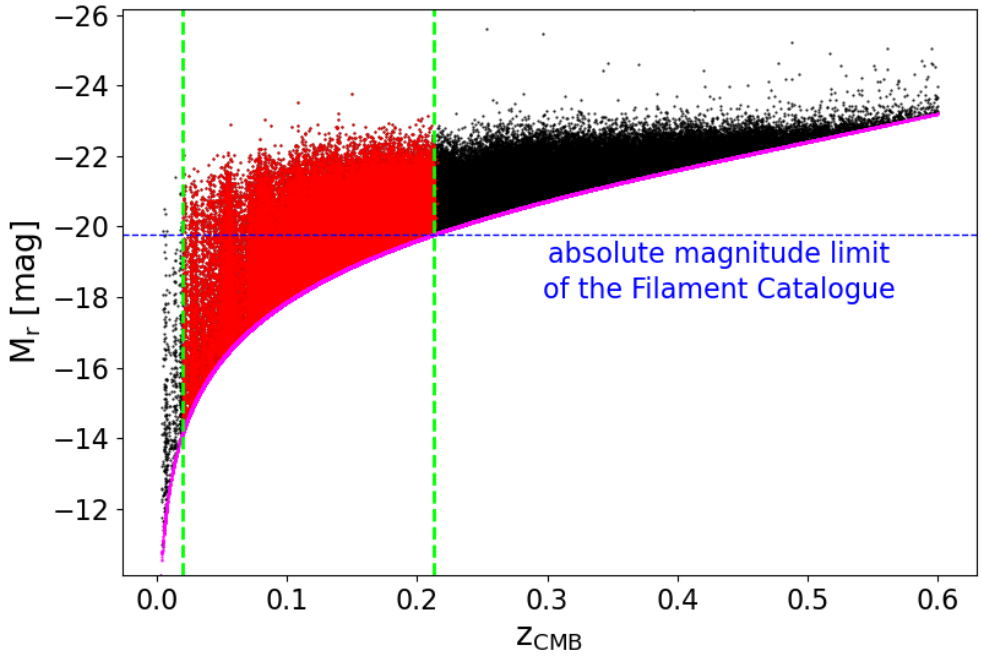

Figure 3.1: Distribution of the absolute r-band magnitude as a function of redshift for all the galaxies in *G3CGalv08* (black points). The magenta curve represents our selection function and gives the faintest possible galaxy that is visible in GAMA at each redshift, given our apparent magnitude limit of $r = 19.8$ mag. Red points show our parent galaxy sample after our initial selection criteria were applied. The two dashed green lines determine our redshift limits (see Sect. 3.2.2 for a discussion of the lower redshift cut). The dashed blue line shows the absolute magnitude cut applied by Alpaslan et al. (2014).

for all the galaxies in *G3CGalv08* (black dots), with the red dots highlighting our parent galaxy sample after our initial selection criteria were applied. In order to determine the faintest possible galaxy that is visible in GAMA at each redshift (shown as a magenta curve in Fig. 3.1), we first calculate the distance modulus DM as a function of redshift using the cosmological luminosity distance D_L:

$$DM = 5\log(D_L) + 25 \tag{3.1}$$

with $D_L = (1 + z)R_0S_k(r)$, where $R_0S_k(r)$ refers to the radial comoving distance, all given in h_{70}^{-1} Mpc. When estimating intrinsic galaxy luminosities, it is necessary to correct for the fact that a fixed observed passband corresponds to a different range of wavelengths in the rest frames of galaxies at different redshifts. This is the so-called k-correction (Humason et al. 1956), which depends on the observed passband, the galaxy's redshift, and its SED. Using the k-correction taken from Robotham et al. (2011), we then calculate the absolute magnitude of the faintest possible galaxy which can be seen within the GAMA survey, given our apparent magnitude limit of $r = 19.8$ mag, as:

$$M_r(z) = 19.8 - DM(z) - k(z) \tag{3.2}$$

This equation describes our initial selection function, i.e. a function that precisely bounds our parent sample data. Unlike Alpaslan et al. (2014), we decided not to apply an absolute magnitude cut here in order to be able to probe the GSMFs more deeply. Our parent galaxy sample now contains a total of 89 451 galaxies across G09, G12 and G15, and 11 820 groups, 5151 of which are part of a filament.

We note that some black dots in Fig. 3.1 are actually still present below the upper redshift cut: these galaxies have $nQ = 2$ and $nQ2\_FLAG = 0$. Also, some red dots lie above the same cut: these 69 galaxies have larger redshifts than 0.213 but belong to a group with a median redshift below this value. According to our selection process, the reverse is also possible but less clear from the plot: 52 galaxies are not included in our final sample, even though they meet all other requirements, because the group they belong to has a median redshift larger than 0.213.

In the rest of this chatper, we now describe two small additional restrictions that have to be applied to our sample.

3.2 Additional sample selection

3.2.1 Stellar mass availability

As part of Project I, we match our spectroscopic galaxy sample with the stellar mass catalogue based on LAMBDAR photometry and Taylor et al. (2011) methodology, as described in Sect. 2.5.1. A small mismatch of 45 galaxies between our spectroscopic and the available stellar mass sample, due to different selection processes, reduces our sample to 89 406 galaxies. Furthermore, this stellar mass catalogue provides the Posterior Predictive P-value (PPP) as a goodness of fit statistic, which can be roughly thought of as a Bayesian analogue to the frequentist reduced χ^2. The PPP is a useful tool for checking whether or to what extent the model is consistent with the data. Given the observed data and the posterior probability density function on the properties of the model, the PPP quantifies the fraction of future observations that would be predicted to be as discrepant as the observed data. Here, we impose a lower limit of PPP ≥ 0.01 in order to discard those galaxies where the data invalidate even the 'most likely' model at 99% confidence. After the PPP cut, our Project I galaxy sample consists of 88 581 total galaxies and 11 789 groups, 5142 of which are part of a filament.

As part of Project II, we match our spectroscopic galaxy sample with the updated stellar mass catalogue derived with the ProSpect SED-fitting code (Sect. 2.5.1). A mismatch of 5778 galaxies between our spectroscopic and the available stellar mass sample, due to different selection processes, reduces our sample to 83 673 objects. Furthermore, the ProSpect catalogue provides the logarithm of the posterior (LP) at the best-fit values as a goodness of fit statistic. In Fig. 3.2 we show the distribution of the LP parameter for our galaxy sample. For LP < -50 we find a small secondary bump in the distribution. A visual inspection of these sources reveals problematic SED fits, often driven by unreliable photometric measurements. This confirms that the model struggles to reproduce the observed data for these objects. Hence, we impose here a lower limit of LP ≥ -50 (dashed red line) in order to discard those galaxies where the data most invalidate the model. After the LP cut, our Project II galaxy sample consists of 83 431 total galaxies, of which

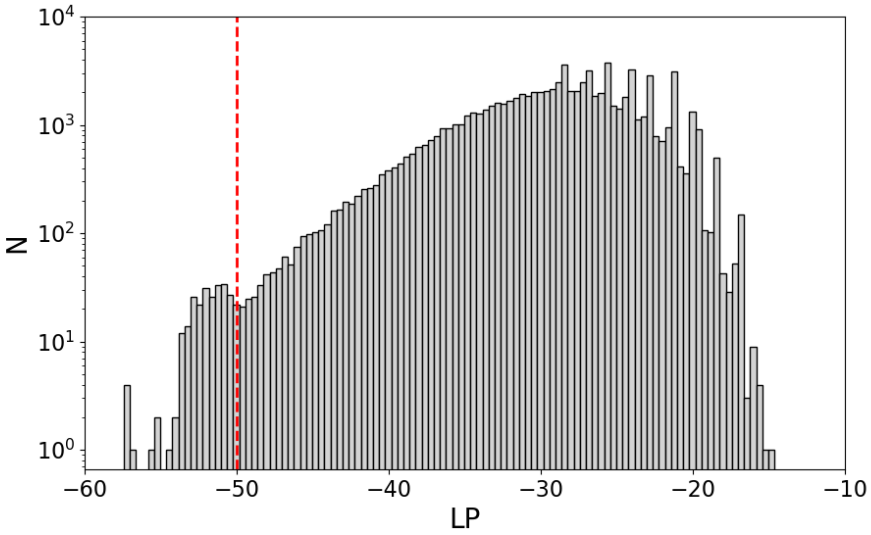

Figure 3.2: Distribution of the LP parameter. The dashed red line marks our lower limit (LP = −50) that has been applied to exclude galaxies with poor SED fits, caused by unreliable photometric data.

37 202 belong to 11 642 groups.

3.2.2 Lower redshift limit

The three panels of Fig. 3.3 show the distribution of our groups in the filaments, i.e. our filamentary structures, across the three GAMA equatorial fields. As one can see, no filament is found at redshifts $z < 0.02$. Below this redshift, the volume is simply not large enough to accommodate a typical filament, and the environment of a galaxy cannot be reliably determined. We thus impose a lower redshift limit of $z = 0.02$ on our sample (Fig. 3.1, left dashed green line), in addition to the upper limit of $z = 0.213$ already applied above. Our Project I final parent sample thus consists of a total of 88 093 galaxies and 11 725 groups, 5142 of which are part of a filament. In comparison, our Project II galaxy sample at this stage comprises 82 981 total galaxies, of which 37 066 belong to 11 579 groups.

3.2.3 Hα star formation rate availability

Another small mismatch of 45 galaxies is found between our spectroscopic sample and the available SFR sample described in Sect. 2.5.4. Our Project II final parent sample thus consists of a total of 82 936 galaxies, of which 37 040 galaxies belong to the same groups.

We summarise the complete selection process of the parent samples for both Project I and Project II in Table 3.1. The final step of the selection process, i.e. the application of the redshift-dependent stellar mass limit, is described in Sect. 5.2.

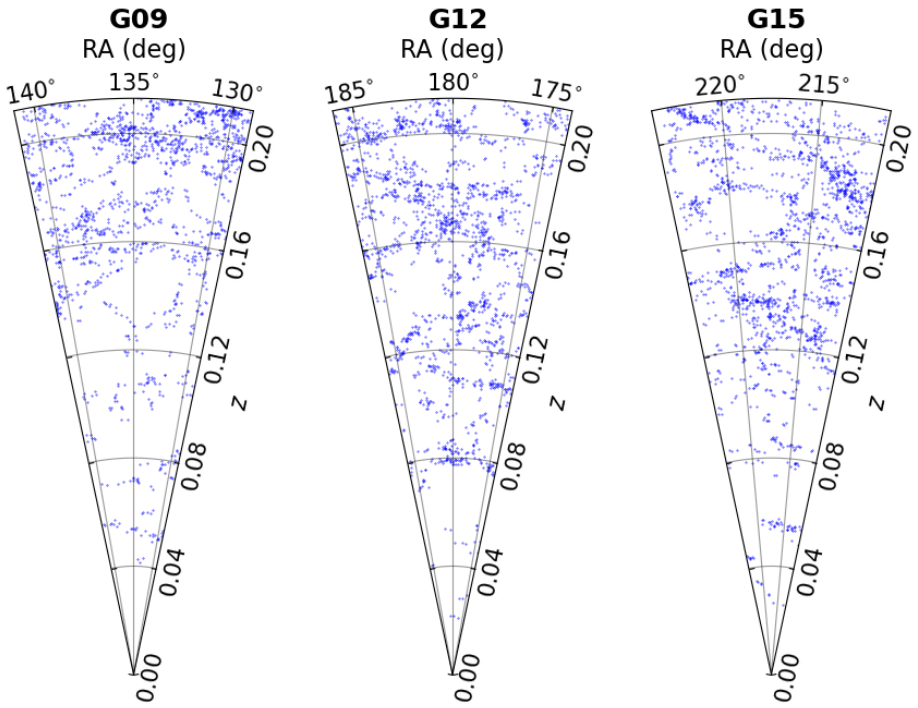

Figure 3.3: Lightcones of the three GAMA equatorial survey regions showing our FC group sample out to $z = 0.213$ (blue dots). All three cones span the full 5° declination range.

Table 3.1: Summary of the parent sample selection process for both Project I and Project II. For each step, we list the selection criterion, the GAMA table used, and the resulting number of galaxies and groups after the selection was applied. Group counts include, in parentheses, either the number of groups in filaments (Project I) or the number of galaxies within groups (Project II).

	Selection step	GAMA table	No of galaxies	No of groups
	$r < 19.8$ mag	*TilingCatv46*	184 081	23 654 (5152)
	$\mathrm{SURVEY_{CLASS}} \geq 4$	*TilingCatv46*		
	$nQ \geq 3$ or ($nQ = 2$ and $nQ2_{\mathrm{FLAG}} \geq 1$)	*TilingCatv46*	182 993	23 652 (5151)
	$z_{\mathrm{CMB}} \leq 0.213$	*DistancesFramesv14*		
	$z_{\mathrm{FOF}} \leq 0.213$	*G3CFoFGroupv09*	89 451	11 820 (5151)
Project I	Stellar mass availability	*StellarMassesLambdarv24*	89 406	11 820 (5151)
	PPP ≥ 0.01	*StellarMassesLambdarv24*	88 581	11 789 (5142)
	$z_{\mathrm{CMB}} \geq 0.02$	*DistancesFramesv14*	88 093	11 725 (5142)
Project II	Stellar mass availability	*ProSpectv03*	83 673	11 645 (37 318)
	LP ≥ -50	*ProSpectv03*	83 431	11 642 (37 202)
	$z_{\mathrm{CMB}} \geq 0.02$	*DistancesFramesv14*	82 981	11 579 (37 066)
	Hα star formation rate availability	*Davies et al. 2016*	82 936	11 579 (37 040)

4 Definition of subsamples

In this chapter, we present our six criteria used to define the different subsamples analysed in this work: the orthogonal distance to the nearest filament $D_{\perp,\mathrm{min}}$ (Sect. 4.1), group membership (Sect. 4.2), group halo mass M_{halo} (Sect. 4.3), a combination of the group's branch order (BO) and the group's number of connecting links (N_{links}; Sect. 4.4), SF activity to distinguish between star-forming and passive galaxies (Sect.4.5), and central/satellite classification (Sect.4.6).

4.1 Orthogonal distance to nearest filament

As discussed in Sect. 2.5.3, from Alpaslan et al. (2014) we only use the filaments identified in the FC but we do not use their galaxy environmental classification. Therefore, we provided our own classification of whether a galaxy is part of a filament or a void, which is simply based on the distance of a galaxy to the nearest filament. In particular, for each galaxy we consider the orthogonal distance to its nearest filament, $D_{\perp,\mathrm{min}}$, as our first criterion used to define the subsamples. Our Project I sample consists of 88 093 galaxies, 39 341 of which are assigned to a group and 48 752 of which are ungrouped (U subsample hereafter); of the grouped galaxies, 23 657 galaxies belong to groups in filaments (G1 subsample hereafter) and the remaining 15 684 galaxies to groups that are not part of a filament (G2 subsample hereafter). All galaxies in G1 are assigned $D_{\perp,\mathrm{min}} = 0$ Mpc by definition. For galaxies in U and G2, we first calculate their 3D Cartesian coordinates and then determine the values of $D_{\perp,\mathrm{min}}$, as we further explain in Sect. 4.1.1. We note that, to diminish the effects of redshift space distortions in this step of the process, the Cartesian coordinates of galaxies in G2 belonging to the same group were derived using the RA and Dec values of the iterative central galaxy, as well as the median redshift of the group as stated in Sect. 3; in this way, all galaxies in a given group end up with the same Cartesian coordinates. In Fig. 4.1 we show the distribution of $D_{\perp,\mathrm{min}}$ for our Project I galaxy sample. As expected, this distribution peaks at $D_{\perp,\mathrm{min}} \approx 2-3\ h_{70}^{-1}$ Mpc and then decreases exponentially. The galaxies in G1 are responsible for the bump at $D_{\perp,\mathrm{min}} = 0$ Mpc.

4.1.1 Orthogonal distance calculation

The calculation of the orthogonal distances to the nearest filament for our galaxy sample requires the determination of their comoving 3D Cartesian coordinates and comoving distances.

The 3D Cartesian coordinates (x,y,z) can be derived from spherical coordinates (r,θ,φ) as

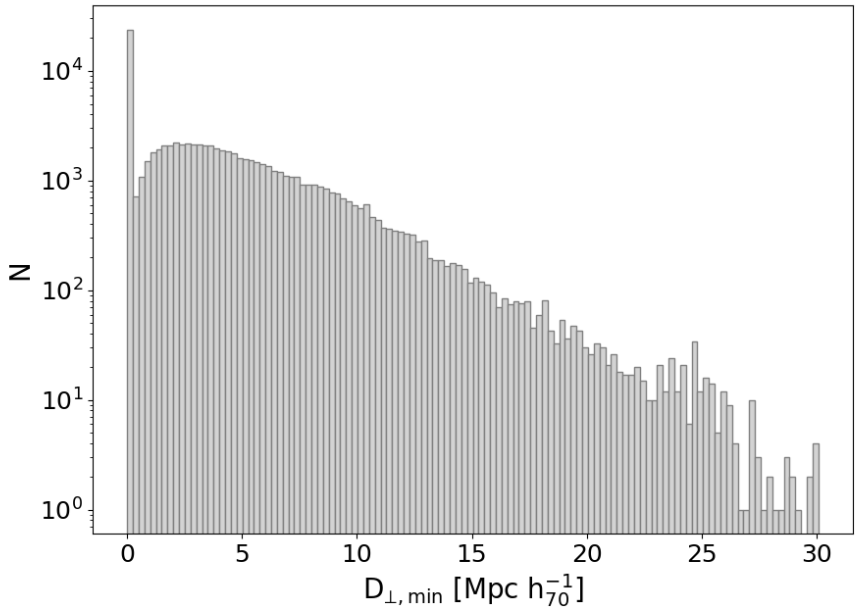

Figure 4.1: Distribution of the orthogonal distance of a galaxy to its nearest filament. The galaxies in subsample G1 (galaxies in groups that are part of a filament) are responsible for the bump at 0 Mpc since they are assigned a value of $D_{\perp,\mathrm{min}} = 0$ by definition.

follows:

$$\mathbf{x} = r \begin{pmatrix} \sin\theta\cos\varphi \\ \sin\theta\sin\varphi \\ \cos\theta \end{pmatrix} = r \begin{pmatrix} \cos\delta\cos\alpha \\ \cos\delta\sin\alpha \\ \sin\delta \end{pmatrix}. \tag{4.1}$$

As shown in Fig. 4.2, r is the radial (i.e. comoving) distance, $\theta = \frac{\pi}{2} - \delta$ is the polar angle, and $\varphi = \alpha$ the azimuthal angle, with δ and α being the declination and the right ascension of the galaxy, respectively. The y-axis initially points at 90 degrees, while the x-axis at 0 degrees. To point the y-axis towards the field center (α_c, δ_c), two additional rotations are applied:

- around the z-axis by an angle $\beta_1 = \frac{\pi}{2} - \alpha_c$, with rotation matrix $\mathrm{R}_1 = \begin{bmatrix} \cos\beta_1 & -\sin\beta_1 & 0 \\ \sin\beta_1 & \cos\beta_1 & 0 \\ 0 & 0 & 1 \end{bmatrix}$;
- around the x-axis by an angle $\beta_2 = -\delta_c$, with rotation matrix $\mathrm{R}_2 = \begin{bmatrix} 1 & 0 & 0 \\ 0 & \cos\beta_2 & \sin\beta_2 \\ 0 & -\sin\beta_2 & \cos\beta_2 \end{bmatrix}$.

The product of these two matrices gives the final rotation matrix, which transforms spherical to Cartesian coordinates:

$$R = R_2 R_1 = \begin{bmatrix} \cos\beta_1 & -\sin\beta_1 & 0 \\ \cos\beta_2\sin\beta_1 & \cos\beta_2\cos\beta_1 & \sin\beta_2 \\ -\sin\beta_2\sin\beta_1 & -\sin\beta_2\cos\beta_1 & \cos\beta_2 \end{bmatrix}. \tag{4.2}$$

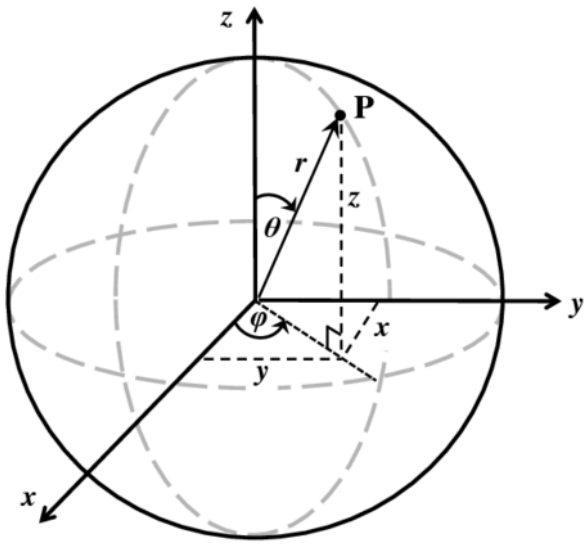

Figure 4.2: Spherical coordinates (r,θ,φ) for a generic point P in space: r is the comoving distance, θ the polar angle, and φ the azimuthal angle. Its Cartesian coordinates (x, y, z) are also shown.

Thus, the Cartesian coordinates in the new reference frame can be written as:

$$\mathbf{x}' = R_2 R_1 \mathbf{x} = r \begin{pmatrix} -\cos\delta \sin\Delta\alpha \\ \cos\delta_c \cos\delta \cos\Delta\alpha - \sin\delta_c \sin\delta \\ \sin\delta_c \cos\delta \cos\Delta\alpha + \cos\delta_c \sin\delta \end{pmatrix}, \tag{4.3}$$

where $\Delta\alpha = \alpha - \alpha_c$. For our methodology, we used $(\alpha_c, \delta_c) = (135.0, 0.0)$ for G09, $(\alpha_c, \delta_c) = (180.0, 0.0)$ for G12, and $(\alpha_c, \delta_c) = (217.5, 0.0)$ for G15. We note that $\delta_c = 0.0$ applies to all GAMA equatorial regions, since their overall declination range is $[-3, 3]$.

In order to obtain the comoving distance as a function of redshift, we first define the *Hubble distance* $d_H = \frac{c}{H_0}$, where c is the speed of light and H_0 is the Hubble constant, and a dimensionless *Hubble parameter* as follows:

$$E(z) = \frac{H(z)}{H_0} = \sqrt{\Omega_r(1+z)^4 + \Omega_m(1+z)^3 + \Omega_k(1+z)^2 + \Omega_\Lambda}. \tag{4.4}$$

In the expression above, Ω_m, Ω_r and Ω_Λ are the normalised present-day densities of matter, radiation, and dark energy, respectively, while $\Omega_k = 1 - \Omega_r - \Omega_m - \Omega_\Lambda$ determines the curvature of the Universe. The comoving distance increment δd_C between two nearby events in the Universe (i.e. close in redshift) is defined as the spatial separation that remains constant over cosmic time if the two objects follow the Hubble flow. It is therefore the appropriate distance measure for probing aspects of large-scale structure imprinted on the Hubble flow. The total line-of-sight comoving distance d_C from the observer to a distant object is computed by integrating the infinitesimal comoving distance contributions δd_C along the comoving path from redshift $z = 0$ to the object's redshift:

$$d_C(z) = d_H \int_0^z \frac{dz'}{E(z')}. \tag{4.5}$$

According to the cosmology adopted throughout this paper, $\Omega_m = 0.30$, $\Omega_r = 0$, $\Omega_\Lambda = 0.70$, and thus $\Omega_k = 0$ (i.e. no curvature or *flat* cosmology). Hence, the comoving distance becomes:

$$d_C(z) = d_H \int_0^z \frac{dz'}{\sqrt{\Omega_m(1+z)^3 + \Omega_\Lambda}}. \tag{4.6}$$

The comoving distance also plays a major role in computing the comoving volume, which is the volume measure in which the number density of non-evolving objects locked into the Hubble flow remains constant with redshift. Since the derivative of the comoving distance with respect to redshift is proportional to $\frac{1}{E(z)}$, the angular diameter distance converts a solid angle $d\Omega$ into a proper area, and two factors of $(1+z)$ convert a proper area into a comoving area. Therefore, the comoving volume element in solid angle $d\Omega$ and redshift interval dz is defined as:

$$dV_c(z) = d_H \frac{(1+z)^2 d_A(z)^2}{E(z)} d\Omega dz, \tag{4.7}$$

where $d_A(z) = \frac{d_M(z)}{1+z}$ is the angular diameter distance, and $d_M(z) = d_C(z)$ is the transverse comoving distance in case of $\Omega_k = 0$. Thus, the total all-sky comoving volume out to redshift z is given by integrating the comoving volume element from the present time to redshift z:

$$\begin{aligned} V_C(z) = \int_0^z dV_C(z') = \int_0^{4\pi} d\Omega \int_0^z d_H \frac{d_M^2(z')}{E(z')} dz' = \\ = 4\pi \int_0^z d_H \frac{d_C^2(z')}{E(z')} dz' = \frac{4\pi}{3} d_C^3(z), \end{aligned} \tag{4.8}$$

where the final expression only holds for $\Omega_k = 0$.

4.2 Group membership

A galaxy's membership of a group or not, as defined by the G^{3}C in Sect. 2.5.2, represents our second criterion used to define the subsamples. As described above, this categorical classification comprises 39 341 grouped galaxies (G1 + G2 subsamples) and 48 752 ungrouped galaxies (U subsample).

4.3 Group halo mass

As in Vázquez-Mata et al. (2020), we make use of two different methods for estimating a group's halo mass $M_{\rm halo}$, which represents our third criterion used to define the subsamples. The first method provides a dynamical mass estimate, $M_{\rm dyn}$, based on the virial theorem and the galaxy dynamics within each group; the second provides a luminosity-based mass estimate, $M_{\rm lum}$, using the group's total r-band luminosity and the weak-lensing calibrated M-L relation of Viola et al. (2015, Equation 37). As discussed in Robotham et al. (2011), the total group r-band luminosity is not simply the sum of the luminosities of all galaxies belonging to that group, but is instead

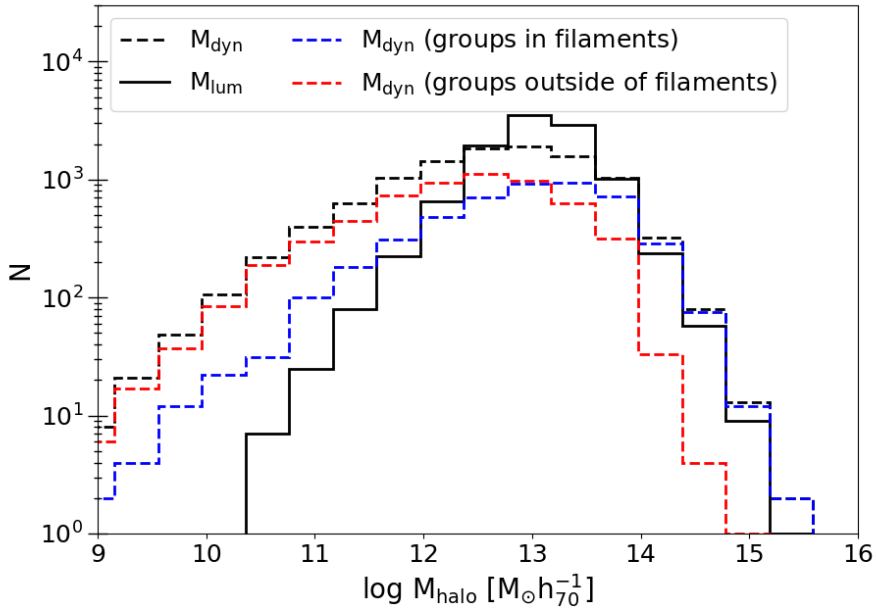

Figure 4.3: The black solid an dashed lines show the distributions of the luminosity-based and dynamical halo mass estimates for our Project I group sample, respectively. The blue and red dashed lines show the distributions of the dynamical halo mass estimates for those groups that are part of a filament and those that are not, respectively.

corrected for the fraction of light in galaxies below the survey magnitude limit using the global GAMA luminosity function. Since most of the luminosity is contributed by galaxies around $L^\star$, and since most GAMA groups are sampled well beyond $L^\star$ due to the survey's depth of $r < 19.8$ mag, these corrections typically amount to only a few percent.

The G^{3}C provides the dynamical group halo masses, both using a constant calibration factor of $A = 10.0$ required to get a median unbiased mass estimate (column `MassA`), as well as using a calibration factor that is a function of group multiplicity and redshift (column `MassAfunc`). Also listed are the group r-band luminosities integrated down to an absolute magnitude of $M_r - 5 \log h_{100} = -14$, again both considering a constant calibration factor of $B = 1.04$ for the median unbiased luminosity estimate (`LumB`), and its functional form (`LumBfunc`). See Sects. 4.3 and 4.4 of Robotham et al. (2011) for detailed explanations of these different calibration factors.

In Fig. 4.3 we show the halo mass distribution of our Project I group sample using both the dynamical estimate (black dashed line) and the luminosity-based one (solid line). Our groups mainly reside in haloes of 10^{12}–10^{14} $M_\odot$ h_{70}^{-1}. Moreover, the dynamical mass estimates have a broader distribution towards lower masses compared to the luminosity-based ones, as already noted by Han et al. (2015) and Vázquez-Mata et al. (2020). We also show as blue and red dashed lines the dynamical halo mass distributions of the groups that define the filaments and those that lie outside of the filaments. Although there is an almost complete overlap, these distributions are nevertheless quite different, with the groups in filaments clearly being more massive. In fact, the

group sample is dominated by the filament groups at halo masses $M_{\rm dyn} \gtrsim 10^{13}\ M_\odot\ h_{70}^{-1}$, and by the groups outside of filaments below that value.

As we discuss below in Sects. 6.1 and 6.2, Project I shows that the dynamical group halo masses yield more conclusive results. Moreover, the findings are largely insensitive to the particular dynamical halo mass estimator used (Figs. 6.6 and 6.8). Thus, in Project II we only make use of `MassAfunc` in studying the dependence of the GSMF on group halo mass, as it explicitly accounts for group multiplicity and redshift.

4.4 Group branch order and number of connecting links

In the FC, 656 filaments spanned by 5152 groups were identified across the three equatorial GAMA regions. As explained in Sect. 2.5.3, a filament is defined as a collection of branches. Each branch, and therefore each group within a branch as well as each galaxy within those groups, can be assigned a branch order (BO). In particular, groups with BO = 1 define the backbone; groups with BO = 2 belong to a second-order branch (connected to the backbone); and so on. The backbone and all the other branches of a filament make up its morphology, with the backbone representing the most central route through the filament, and the other branches being paths that emerge from the backbone.

Apart from the order of its branch, the position of a group within its filament can be further characterised by its total number of links to neighbouring groups, $N_{\rm links}$. A group at the end of its branch has $N_{\rm links} = 1$, a group in the middle of a branch has $N_{\rm links} = 2$, while a group belonging to multiple branches has $N_{\rm links} > 2$. To obtain a comprehensive picture of how much a group is embedded in a denser (or less dense) part of a filament, we consider both its BO and its $N_{\rm links}$, the combination of which represents our fourth criterion used to define the subsamples.

4.5 Selecting star-forming/passive galaxies

In the literature, several approaches provide a separation between blue, star-forming, and red, passive galaxies, based on colour, SFR, morphology, or other galactic properties (Davies et al. 2019a). A common method, for instance, relies on specific colour cuts (Bell et al. 2003; Baldry et al. 2004; Peng et al. 2010).

However, at lower stellar masses, dust attenuation and complex SFHs make this distinction more problematic. To address this issue, Taylor et al. (2015) develop a statistical model that describes the observed galaxy distribution as the sum of two overlapping components, referred to as *R-type* and *B-type*, each defined by its own stellar mass function, color-mass relation, and intrinsic scatter. After correcting for dust, B-type (star-forming) galaxies show nearly constant intrinsic colours across a wide range of stellar masses, indicating relatively uniform stellar populations. In contrast, R-type (passive) galaxies show a strong correlation between colour and mass, with lower-mass R-type galaxies becoming progressively bluer, suggesting younger stellar populations or recent quenching events. In particular, a well-defined red sequence of passive galaxies emerges clearly only above a stellar mass of $10^{10.5} M_\odot$. Below this mass, the distinction

between the two populations becomes increasingly ambiguous. Therefore, Taylor et al. (2015) show that the previously observed differences between red and blue galaxy populations arise from inconsistent and arbitrary definitions, as hard cuts in CMDs lead to contamination and incompleteness, particularly at low masses where the two populations significantly overlap. While this method is flexible and highly effective, it is challenging to apply, as it consists of a complex 40-parameter probabilistic model tuned for nearby $z < 0.12$ galaxies.

Interestingly, Davies et al. (2019b) use a distinction based on an offset from the star-forming sequence (SFS). More precisely, they first consider a preliminary division at $\mathrm{SFR}/M = 10^{-10.5}\ \mathrm{yr}^{-1}$; then, they perform two different least-square regression fits to galaxies above and below this threshold (defining the star-forming and passive fits, respectively); finally, they identify the minimum density points along cross-sections perpendicular to the two fits, and the interpolation of those minima is taken as the final dividing line. The choice not to consider a separation at 1 dex below the SFS, as performed in other previous works, is due to the fact that within GAMA the SFS and the passive cloud show two different slopes. Therefore, this approach just provides a more robust division between the two populations.

Here, we implement the separation between SF and passive galaxies, which represents our fifth criterion used to define the subsamples, following a similar approach to that of Davies et al. (2019b). Since we do not want to be limited to their fixed, somewhat arbitrary initial division at $\mathrm{SFR}/M = 10^{-10.5}\ \mathrm{yr}^{-1}$, we here implement an iterative procedure. At each iteration, the two regression fits and the dividing line are redetermined, using the current dividing line to define the star-forming and passive samples for the next step. The process continues until the dividing line converges, with a tolerance of 10^{-2}. This slightly modified approach gives a final dividing line between the star-forming and passive populations which is independent of the choice of the initial division. In Fig. 4.4 we show the distribution of our Project II parent sample in the $\log M - \log \mathrm{SFR}$ plane, split by star-forming (cyan dots) and passive (pink dots) galaxies. The star-forming and passive fits are marked as dashed blue and red lines, respectively, whereas the green solid line represents our final division. The density contours in Fig. 4.4 show that the dividing line accurately follows the minimum ridge. Our procedure yields a final separation that is very similar to the one obtained by Davies et al. (2019b).

We note that the black dots identify the 242 sources with $\mathrm{LP} < -50$ (Sect. 3.2.1): this is to show that, since they are distributed approximately randomly in the $\log M - \log \mathrm{SFR}$ plane, their exclusion from our Project II sample is expected not to introduce any bias.

We also note that for 4165 galaxies our Hα-based SFR measurements provide only an upper limit. Among these, 128 have an upper limit that lies above our dividing line, and therefore their classification is uncertain. For these galaxies, we use the SED-based SFR measurements from ProSpect instead. This results in 51 of these 128 galaxies being classified as star-forming. The remaining 77 galaxies are classified as passive.

From our total parent sample of 82 936 objects, we thus identify 55 914 star-forming and 27 022 passive galaxies. Of these, 20 769 and 16 271 are grouped galaxies, respectively.

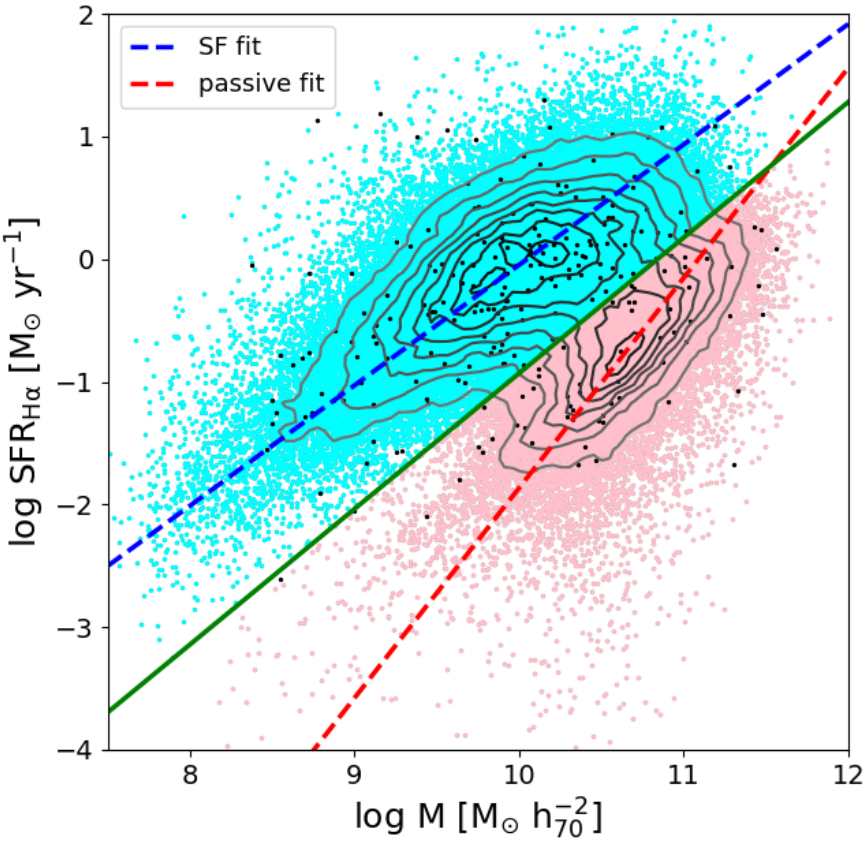

Figure 4.4: Selection of star-forming and passive galaxies using the log M − log SFR plane. The dashed blue and red lines display the star-forming and passive population fits, respectively, whereas the solid green line displays our final dividing line. Star-forming galaxies are shown in cyan and passive galaxies in pink. Black dots refer to the 242 sources with with LP < −50 (Sect. 3.2.1).

4.6 Grouped central and satellite galaxies

The G^{3}C provides two different approaches for the determination of the central galaxy in a group. In particular, the catalogue identifies the source with the highest r-band luminosity (i.e. the brightest group galaxy, or BGG hereafter) and the source closest to the iterative centre of the group. This centre is defined through an iterative procedure where, at each iteration, the r-band centre of light is calculated and the most distant galaxy rejected until only two galaxies remain. Then, the brightest r-band galaxy is selected as central. See Sect. 4.2 of Robotham et al. (2011) for detailed explanations. Despite these two approaches producing similar results, Robotham et al. (2011) show that the iterative method always offers the most accurate agreement with the exact group centre. Therefore, as done by Vázquez-Mata et al. (2020), we adopt this strategy to identify the central galaxy in each group, i.e. to distinguish between grouped central and satellite galaxies, which represents our final criterion used to define the subsamples.

From our Project II final sample of 37 040 grouped galaxies, the iterative procedure identifies 11 038 centrals and 26 002 satellites. We here highlight that ~97% of those centrals are also BGGs. Therefore, we do not expect our results to differ when selecting centrals according to the BGG approach.

5 Method

In this chapter, we describe the methods we used in our work: the Modified Maximum Likelihood estimator for the construction of the GSMFs (Sect. 5.1), the stellar mass completeness limit for the derivation of the selection function (Sect. 5.2) and the random sample generation for the application of volume corrections to the GSMFs (Sect. 5.3).

5.1 Modified Maximum Likelihood estimator

Massive galaxies are much rarer compared to low-mass ones. In a fixed cosmic volume, the number of galaxies per unit mass decreases with mass according to a power law until reaching a specific cut-off, beyond which the number density falls off exponentially. To characterize this behaviour, it is helpful to define the GSMF $\phi(M)$ as the density of galaxies per unit volume and per unit stellar mass M. Specifically, in a given cosmic volume dV, the expected number of galaxies within the interval $[M, M + dM]$ is given by $dN = \phi(M)dVdM$. Analytical parametric functions intended to match observed GSMFs can be expressed in the form $\phi(M|\boldsymbol{\theta})$, where $\boldsymbol{\theta}$ denotes a vector of P scalar model parameters. The Schechter function (Schechter 1976) represents the most well-known model accurately capturing the truncated power-law behaviour:

$$\phi(M)dM = e^{-\frac{M}{M^\star}}\phi^\star\left(\frac{M}{M^\star}\right)^\alpha \frac{dM}{M^\star}. \tag{5.1}$$

Here, $\phi^\star$ is the normalisation factor, $M^\star$ is the mass at the normalisation point (i.e. near the exponential break), and α is the faint-end slope parameter. However, the shape of the GSMF is not always well represented by a single Schechter function due to an often observed steepening below $10^{10}\ M_\odot$, giving rise to a double Schechter function (Baldry et al. 2008):

$$\phi(M)dM = e^{-\frac{M}{M^\star}}\left(\phi_1^\star\left(\frac{M}{M^\star}\right)^{\alpha_1} + \phi_2^\star\left(\frac{M}{M^\star}\right)^{\alpha_2}\right)\frac{dM}{M^\star}, \tag{5.2}$$

where $\phi_1^\star$, $\phi_2^\star$ and α_1, α_2 describe the normalization and slope parameters, respectively, for the two components. Without loss of generality, we can always choose $\alpha_1 > \alpha_2$ such that the second term in Equation 5.2 dominates at lower masses (Baldry et al. 2012). This shape is also supported by abundance matching between the theoretically predicted HMF and the observed GSMF (Marinoni & Hudson 2002; Shankar et al. 2006; Baldry et al. 2008; Conroy & Wechsler 2009; Guo et al. 2010; Moster et al. 2010). Despite its widespread use, this parametrisation has several important limitations. In particular, the Schechter parameters are strongly correlated and sensitive to the limiting magnitude adopted in the fit (Croton et al. 2005). Therefore, it should only be used when

the Schechter function provides a good representation of the data and the fit is performed over a consistent and appropriate magnitude range.

The most straightforward and intuitive technique for fitting a GSMF model, as described in Schmidt (1968), is to estimate the observed space densities for different mass intervals of the data. This is achieved by computing for each mass interval the ratio between the number of detected galaxies and the maximum volume $V_{\rm max}$ in which galaxies of that mass could have been observed. This procedure is also known as $1/V_{\rm max}$ method. The model function $\phi(M|\boldsymbol{\theta})$ is then fitted to these values. However, this method has several drawbacks: the fitting process is influenced by the division into arbitrary mass intervals; Poisson errors cannot be assigned to non-detections (i.e. mass intervals with no galaxy); the choice of $V_{\rm max}$ is sometimes uncertain due to complex detection limits with source-dependent completeness; and systematic errors can be introduced by the cosmic LSS. Just observing more galaxies will not solve most of these limitations, which indeed remain a pertinent issue for modern spectroscopic redshift surveys (York et al. 2000; Colless et al. 2001; Drinkwater et al. 2010; Grazian et al. 2015; Liske et al. 2015; Davidzon et al. 2017).

In this study, we hence employ the modified maximum likelihood (MML) estimation, which was comprehensively documented by Obreschkow et al. (2018). This method bypasses the need for data binning and operates within a Bayesian framework tailored for fitting distribution functions (e.g. GSMFs) to complex multi-dimensional datasets. The MML framework meticulously takes into account the observational measurement errors for individual objects, incorporates complex observational selection functions, and provides the option to internally correct for the underlying LSS detected within the survey volume. The core of the MML approach consists of a fit-and-debias procedure, an iterative fitting algorithm that iteratively solves a standard maximum likelihood estimation, revising the data by accounting for the previous fit and observational uncertainties. The MML framework is accessible via `DFTOOLS` (Obreschkow et al. 2018), an open-source software package for the `R` statistical programming language. `DFTOOLS` gives the most likely solution and full co-variance matrix of the relevant model parameters in order to derive volume-corrected binned mass functions.

For Project I, we adopt a double Schechter function (Equation 5.2) throughout, which has been demonstrated to effectively address the notable upturn observed at intermediate stellar masses (Baldry et al. 2008).

When distinguishing between star-forming and passive galaxies, as done in Project II, the functional shape of the GSMF may differ between the two populations. Peng et al. (2010) show that in their model environmental quenching alone results in a single Schechter function with the same shape as the mass function of blue galaxies, whereas, when both environmental and mass quenching mechanisms are included, the resulting mass function of red galaxies follows a double Schechter. Following the approach of Weigel et al. (2016), we do not impose any a priori assumptions about the functional form. Instead, we allow each GSMF to be represented by either a single or a double Schechter function. Specifically, we estimate the likelihoods of both functional forms for our star-forming and passive galaxy samples (see Sect. 4.5). The likelihood ratio then determines which functional form provides the best fit. We note that the double Schechter function yields a notably better fit to our data. For this reason, we adopt it as the preferred functional form to describe $\phi(M)$ across both our star-forming and passive populations.

5.2 Stellar mass completeness limit

One of the most crucial steps in properly estimating the number density $\phi(M)$ consists in the derivation of $M_{\rm lim}(z)$, which represents the stellar mass limit above which our sample is complete at a given redshift, and which depends both on redshift and the stellar mass-to-light M/L distribution of the sample, given our flux-limited sample.

The determination of the stellar mass completeness limit is particularly challenging for a flux-limited sample like those of Project I and Project II, since a sharp limit in luminosity does not correspond to a sharp limit in stellar mass, as shown in Fig. 5.1. Taking a narrow redshift range (dashed black lines, top panel) and simply using as a mass limit (solid green line, bottom panel) the mass that corresponds to the luminosity limit and the average M/L (respectively, solid blue and dashed cyan line, bottom panel) would result in an incomplete sample, since all the massive yet lower-luminous sources falling below the absolute magnitude cutoff are already missing from the sample. Therefore, it is necessary to move the mass limit sufficiently upwards (dashed green line, bottom panel) to reduce the incompleteness to an acceptable level.

Different strategies for the estimation of $M_{\rm lim}(z)$ can be found in the literature. For example, the approach presented in Dickinson et al. (2003), Fontana et al. (2006), Pérez-González et al. (2008) and others rely on a single stellar population (SSP) paradigm; the minimum stellar mass of a galaxy with magnitude equal to the magnitude limit $r_{\rm lim}$ can be estimated by scaling the flux of a synthetized spectrum of a passively evolving SSP formed at high redshift. The technique introduced by Marchesini et al. (2009a) considers deeper survey data, where the flux and mass of each object are scaled to match $r_{\rm lim}$; in this context, the most massive sources have the lowest M/L and can therefore be excluded by simply applying $r_{\rm lim}$ as a cut. Quadri et al. (2012) and Tomczak et al. (2014) use a slightly modified version of this approach, by considering the objects above the flux completeness and scaling their masses and fluxes down to $r_{\rm lim}$; the upper limit of those scaled-mass values defines their mass completeness limit as a function of redshift.

For both Project I and Project II, we followed the approach presented by Pozzetti et al. (2010) and illustrated in Fig. 5.2. For each galaxy in our final parent sample, we first consider $M_{{\rm lim},i}$, that is, the mass that source i would have if it had the same M/L_r but a magnitude equal to our spectroscopic magnitude limit of $r_{\rm lim} = 19.8$ mag. In Fig. 5.2 we show the resulting distribution in $M_{{\rm lim},i}$ which reflects that of the $M_i/L_{r,i}$ at each redshift in our Project I galaxy sample. In other words, $M_{{\rm lim},i}$ is M/L_r dependent. Under the assumption of a constant M/L_r, $M_{\rm lim,i}$ is simply given by

$$\log(M_{{\rm lim},i}) = \log(M_i) + 0.4(r_i - r_{\rm lim}). \tag{5.3}$$

Next, we divided our sample into 20 bins of comoving distance d and then, in each bin, sorted all sources by magnitude, selecting the 20% faintest galaxies (shown in red in Fig. 5.1). For each bin, we defined $M_{\rm lim}$ as the upper envelope of the $M_{\rm lim,i}$ distribution, below which 95% of these faint objects lie. The function $M_{\rm lim}(d)$ was then determined by fitting an exponential curve to the estimated mass limits in each bin defined as

$$\log[M_{\rm lim}/(M_\odot\, h_{70}^{-2})](d) = a\log[d/({\rm Mpc}\, h_{70}^{-1})] + b, \tag{5.4}$$

with a and b being the free parameters. The fit resulted in $a = 1.0668$ and $b = 3.1956$. This $M_{\rm lim}(d)$ therefore corresponds to the 95% completeness limit of the M/L_r distribution of the 20%

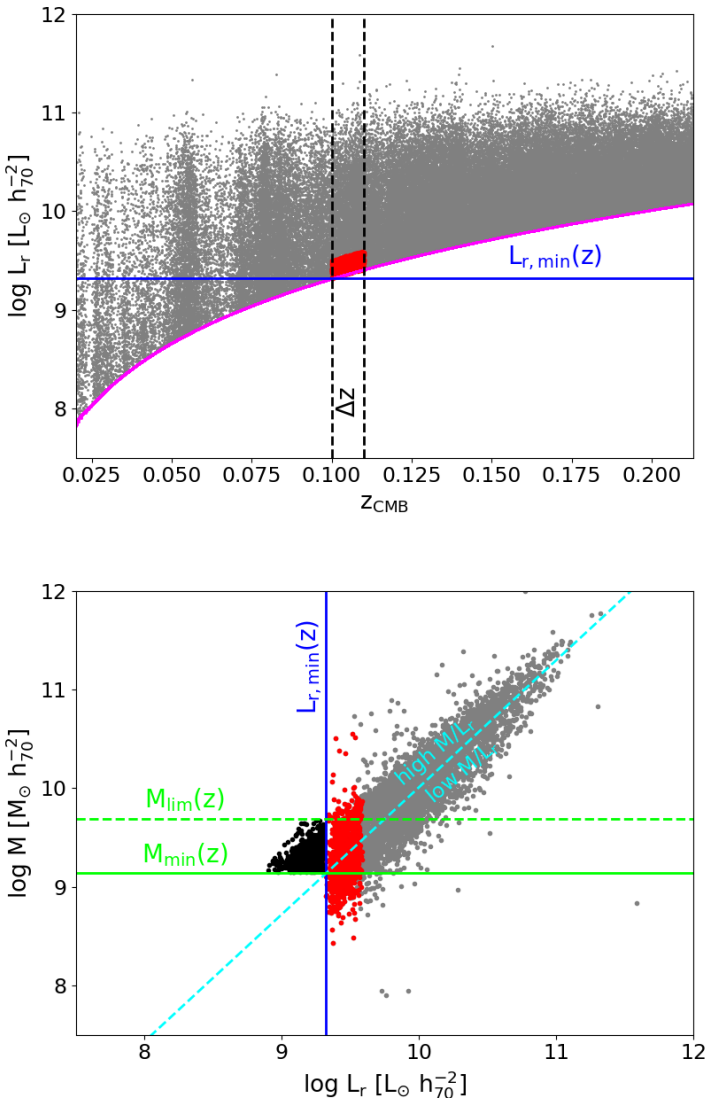

Figure 5.1: Top panel: Distribution of the total r-band luminosity as a function of redshift for our Project I parent galaxy sample (grey dots). The magenta curve represents our selection function and gives the lowest luminosity of a galaxy for which a redshift could have been collected in GAMA, given our apparent magnitude limit of $r = 19.8$ mag. The two dashed black lines define a narrow redshift range Δz for illustrative purposes. The solid blue line and the red box correspond to the luminosity limit and the 20% faintest galaxies associated with this redshift range, respectively. Bottom panel: Stellar mass vs. r-band luminosity for the galaxy subsample in the narrow redshift range, Δz, defined in the top panel. The dashed cyan line gives the average correlation between the two galactic properties. Galaxies lying above this line have a higher than average M/L_r and vice versa. The luminosity limit from the top panel is also shown here in blue. The intersection of this limit with the average correlation defines the corresponding mass limit at this redshift shown as a solid green line. However, this mass limit would not in fact result in a complete sample as all galaxies to the left of the blue line, shown in black, would be missed. To be complete, it is necessary to move the mass limit up sufficiently such that (almost) no more galaxies are missed. The dashed green line thus gives the final stellar mass limit, representing the 95% M/L_r completeness limit of the 20% faintest galaxies at this redshift (see text).

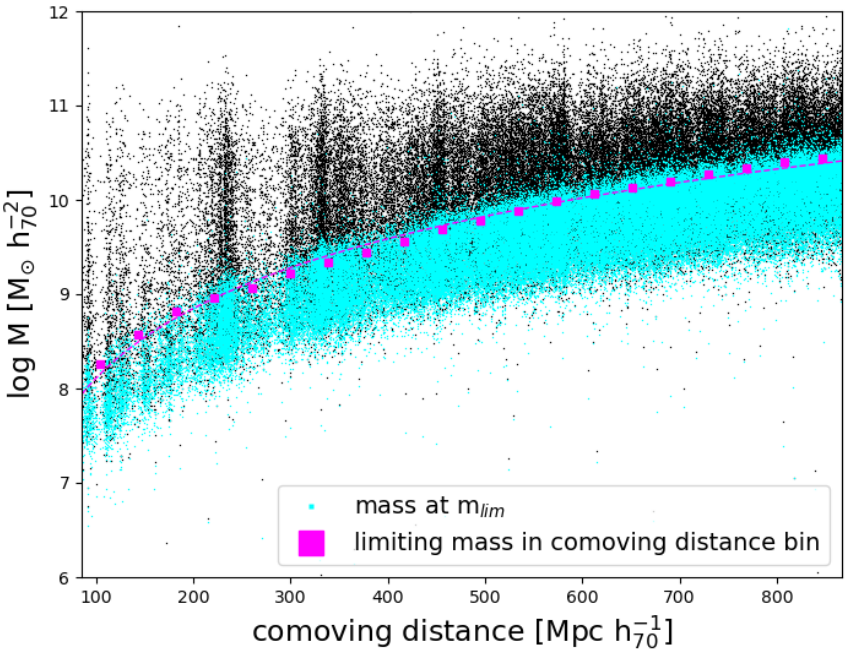

Figure 5.2: Determination of the stellar mass completeness limit as a function of comoving distance for our Project I galaxy sample (black dots). Due to the range in M/L_r, constraining the mass completeness limit of a flux limited sample is not straightforward. By keeping the M/L_r and the redshift of each source constant, we determined the stellar mass that each object would have if its flux was equal to the flux limit. These limiting mass values are shown in cyan, with higher dots at a given redshift having larger M/L_r values. We then divided our sample into bins of comoving distance, sorted the sources in each bin according to their luminosity, selected the faintest 20%, and determined the stellar mass below which 95% of these faint objects lie (Pozzetti et al. 2010). We repeated this procedure for each bin and thus obtained the limiting mass values that are shown as magenta squares. The mass completeness function $M_{\rm lim}(d)$, shown as the magenta dashed line, was then estimated by fitting an exponential curve to these limiting mass values in each comoving distance bin.

lowest-luminosity galaxies at each redshift and represents the selection function for our sample (shown as the magenta dashed line in Fig. 5.2).

Unavoidably, however, the (small) remaining incompleteness of the sample thus selected is not random. Instead, it depends on luminosity and M/L_r, with faint, high-M/L_r galaxies most affected. Since any subsample of galaxies that we might choose to select below may have an L_r-M/L_r distribution that is slightly different from that of the full sample (at a given redshift), the incompleteness of this subsample will also be slightly different from that of the full sample. This could be avoided by re-determining $M_{\rm lim}$ individually for each subsample. However, this would result in the union of a complete set of subsamples not necessarily being identical to the full sample, and these subsamples covering slightly different volumes, which may in turn result in slightly different LSS corrections. In practice, however, we found that the two methods produce

essentially the same results for all of our subsamples in Project I. For simplicity, we hence use the same selection function for all subsamples adopted in Project I.

The sample was restricted to the galaxies that lie above this curve. This results in our Project I final sample of 52 089 galaxies (59% of the parent sample defined in Sect. 3) and 10 429 groups. We note that when referring to any of our Project I subsamples below, in particular the samples G1, G2 and U defined in Sect. 4.1, these samples should be understood to have had the selection function shown in Fig. 5.2 applied to them.

For the purposes of Project II, by contrast, it would be inappropriate to adopt the selection function of the full sample as representative for the subsamples discussed in Sect. 4, since each of these exhibits its own L_r–M/L_r distribution, resulting in different levels of incompleteness. Unlike in Project I, we thus re-derive $M_{\rm lim}(z)$ individually for each subsample, that is, we adopt distinct selection functions for star-forming and passive galaxies (Sect. 4.5) as well as for centrals and satellites (Sect. 4.6). In practice, however, we find that using a single selection function (that of the full sample) produces essentially the same results.

Finally, for both Project I and Project II, we amended our selection function at the lowest redshifts by requiring $\log[M/(M_\odot\, h_{70}^{-1})] > 8.3$ (cf. Fig. 5.2) because we found our mass function measurements below this value to be unreliable for many of the subsamples that we investigate in Sects. 6.1 and 7.1.

To measure a given sample's GSMF, we input the selected galaxies' comoving distances, stellar masses, stellar mass errors, selection function, and desired functional form to fit (i.e. double Schechter) into the `DFTOOLS` routine `DFFIT`. We note that the code computes both the functional fit as well as the full covariance matrix for the fitted parameters.

5.3 Random sample generation

The content of this section applies exclusively to our Project I final sample, as defined in Sect. 3.

The general mass function of filament galaxies just considers all the galaxies in filaments, using the total survey volume, and describes the overall average density of galaxies living in filaments. In contrast, the 'conditional' GSMF (cGSMF hereafter) represents the local density of galaxies in filaments, given that they are a member of a filament. To see how the local density of galaxies changes as a function of environment, we need to know which fraction of the total survey volume is occupied by filaments (assuming a certain radius) and voids. To this end, we distribute a random sample of points in the total survey volume and then ask which fraction of this sample lies within various environments.

At this stage of the analysis, we employ a method for generating points uniformly within the solid angle defined by the survey boundaries, i.e. within the limits in right ascension, $\alpha_{min} \leq \alpha \leq \alpha_{max}$, and declination, $\delta_{min} \leq \delta \leq \delta_{max}$. The starting point is the definition of the differential element of solid angle: $d\Omega = \cos\delta, d\delta, d\alpha$. The right ascension is just *uniformly* distributed between the upper and lower bounds $\alpha \sim U(\alpha_{min}, \alpha_{max})$. The declination, however, is not uniformly distributed, because the area covered at an angle δ goes as $\cos\delta$. If $\mathrm{dP} \propto \cos\delta \mathrm{d}\delta$ represents the probability of finding an object in a small range of declinations, then the cumulative distribution function (CDF)

of selecting a point at a specific declination is given by:

$$P(\delta) = \frac{\int_{\delta_{min}}^{\delta} \cos\delta' d\delta'}{\int_{\delta_{min}}^{\delta_{max}} \cos\delta' d\delta'} = \frac{[\sin\delta]_{\delta_{min}}^{\delta}}{[\sin\delta]_{\delta_{min}}^{\delta_{max}}} = \frac{\sin\delta - \sin\delta_{min}}{\sin\delta_{max} - \sin\delta_{min}}.$$

This CDF maps declination δ to a uniform random variable $v \in [0, 1]$, i.e. $P(\delta) = v$. Solving this expression for δ gives the inverse CDF mapping v to the declination:

$$\delta = \arcsin(v(\sin\delta_{max} - \sin\delta_{min}) + \sin\delta_{min}).$$

The desired distribution in declination is then realized by letting v to be *uniformly* distributed between 0 and 1: $v \sim U(0, 1)$. This is equivalent to $\delta = \arcsin(u)$, where $u \sim U(\sin\delta_{min}, \sin\delta_{max})$. In other words, the declination will be uniformly distributed according to the *arcsin* of the sine of its minimum and maximum values.

The density of our random sample is determined by the requirement to have the volume of a sphere with the minimum filament radius considered in our analysis (i.e. 3 Mpc h_{70}^{-1}), probed by at least 30 random points. This leads us to a total number of ∼3 billion random points spread across the three equatorial regions. In Table 5.1 we provide the fractional volumes of both filaments and voids as a function of filament radius. We note that Alpaslan et al. (2014) used a radius of 4.13 Mpc h_{100}^{-1} to divide galaxies into filament and void galaxies in the FC.

Table 5.1: Fraction of the total survey volume occupied by filaments and voids (i.e. everything outside the filaments) as a function of the assumed filament radius.

Filament radius (h_{70}^{-1} Mpc)	Fractional volume of filaments (%)	Fractional volume of voids (%)
3	13	87
4	23	77
5	34	66
6	45	55
7	56	44

6 Environment-dependent galaxy stellar mass functions in the low-redshift Universe

In this chapter, we present and discuss our results on the environment-dependent GSMFs in the low-redshift Universe. We analyse how the GSMF varies as a function of several environmental properties, and interpret our findings in the context of previous results from the literature.

6.1 Results

In this section, we present our results on the variation of the cGSMF as a function of each environmental property described in Sect. 4: orthogonal distance to the nearest filament $D_{\perp,\mathrm{min}}$ (6.1.1), group membership (6.1.2), group halo mass M_{halo} (in particular, its dynamical estimate M_{dyn} in 6.1.3.1 and its luminosity-based one M_{lum} in 6.1.3.2) and the combination of group branch order BO and group number of connecting links N_{links} (6.1.4).

6.1.1 How the GSMF differs in filaments and voids

We now investigate the cGSMF in filaments and in voids. As discussed in Sect. 2.5.3, we use the definition of the quasi one-dimensional filaments identified in the equatorial GAMA regions by Alpaslan et al. (2014), but we do not use their classification of galaxies as belonging to filaments or voids. Instead, we prefer to implement our own classification in order to be able to investigate

Table 6.1: Best-fit double Schechter function parameters for the mass functions in voids (left) and filaments (right), when considering our entire galaxy sample.

$\log M^\star$ $(M_\odot h_{70}^{-2})$	α_1	α_2	Void sample	Filament sample	$\log M^\star$ $(M_\odot h_{70}^{-2})$	α_1	α_2
10.52 ± 0.01	-0.49 ± 0.07	-1.51 ± 0.05	$D_{\perp,\mathrm{min}} > 3$	$D_{\perp,\mathrm{min}} \leq 3$	10.82 ± 0.01	-0.83 ± 0.03	-1.75 ± 0.11
10.50 ± 0.02	-0.43 ± 0.08	-1.51 ± 0.05	$D_{\perp,\mathrm{min}} > 4$	$D_{\perp,\mathrm{min}} \leq 4$	10.81 ± 0.01	-0.86 ± 0.02	-1.77 ± 0.11
10.51 ± 0.02	-0.49 ± 0.08	-1.54 ± 0.06	$D_{\perp,\mathrm{min}} > 5$	$D_{\perp,\mathrm{min}} \leq 5$	10.80 ± 0.01	-0.85 ± 0.02	-1.75 ± 0.09
10.50 ± 0.02	-0.47 ± 0.09	-1.54 ± 0.06	$D_{\perp,\mathrm{min}} > 6$	$D_{\perp,\mathrm{min}} \leq 6$	10.79 ± 0.01	-0.86 ± 0.02	-1.75 ± 0.09
10.49 ± 0.02	-0.38 ± 0.11	-1.50 ± 0.06	$D_{\perp,\mathrm{min}} > 7$	$D_{\perp,\mathrm{min}} \leq 7$	10.78 ± 0.01	-0.87 ± 0.02	-1.78 ± 0.09

Notes. The $D_{\perp,\mathrm{min}}$ limits are given in units of Mpc h_{70}^{-1}.

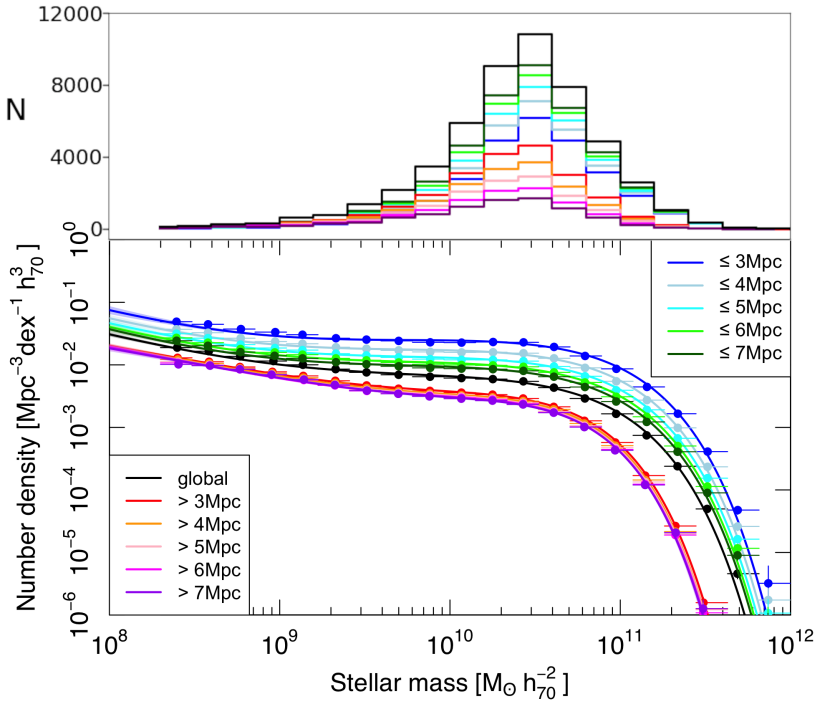

(a) All galaxies

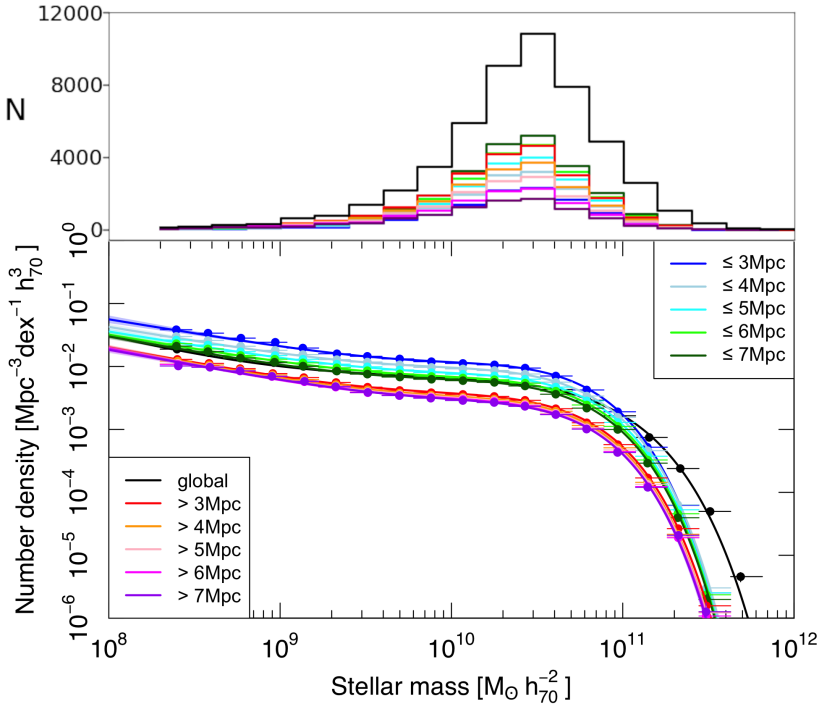

(b) Excluding grouped galaxies in filaments

Figure 6.1: Lower panels: cGSMFs in voids and filaments colour-coded by filament radius as indicated in the legend. In panel (a), we use our entire galaxy sample, while in panel (b) we discard all the grouped galaxies from our filament samples. Our global GSMF is also shown in black. Upper panels: Raw number of galaxies as a function of stellar mass in each sample, as indicated.

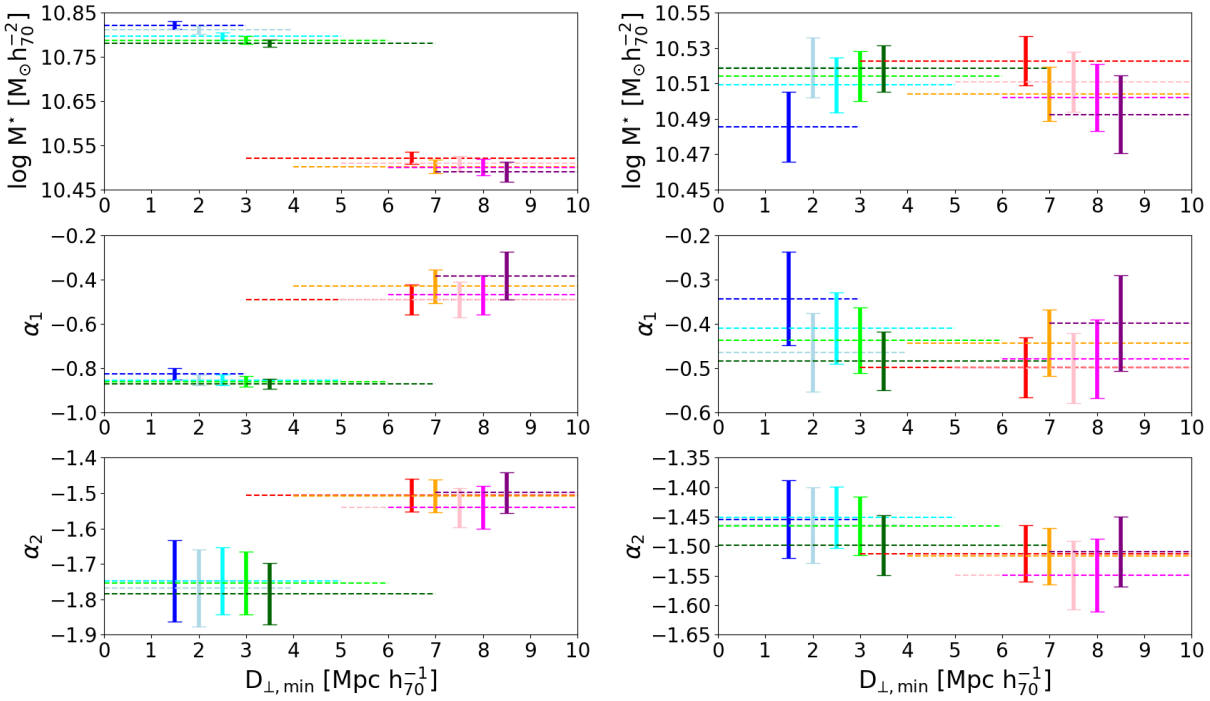

(a) All galaxies

(b) Excluding grouped galaxies in filaments

Figure 6.2: Best-fit double Schechter function parameters of the cGSMFs shown in Fig. 6.1 using the same colour-coding by filament radius. The differences between filaments and voids found for $M^\star$, α_1 and α_2 when using the entire galaxy sample in panel (a) vanish after removing all grouped galaxies from the filament samples in panel (b). We note the different scaling of the y-axes in (a) and (b).

Table 6.2: Same as Table 6.1 but now discarding all the grouped galaxies in filaments from our filament samples.

$\log M^\star$ $(M_\odot h_{70}^{-2})$	α_1	α_2	Void sample	Filament sample	$\log M^\star$ $(M_\odot h_{70}^{-2})$	α_1	α_2
10.52 ± 0.01	-0.49 ± 0.07	-1.51 ± 0.05	$D_{\perp,\mathrm{min}} > 3$	$D_{\perp,\mathrm{min}} \leq 3$	10.49 ± 0.02	-0.34 ± 0.11	-1.45 ± 0.07
10.50 ± 0.02	-0.43 ± 0.08	-1.51 ± 0.05	$D_{\perp,\mathrm{min}} > 4$	$D_{\perp,\mathrm{min}} \leq 4$	10.52 ± 0.02	-0.47 ± 0.09	-1.46 ± 0.06
10.51 ± 0.02	-0.49 ± 0.08	-1.54 ± 0.06	$D_{\perp,\mathrm{min}} > 5$	$D_{\perp,\mathrm{min}} \leq 5$	10.51 ± 0.02	-0.41 ± 0.08	-1.45 ± 0.05
10.50 ± 0.02	-0.47 ± 0.09	-1.54 ± 0.06	$D_{\perp,\mathrm{min}} > 6$	$D_{\perp,\mathrm{min}} \leq 6$	10.51 ± 0.01	-0.44 ± 0.07	-1.47 ± 0.05
10.49 ± 0.02	-0.38 ± 0.11	-1.50 ± 0.06	$D_{\perp,\mathrm{min}} > 7$	$D_{\perp,\mathrm{min}} \leq 7$	10.52 ± 0.01	-0.48 ± 0.07	-1.50 ± 0.05

the effect of assuming different filament radii. Since we do not know a priori how thick a typical filament should be, we used different filament radii, as listed in Table 5.1. Having calculated, for each galaxy in our sample, its orthogonal distance to its nearest filament, $D_{\perp,\mathrm{min}}$, we consider all galaxies with $D_{\perp,\mathrm{min}}$ smaller than the filament radius under consideration as being part of a filament, while all others are considered void galaxies.

In Fig. 6.1(a) we show the cGSMFs of void and filament galaxies as a function of the filament radius. Their best-fit double Schechter function parameters are tabulated in Table 6.1 and shown in Fig. 6.2(a). We note that in these and similar tables and figures throughout this paper, we only present our results regarding $M^\star$, α_1 and α_2, since we are more interested in any change of the shape of the mass function and less in its normalization. From Figs. 6.1(a) and 6.2(a) we see that the shape of the void GSMF is essentially unaffected by the filament radius. On the other hand, the filament GSMF does show some small variation in $M^\star$. However, by far the most striking feature of these figures is the very significant difference in the shapes of the filament and void GSMFs, which is manifested in all three of the Schechter function parameters shown.

In Fig. 6.3 we show the 1-σ, 2-σ and 3-σ likelihood contours of the cGSMFs in voids and filaments. Clearly, the differences in the double Schechter function parameters $M^\star$, α_1 and α_2 between voids and filaments, already seen in Fig. 6.2(a), remain significant when taking into account the correlations among the parameters.

So far, we have only considered the cumulative (w.r.t. to filament radius) mass functions. In Fig. 6.4 we now show the Schechter function parameters of the cGSMFs in differential bins of $D_{\perp,\mathrm{min}}$. This clearly demonstrates that the difference between the shapes of the void and filament cGSMFs is entirely driven by the innermost 0–3 Mpc h_{70}^{-1} bin. In fact, as we subsequently demonstrate, it is entirely driven by the galaxies belonging to the groups that define the filaments.

In Sect. 4.1 we defined the G1 subsample as all those grouped galaxies for which the groups are part of a filament. These galaxies were assigned $D_{\perp,\mathrm{min}} = 0$ by definition. We now discard the G1 subsample from our filament samples. The new cGSMFs as a function of the filament radius are shown in Fig. 6.1(b), and their best-fit double Schechter function parameters are tabulated in Table 6.2 and shown in Fig. 6.2(b). With the removal of the grouped galaxies from our filament samples, the differences between the shapes of the void and the filament cGSMFs have disappeared almost entirely, as shown in Fig. 6.1(b). In particular, the new filament cGSMFs now have systematically lower $M^\star$ and shallower α_1 and α_2 values, almost indistinguishable from those of the void mass functions. In other words, the galaxies in G1 contribute significantly to higher masses and steeper slopes, leading us to conclude that the shape of the GSMF is not strongly affected by the larger-scale environment (i.e. voids versus filaments), but rather by group membership.

6.1.2 How the GSMF differs for grouped and ungrouped galaxies

We now demonstrate the effect of group membership on the mass function explicitly by directly comparing the cGSMFs of grouped and ungrouped galaxies.

The volume correction for the group galaxy sample was calculated as follows. First, each group was assigned the median `Rad50` of the groups with the same number of members, where `Rad50` is the group radius defined by the 50$^{\mathrm{th}}$ percentile group member (taken from the G^{3}C). The

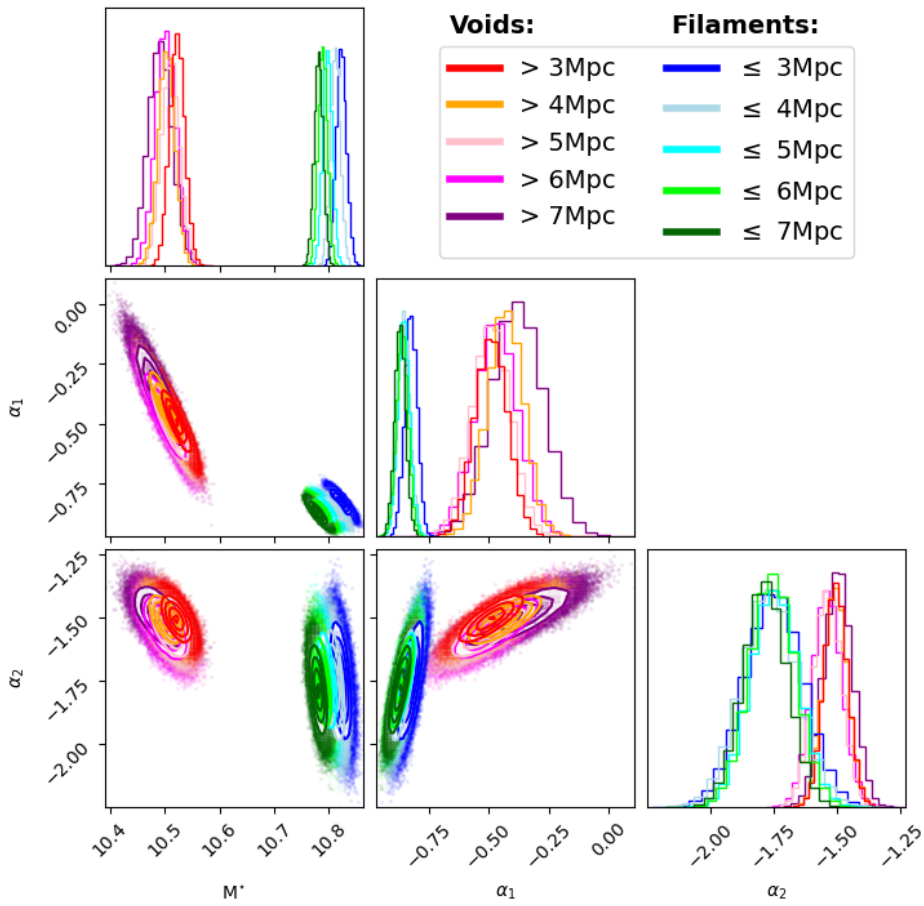

Figure 6.3: Likelihood contours at the 1-σ, 2-σ and 3-σ levels of the cGSMFs in voids and filaments colour-coded by filament radius as indicated in the legend. For each distribution, 10^5 random samples were generated.

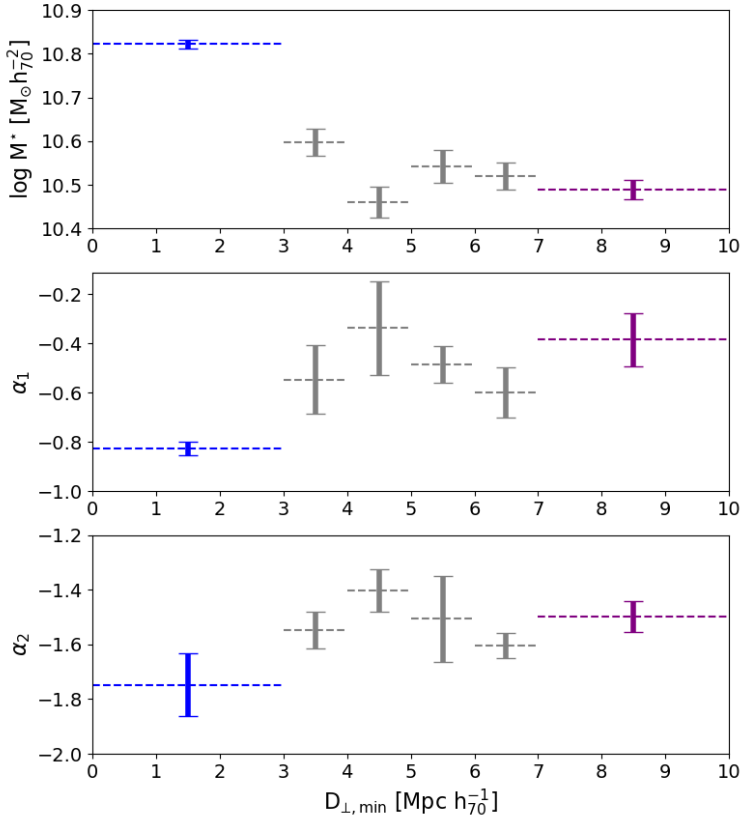

Figure 6.4: Best-fit double Schechter function parameters for the differential cGSMFs in the range 3–7 Mpc h_{70}^{-1} (shown in grey). The results for $D_{\perp,\mathrm{min}} \leq 3$ and $D_{\perp,\mathrm{min}} > 7$ are shown in blue and purple, respectively.

group's volume was then calculated assuming a spherical shape, and the final volume correction was then derived by summing up the volumes of all groups. When we divide our sample into bins of a group property, as we do in Sects. 6.1.3 and 6.1.4, each volume correction is derived by summing up the volumes of those groups with the property within that bin.

Our resulting cGSMFs are shown in Fig. 6.5, and the best-fit double Schechter function parameters are tabulated in Table 6.3 (cf. also Fig. 6.7). Clearly, the mass functions of the grouped (in yellow) and ungrouped galaxies (in brown) differ substantially: the characteristic mass $M^\star$ of the grouped cGSMF is larger, its intermediate-mass slope α_1 is steeper, while its low-mass slope α_2 is essentially the same. As we shall see in the next subsection, these differences are likely due to the ungrouped galaxies being hosted by less massive halos compared to the grouped galaxies.

Splitting the group galaxy sample into those that are part of a filament (subsample G1) and those that are not (subsample G2), we also find significant differences. In particular, the cGSMF of the grouped filament galaxies has a larger characteristic mass than that of the grouped galaxies outside of filaments. Again anticipating the results of the next subsection, we attribute

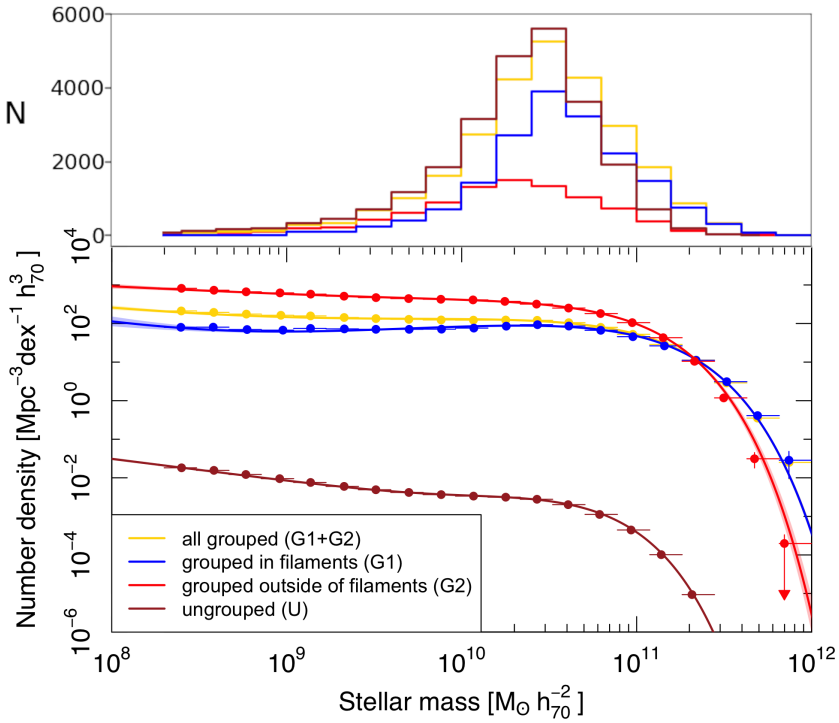

Figure 6.5: Lower panel: cGSMFs of grouped and ungrouped galaxies, as indicated in the legend. The grouped galaxies have further been subdivided into those that are part of a filament and those that are not. We note that our total group sample occupies a volume of just $\sim 2.4 \times 10^2$ Mpc^3 h_{70}^{-3}. This explains why the cGSMFs of grouped and ungrouped galaxies differ by $\sim$4 orders of magnitude. Upper panel: Raw number of galaxies as a function of stellar mass in each sample, as indicated.

Table 6.3: Best-fit double Schechter function parameters for the mass functions of grouped and ungrouped galaxies.

Galaxy sample	$\log M^\star$ $(M_\odot\, h_{70}^{-2})$	α_1	α_2
G1+G2	10.87 ± 0.01	-0.81 ± 0.04	-1.49 ± 0.13
G1	10.86 ± 0.01	-0.69 ± 0.03	-1.71 ± 0.21
G2	10.70 ± 0.04	-0.57 ± 0.25	-1.24 ± 0.11
U	10.41 ± 0.01	-0.22 ± 0.06	-1.57 ± 0.03

this difference to the larger halo masses of the filament groups compared to the groups outside of filaments, as shown in Fig. 4.3.

We also note the large difference in the normalisation of the grouped and ungrouped cGSMFs by ∼4 orders of magnitude. This is of course due to the cGSMFs effectively measuring the typical local density in groups and of ungrouped galaxies. While the raw numbers of grouped and ungrouped galaxies in our sample are actually quite similar (cf. Sect. 4.2 and upper panel of Fig. 6.5), the volumes occupied by them are vastly different, generating the large difference in density. We hasten to point out, though, that our method of determining the volume occupied by the groups is only very approximate.

Having established the group environment as an important factor in shaping the GSMF, we now turn to investigating the GSMF as a function of group properties.

6.1.3 GSMF dependence on group halo mass

In this section, we study the dependence of the GSMF on group halo mass $M_{\rm halo}$. As described in Sect. 4.3, we have two different estimates of $M_{\rm halo}$: the dynamical mass estimate $M_{\rm dyn}$ and the group r-band luminosity-based mass estimate $M_{\rm lum}$. We now describe our GSMF measurements using these two estimates in turn.

6.1.3.1 GSMF dependence on dynamical group halo mass

To study the dependence of the GSMF on dynamical group halo mass $M_{\rm dyn}$, we are forced to discard 879/10 429 (8.4%) of our groups for which the G^{3}C does not report any $M_{\rm dyn}$ values because the measured velocity dispersion of these groups is smaller than its error. These are overwhelmingly groups with $N_{\rm FOF} = 2$. Our total sample now consists of 9550 groups containing 25 567 galaxies.

Next, we bin the galaxies into four different bins in $\log[M_{\rm dyn}/(M_\odot\, h_{70}^{-1})]$ according to the mass of the group that they belong to: ≤ 12.5, 12.5–13, 13–13.5, and > 13.5 (cf. Fig. 4.3).

As explained in Sect. 4.3, the G^{3}C provides the dynamical group halo mass using two different calibration factors, which we refer to as `MassA` and `MassAfunc`, respectively.

Our resulting cGSMFs, colour-coded by $M_{\rm dyn}$, are shown in Fig. 6.6(a) for the `MassA` calibration factor and in (b) for the `MassAfunc` factor, respectively. The best-fit double Schechter function parameters are tabulated in Table 6.4 and shown in Fig. 6.7. We first point out that the characteristic mass $M^\star$ clearly increases with $M_{\rm dyn}$. In other words, more massive halos tend to host more massive galaxies, a result to be expected in a hierarchical structure formation paradigm, where larger halos form by the merging of smaller ones, accumulating more mass and forming larger central galaxies. Furthermore, the intermediate-mass slope α_1 steepens with $M_{\rm dyn}$, that is, a more rapid decline with stellar mass in the number of intermediate-mass galaxies is observed in more massive halos. In contrast, there is no evidence for any trend in the low-mass slope α_2, except possibly for an increase in the highest halo mass bin, where the cGSMF is nonetheless best represented by a single Schechter function (with $\alpha_2 = \alpha_1$). Reassuringly, these results are largely robust against the choice of calibration factor.

We also find that the results of the previous subsection are broadly consistent with these

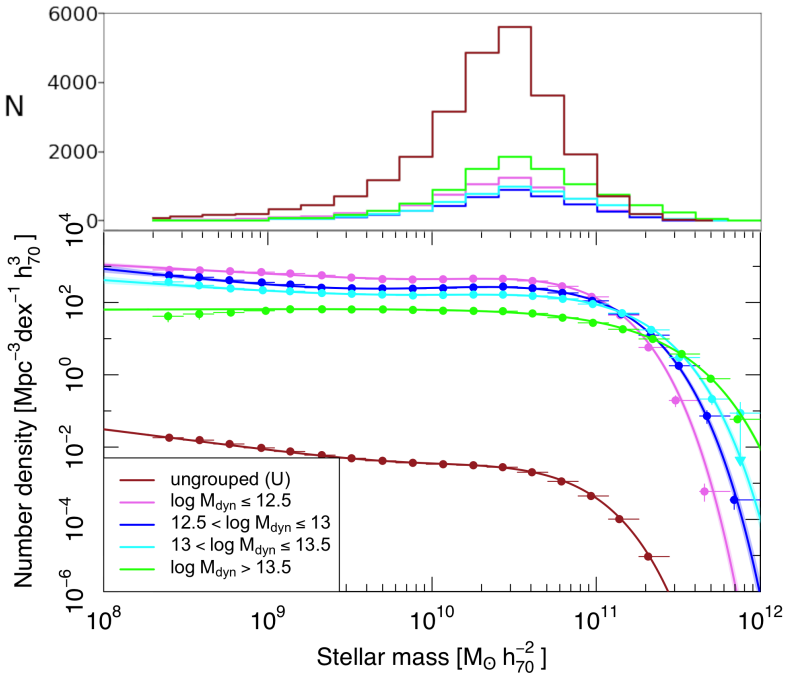

(a)

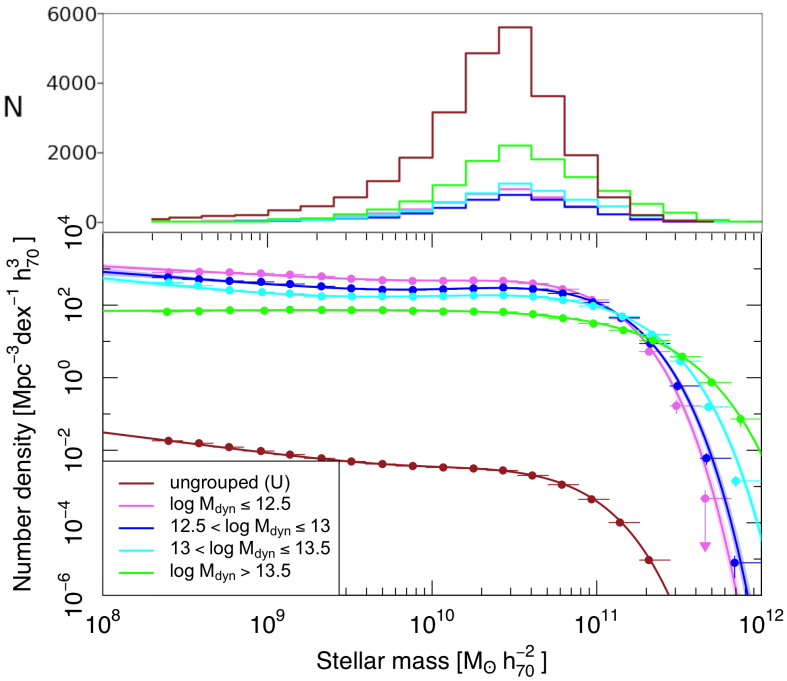

(b)

Figure 6.6: Lower panels: cGSMFs of the group galaxy subsample colour-coded by $M_{\rm dyn}$ as indicated in the legend. In panel (a), we use the `MassA` calibration factor, while in panel (b) we use the `MassAfunc` factor. For comparison, the cGSMF of the ungrouped galaxies is also shown in brown. Upper panels: Raw number of galaxies as a function of stellar mass in each sample, as indicated.

Table 6.4: Best-fit double Schechter function parameters of the cGSMFs of grouped galaxies for different subsamples, as indicated.

Galaxy sample	Halo mass estimator	$\log M^\star$ $(M_\odot\, h_{70}^{-2})$	α_1	α_2
$\log(\frac{M_{\rm dyn}}{M_\odot h_{70}^{-1}}) \leq 12.5$	`MassA`	10.47 ± 0.02	0.14 ± 0.13	-1.25 ± 0.06
$\log(\frac{M_{\rm dyn}}{M_\odot h_{70}^{-1}}) \leq 12.5$	`MassAfunc`	10.47 ± 0.03	0.12 ± 0.16	-1.24 ± 0.07
$12.5 < \log(\frac{M_{\rm dyn}}{M_\odot h_{70}^{-1}}) \leq 13$	`MassA`	10.65 ± 0.03	-0.36 ± 0.10	-1.49 ± 0.12
$12.5 < \log(\frac{M_{\rm dyn}}{M_\odot h_{70}^{-1}}) \leq 13$	`MassAfunc`	10.55 ± 0.03	-0.12 ± 0.14	-1.35 ± 0.09
$13 < \log(\frac{M_{\rm dyn}}{M_\odot h_{70}^{-1}}) \leq 13.5$	`MassA`	10.78 ± 0.03	-0.40 ± 0.14	-1.34 ± 0.12
$13 < \log(\frac{M_{\rm dyn}}{M_\odot h_{70}^{-1}}) \leq 13.5$	`MassAfunc`	10.75 ± 0.02	-0.49 ± 0.09	-1.50 ± 0.14
$\log(\frac{M_{\rm dyn}}{M_\odot h_{70}^{-1}}) > 13.5$	`MassA`	11.05 ± 0.01	-0.99 ± 0.04	-0.99 ± 0.08
$\log(\frac{M_{\rm dyn}}{M_\odot h_{70}^{-1}}) > 13.5$	`MassAfunc`	11.03 ± 0.01	-0.98 ± 0.06	-0.98 ± 0.09

trends in that the differences between the shapes of the cGSMFs of grouped galaxies in filaments and those outside of filaments can be explained almost entirely by the fact that the halo masses of groups in filaments are systematically higher than those of groups outside of filaments (cf. Fig. 4.3). The only exception is the very steep low-mass slope of the grouped galaxies in filaments (cf. Table 6.3).

To investigate whether the shape of the cGSMF of the ungrouped galaxies also fits this picture we show in Fig. 6.7 (as brown lines) the best-fit double Schechter function parameters of the ungrouped galaxies derived in the previous subsection. Of course, for these galaxies we lack an estimate of their halo masses but it seems reasonable to assume that the halo mass distribution of these galaxies will be skewed towards similar or even lower masses than that of the group halos in our lowest halo mass bin. Under this assumption, at least the $M^\star$ value of the ungrouped galaxies is entirely consistent with the $M^\star$-halo mass trend of grouped galaxies.

Overall, we thus conclude that there is clear evidence of a dependence of $M^\star$ and α_1 on halo mass, while there is no clear trend for α_2.

6.1.3.2 GSMF dependence on luminosity-based group halo mass

To study the dependence of the GSMF on luminosity-based group halo mass $M_{\rm lum}$, we follow the work of Vázquez-Mata et al. (2020) and only consider high-fidelity groups with multiplicity $N_{\rm FOF} > 4$ and $M_{\rm lum} > 10^{12}\ M_\odot\ h_{70}^{-1}$, as this is the sample for which the luminosity-halo mass scaling relation of Viola et al. (2015) is well calibrated. We are thus forced to discard 8917/10 429 (85.5%) of our groups, leaving us with 1512 groups containing 11 417 galaxies.

We now bin the remaining galaxies into three different bins in $\log[M_{\rm lum}/(M_\odot\, h_{70}^{-1})]$ according to the mass of the group that they belong to: ≤ 13.75, 13.75–14.25, and > 14.25 (cf. Fig. 4.3).

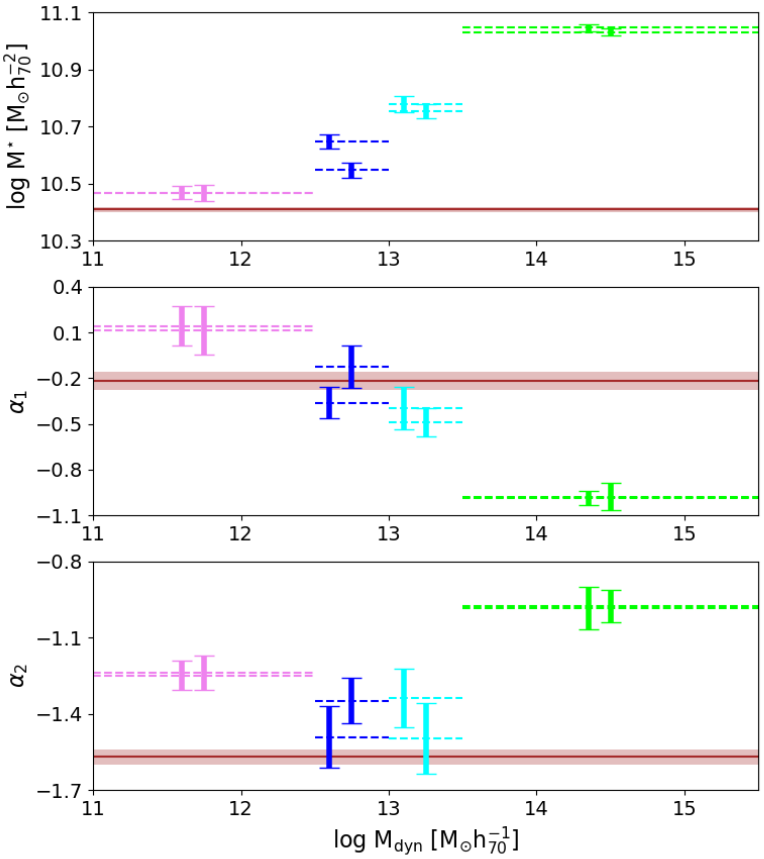

Figure 6.7: Best-fit double Schechter function parameters of the cGSMFs shown in Fig. 6.6 using the same colour-coding by $M_{\rm dyn}$. For clarity, the vertical error bars corresponding to the `MassA` estimator have been slightly offset to the left. The brown horizontal bands show the results for the ungrouped galaxy sample.

As explained in Sect. 4.3, the G^{3}C provides the total group luminosity that we use to derive the luminosity-based halo mass using two different calibration factors, which we refer to as (`LumB`) and (`LumBfunc`), respectively.

Our resulting cGSMFs, colour-coded by $M_{\rm lum}$, are shown in Fig. 6.8(a) for the `LumB` calibration factor and in (b) for the `LumBfunc` factor, respectively. For a direct comparison, panels (c) and (d) show the corresponding cGMSFs for the same mass bins using the dynamical halo mass estimator (i.e. using $M_{\rm dyn}$ for the bin assignment, and using the same $N_{\rm FOF} > 4$ selection). The best-fit double Schechter function parameters are tabulated in Table 6.5 and shown in Fig. 6.9, where the left panels show the results for $M_{\rm lum}$ and the right panels those for $M_{\rm dyn}$. We see that all four mass estimators provide results that are largely consistent with each other for all three Schechter function parameters. As in the previous subsection, we also find here that the cGSMF is best represented by a single Schechter function at $M_{\rm halo} > 10^{13.5}\ M_\odot\ h_{70}^{-1}$. However, with the cGSMFs of the intermediate and high halo mass bins being essentially identical, it is not possible

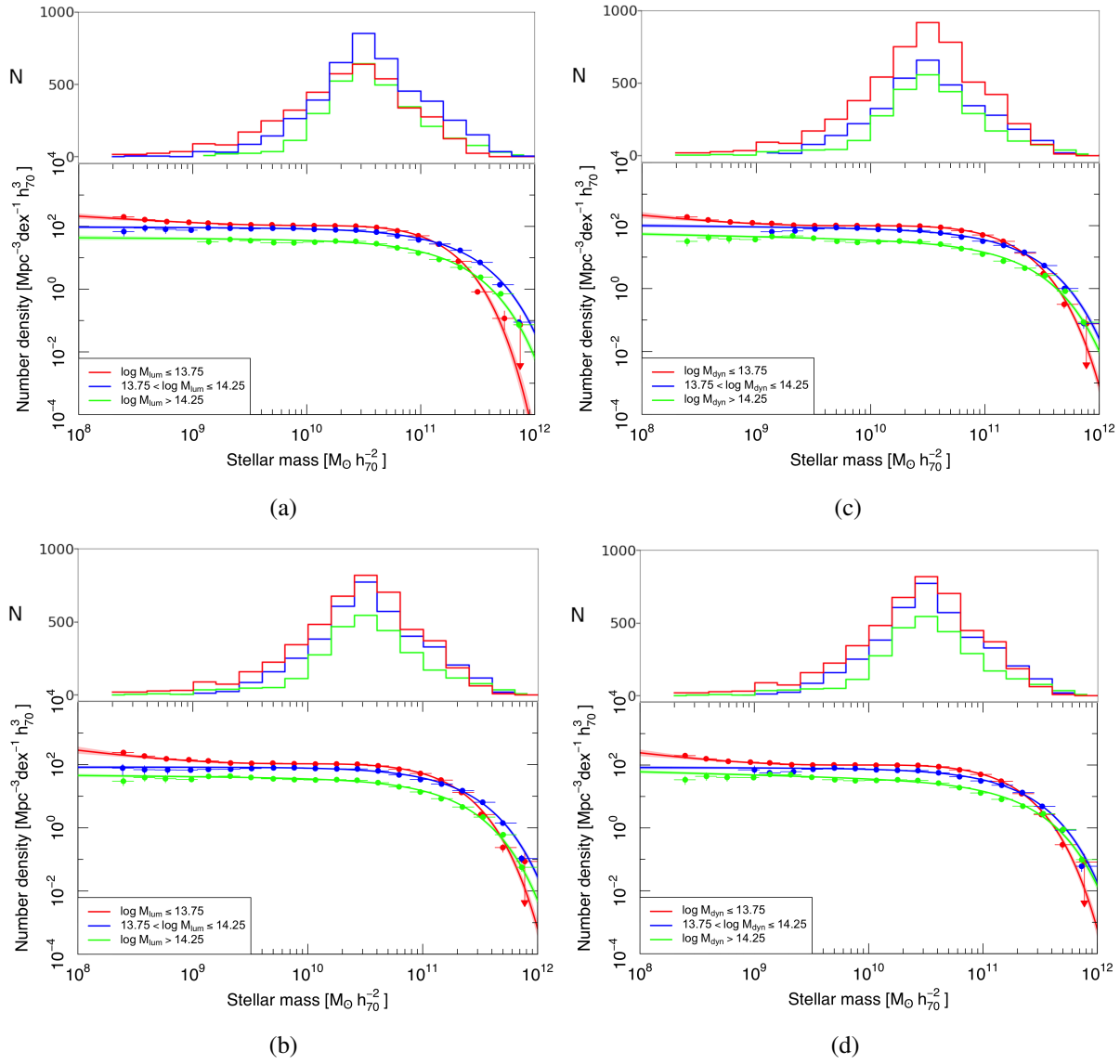

Figure 6.8: Left column, lower panels: cGSMFs of our high-fidelity group galaxy subsample colour-coded by $M_{\rm lum}$, as indicated in the legend. In panel (a) we use the `LumB` calibration factor, while in panel (b) we use the `LumBfunc` factor. Right column, lower panels: Same as the left but using the dynamical halo mass estimates with the `MassA` calibration factor in panel (c) and the `MassAfunc` factor in panel (d). Upper panels: Raw number of galaxies as a function of stellar mass in each sample, as indicated.

Table 6.5: Best-fit double Schechter function parameters of the cGSMFs of grouped galaxies for different subsamples, as indicated.

Galaxy sample $N_{\rm FOF} > 4$	Halo mass estimator	$\log M^\star$ $(M_\odot\, h_{70}^{-2})$	α_1	α_2
$\log(\frac{M_{\rm lum}}{M_\odot h_{70}^{-1}}) \leq 13.75$	LumB	10.74 ± 0.04	-0.33 ± 0.22	-1.23 ± 0.11
$\log(\frac{M_{\rm dyn}}{M_\odot h_{70}^{-1}}) \leq 13.75$	MassA	10.88 ± 0.03	-0.67 ± 0.12	-1.40 ± 0.18
$\log(\frac{M_{\rm lum}}{M_\odot h_{70}^{-1}}) \leq 13.75$	LumBfunc	10.88 ± 0.03	-0.70 ± 0.12	-1.48 ± 0.20
$\log(\frac{M_{\rm dyn}}{M_\odot h_{70}^{-1}}) \leq 13.75$	MassAfunc	10.87 ± 0.03	-0.69 ± 0.11	-1.47 ± 0.19
$13.75 < \log(\frac{M_{\rm dyn}}{M_\odot h_{70}^{-1}}) \leq 14.25$	LumB	11.12 ± 0.02	-1.01 ± 0.07	-1.01 ± 0.10
$13.75 < \log(\frac{M_{\rm dyn}}{M_\odot h_{70}^{-1}}) \leq 14.25$	MassA	11.10 ± 0.02	-1.04 ± 0.17	-1.04 ± 0.06
$13.75 < \log(\frac{M_{\rm dyn}}{M_\odot h_{70}^{-1}}) \leq 14.25$	LumBfunc	11.10 ± 0.02	-1.00 ± 0.02	-1.00 ± 0.04
$13.75 < \log(\frac{M_{\rm dyn}}{M_\odot h_{70}^{-1}}) \leq 14.25$	MassAfunc	11.08 ± 0.02	-1.01 ± 0.18	-1.01 ± 0.06
$\log(\frac{M_{\rm dyn}}{M_\odot h_{70}^{-1}} >) 14.25$	LumB	11.07 ± 0.03	-1.02 ± 0.09	-1.02 ± 0.08
$\log(\frac{M_{\rm dyn}}{M_\odot h_{70}^{-1}} >) 14.25$	MassA	11.11 ± 0.02	-1.08 ± 0.07	-1.08 ± 0.06
$\log(\frac{M_{\rm dyn}}{M_\odot h_{70}^{-1}} >) 14.25$	LumBfunc	11.06 ± 0.02	-1.04 ± 0.13	-1.04 ± 0.05
$\log(\frac{M_{\rm dyn}}{M_\odot h_{70}^{-1}} >) 14.25$	MassAfunc	11.13 ± 0.02	-1.10 ± 0.02	-1.10 ± 0.05

to confidently confirm the trends with halo mass observed in the previous subsection with this more limited (albeit higher fidelity) sample. On the other hand, the results are not inconsistent with these trends either.

6.1.4 GSMF dependence on group branch order and number of connecting links

In Sect. 6.1.1 we analysed the change (or lack thereof) of the mass function when moving perpendicularly to the filaments. We now investigate the dependence of the GSMF on the position within the filamentary structure.

From our groups-in-filaments galaxy subsample (G1) defined in Sect. 4.1, we select six different subsamples according to specific combinations of group branch order BO and group number of connecting links $N_{\rm links}$, as listed in Table 6.6. In particular, we distinguish between galaxies in groups located in their filaments' backbone (BO = 1) and in their outskirts (BO > 1), as well as between galaxies inhabiting groups located at the edge ($N_{\rm links} = 1$), at an intermediate position ($N_{\rm links} = 2$), and at the centre ($N_{\rm links} > 2$) of their filament. We note that the full range of both parameters is 1–5.

The resulting cGSMFs are shown in Fig. 6.10 as a function of the combination of BO and $N_{\rm links}$. The best-fit double Schechter function parameters are tabulated in Table 6.7 and shown in Fig. 6.11. We first note that, when moving from the backbone (in red) to the outskirts (in blue),

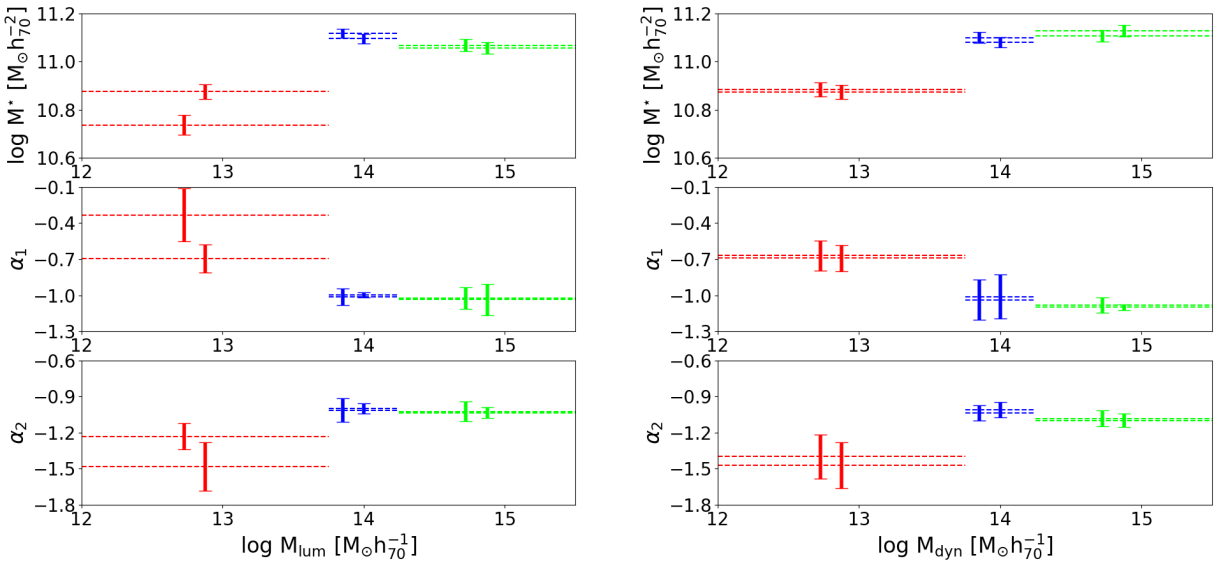

Figure 6.9: Best-fit double Schechter function parameters of the cGSMFs shown in Fig. 6.8 using the same colour-coding by $M_{\rm lum}$ (left) or $M_{\rm dyn}$ (right). For clarity, the vertical error bars corresponding to the `LumB` (left) and `MassA` (right) estimators have been slightly offset to the left.

Table 6.6: Selection of $2 \times 3 = 6$ different subsamples from the FC group galaxy sample (G1) based on the group branch order (BO) and number of connecting links ($N_{\rm links}$).

	Backbone	Outskirts
edge	BO = 1 & $N_{\rm links} = 1$	BO > 1 & $N_{\rm links} = 1$
intermediate	BO = 1 & $N_{\rm links} = 2$	BO > 1 & $N_{\rm links} = 2$
centre	BO = 1 & $N_{\rm links} > 2$	BO > 1 & $N_{\rm links} > 2$

none of the three double Schechter parameters seem to vary very significantly, regardless of the value of $N_{\rm links}$. Both for centres and edges, the backbone and outskirts are in excellent agreement in all three Schechter parameters, while for the intermediate regions some mildly significant differences appear, with higher $M^\star$ and α_2 values and a lower α_1 value in the outskirts compared to the backbone. However, this may be affected by the fact that the cGSMF of the intermediate regions in outskirts are best fit with a single Schechter function (where $\alpha_1 = \alpha_2$), which also applies to the central regions of both the backbone and the outskirts (cf. Table 6.7).

Table 6.7: Best-fit double Schechter function parameters for the mass functions of grouped galaxies in filaments for different subsamples and for grouped galaxies outside of filaments, as indicated.

Galaxy sample	$\log M^\star$ $(M_\odot\, h_{70}^{-2})$	α_1	α_2
BO = 1 & $N_{\rm links} > 2$ (backbone centres)	10.84 ± 0.02	-0.62 ± 0.08	-0.62 ± 0.34
BO > 1 & $N_{\rm links} > 2$ (outskirts centres)	10.82 ± 0.03	-0.57 ± 0.13	-0.57 ± 0.30
BO = 1 & $N_{\rm links} = 2$ (backbone intermediates)	10.87 ± 0.02	-0.71 ± 0.04	-1.82 ± 0.38
BO > 1 & $N_{\rm links} = 2$ (outskirts intermediates)	10.96 ± 0.03	-0.85 ± 0.05	-0.85 ± 0.27
BO = 1 & $N_{\rm links} = 1$ (backbone edges)	10.80 ± 0.03	-0.57 ± 0.10	-1.36 ± 0.21
BO > 1 & $N_{\rm links} = 1$ (outskirts edges)	10.79 ± 0.03	-0.55 ± 0.09	-1.79 ± 0.66
Grouped galaxies outside of filaments (G2)	10.70 ± 0.04	-0.57 ± 0.25	-1.24 ± 0.11

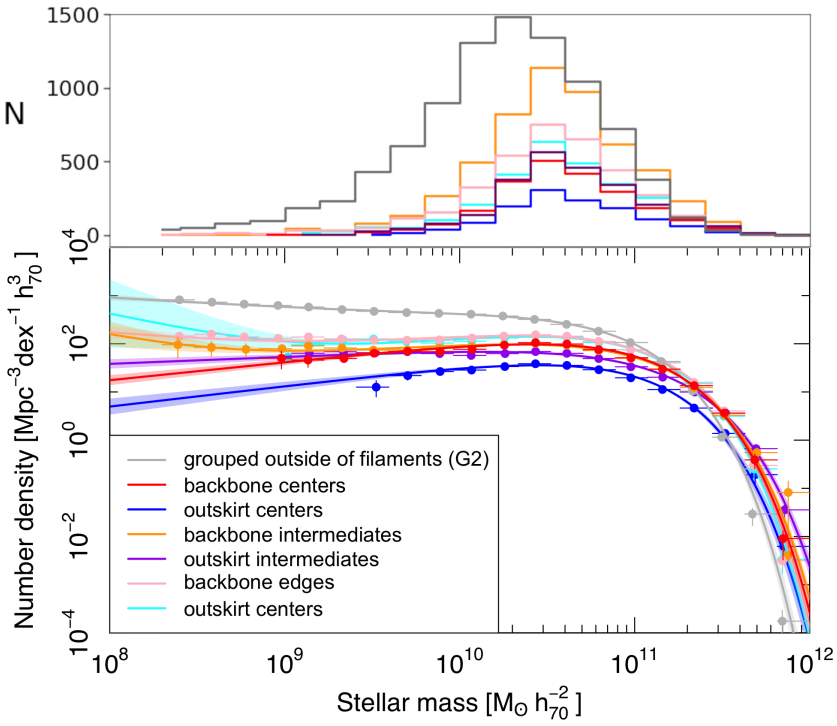

Figure 6.10: Lower panel: cGSMFs of grouped galaxies in filaments (G1 subsample) colour-coded by a combination of BO and $N_{\rm links}$, as indicated in the legend. For comparison, the cGSMF of grouped galaxies outside of filaments (G2) is also shown in grey. Upper panel: Raw number of galaxies as a function of stellar mass in each sample, as indicated.

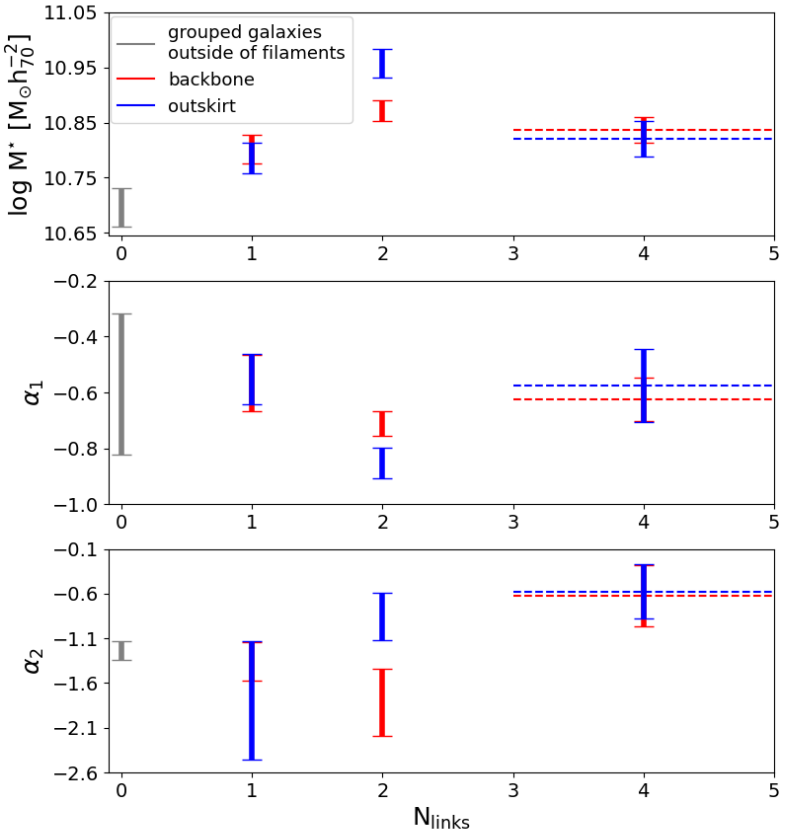

Figure 6.11: Best-fit double Schechter function parameters of the cGSMFs shown in Fig. 6.10, as indicated in the legend. The grouped galaxies outside of filaments (in grey) are somewhat arbitrarily shown at $N_{\rm links} = 0$.

In addition, we did not find any significant trends as function of $N_{\rm links}$ for any of the Schechter function parameters for the backbone or the outskirts sample, or their combination. This remains true if we add, somewhat arbitrarily, the Schechter function parameters of grouped galaxies outside of filaments at $N_{\rm links} = 0$ (shown in grey in Fig. 6.11). All we observed here is that the $M^\star$ value of grouped galaxies outside of filaments is significantly lower than that of grouped galaxies in filaments, as we had already noted in Sect. 6.1.2.

We thus conclude that there is no evidence for any differences in the shape of the GSMF of grouped galaxies in filaments as a function of position within the filamentary structure.

6.2 Discussion

In this section, we first compare our global GSMF with other GAMA and SDSS DR7 GSMFs (6.2.1), and then discuss our results on the dependence of the mass function on different environmental measures in the context of other similar studies (6.2.2).

6.2.1 Global GAMA and SDSS DR7 GSMFs

Many studies have already been undertaken inside the GAMA project concerning GSMFs. Baldry et al. (2012) selected a flux-limited sample of 5210 galaxies from the earliest phase of the GAMA project, called GAMA I, covering an area of 143 deg^2. This sample was complete to $r = 19.4$ mag in the G09 and G15 regions and to $r = 19.8$ mag in G12, and covered the redshift range $0.002 < z < 0.06$. Kelvin et al. (2014) selected a local volume-limited subsample of 2711 galaxies, also from GAMA I, to a lower stellar mass limit of $M = 10^9\ M_\odot$, covering $0.025 < z < 0.06$. Similarly, Alpaslan et al. (2015) defined a local volume-limited subsample of 7195 galaxies to a lower stellar mass limit of $M = 10^{9.5}\ M_\odot$, up to $z = 0.1$. Wright et al. (2017) expanded the analysis by Baldry et al. (2012) to the full GAMA II dataset. Their flux-limited sample, covering the same GAMA II equatorial regions of 180 deg^2 used in this study, was complete down to $r = 19.8$ mag and covered the redshift range $0.002 < z < 0.1$. Baldry et al. (2012), Kelvin et al. (2014) and Wright et al. (2017) all computed their global GSMFs using a density-corrected $1/V_{\rm max}$ method. Completing the set of GSMF studied with GAMA, Driver et al. (2022) most recently considered a flux-limited sample of 13 957 galaxies from the latest version of GAMA, called GAMA III, adding the G23 region to the equatorial regions for a total area of 250 deg^2. The magnitude limit of this sample was $r = 19.65$ mag, covering a redshift range of $0.0013 < z < 0.1$. They computed their GSMF using the same MML estimator as in the present study. Finally, we include in our comparison the GSMF of Weigel et al. (2016), which was measured from a sample of ~110 000 galaxies selected from the SDSS DR7, covering an area of 7748 deg^2, with a magnitude limit of $r = 17.77$ mag and a redshift range of $0.02 < z < 0.06$. Their GSMF was computed using the parametric maximum likelihood method, originally developed by Sandage et al. (1979).

The global GSMF was fit with a double Schechter function in almost all of theses studies. The only exception is Alpaslan et al. (2015) who used a single Schechter function. We list the best-fit Schechter parameters in Table 6.8 and compare the corresponding functions to our data and best-fit double Schechter function in Fig. 6.12. Evidently, our global GSMF, shown in black, is in very good agreement with all of the mass functions of the previous studies described above, except that of Alpaslan et al. (2015). The agreement is best with the GSMF of Driver et al. (2022), with the differences being less than a factor of two over the entire range of four orders of magnitude in stellar mass considered here (cf. lower panel of Fig. 6.12). The overall excellent agreement between these various mass functions is quite remarkable, given the differences in photometry, stellar mass estimation techniques, and GSMF measurement procedures.

Nevertheless, some differences remain. At high stellar masses, the lower $M^\star$ values of the GAMA I studies by (Baldry et al. 2012) and Kelvin et al. (2014) are likely due to the over-fragmentation of bright galaxies relative to fainter and smaller systems in the original GAMA aperture photometry, causing their fluxes to be underestimated and thus leading to an underestimate

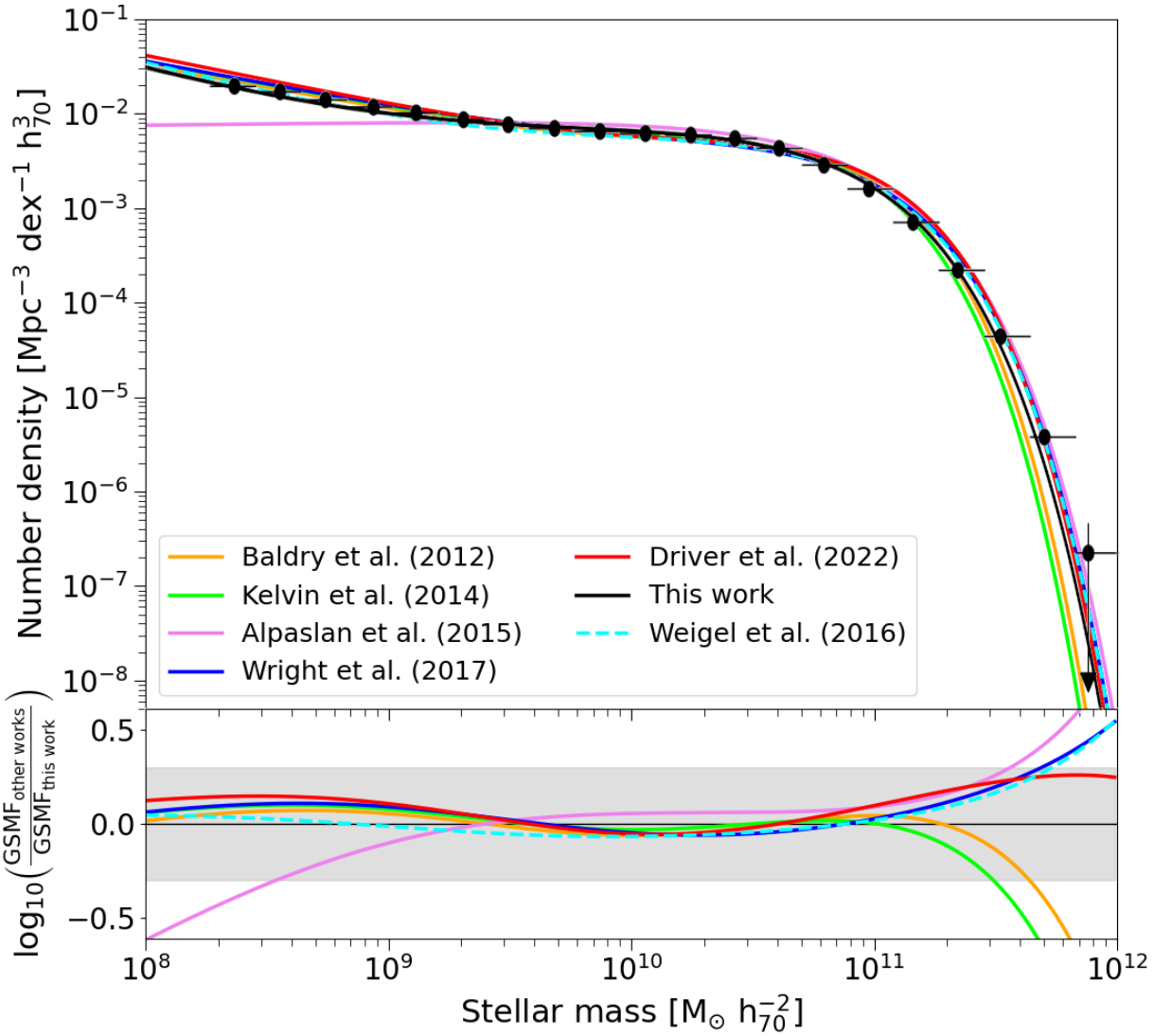

Figure 6.12: Upper panel: Comparison of our global GSMF with other recent measurements derived from GAMA and SDSS data, as indicated. Lower panel: Logarithmic ratio of the literature GSMFs relative to ours. The grey shaded area indicates agreement within a factor of two.

of their stellar masses as well. This issue was addressed in the photometry presented by Wright et al. (2017), which we have also used in this work. We note that our $M^\star$ value compares well with that of Driver et al. (2022) despite their use of further improved photometry and the improved stellar mass estimation technique of Robotham et al. (2020). At intermediate masses, where the inter-GSMF agreement is best, our global GSMF confirms a plateau from $\sim 10^{9.5}$ to $\sim 10^{10.5}$ $M_\odot\, h_{70}^{-2}$, which was already noticed by Baldry et al. (2012) in the GAMA I data. This characteristic seems to emerge at lower redshifts ($z < 1$) and may be caused by mergers (Robotham et al. 2014). Moving towards lower masses, the GSMF rises noticeably, clearly requiring a double Schechter function for an adequate description, as demonstrated by the disagreement with the single Schechter

Table 6.8: Best-fit double Schechter function parameters of the GSMFs shown in Fig. 6.12, as indicated.

Dataset	$\log M^\star$ $(M_\odot\, h_{70}^{-2})$	$\Phi_1^\star$ $(10^{-3}\ \mathrm{Mpc}^{-3}\, h_{70}^3)$	α_1	$\Phi_2^\star$ $(10^{-3}\ \mathrm{Mpc}^{-3}\, h_{70}^3)$	α_2
Baldry et al. (2012)	10.66 ± 0.05	3.96 ± 0.34	-0.35 ± 0.18	0.79 ± 0.23	-1.47 ± 0.05
Kelvin et al. (2014)	10.64 ± 0.07	4.18 ± 1.52	-0.43 ± 0.35	0.74 ± 1.13	-1.50 ± 0.22
Alpaslan et al. (2015)	10.82 ± 0.02	2.00 ± 0.13	-0.97 ± 0.02	2.00 ± 0.13	-0.97 ± 0.02
Wright et al. (2017)	10.78 ± 0.01	2.93 ± 0.40	-0.62 ± 0.03	0.63 ± 0.10	-1.50 ± 0.01
Driver et al. (2022)	10.75 ± 0.02	3.66 ± 0.14	-0.47 ± 0.07	0.63 ± 0.09	-1.53 ± 0.03
This work	10.76 ± 0.01	3.75 ± 0.09	-0.86 ± 0.03	0.13 ± 0.05	-1.71 ± 0.06
Weigel et al. (2016)	10.79 ± 0.01	9.77 ± 6.30	-0.79 ± 0.04	0.49 ± 0.23	-1.69 ± 0.10

Notes. We show our global GSMF, other GAMA GSMFs (Baldry et al. 2012; Kelvin et al. 2014; Alpaslan et al. 2015; Wright et al. 2017; Driver et al. 2022) and the SDSS DR7 GSMF derived by Weigel et al. (2016). The GSMF of Alpaslan et al. (2015) was fit with a single Schechter function, which we represent as $\Phi_1^\star = \Phi_2^\star = \Phi^\star/2$ and $\alpha_1 = \alpha_2 = \alpha$ here. Furthermore, in contrast to all other studies listed here, Alpaslan et al. (2015) used cosmological parameters of $(H_0, \Omega_\mathrm{M}, \Omega_\Lambda) = (100, 0.25, 0.75)$. We have thus rescaled their values to $H_0 = 70$ km s^{-1} Mpc^{-1}.

function GSMF of Alpaslan et al. (2015) at low masses. Despite the good agreement of the various double Schechter functions in Fig. 6.12 in the intermediate and low-mass regimes, their parameters in this regime $(\Phi_1^\star, \alpha_1, \Phi_2^\star, \alpha_2)$ are actually somewhat different. For example, our α_1 and α_2 values are significantly steeper than those of Wright et al. (2017) and Driver et al. (2022) (but very similar to those of Weigel et al. 2016), whereas our $\Phi_2^\star$ value is significantly lower. Apart from correlations among these parameters and different lower mass limits used, another reason for this variance is presumably the inability even of a double Schechter function to accurately model the intermediate-mass, low-mass, and transition regimes simultaneously.

6.2.2 Environment-dependent GSMFs

As soon as the environment is a concern in describing any change in the shape of the mass function, it is important to stress that many definitions of environment are found in the literature (e.g. Muldrew et al. 2012). One approach relies on geometry, according to which galaxies are classified into categories such as voids (i.e. three-dimensional structures), sheets (two-dimensional), filaments (one-dimensional) and clusters, groups or knots (zero-dimensional). A second approach considers the distinction between grouped and ungrouped galaxies, where the latter are often referred to as field galaxies. A third approach classifies galaxies based on halo mass. A fourth approach describes the environment through measurements of the local density (averaged over some scale), which can be parametrized in several ways and following different techniques, for example by counting the number of neighbours of a galaxy within a specific aperture or measuring the distance to the n^{th} nearest neighbour. Although these different measures of environment are generally correlated, they cannot be considered equivalent.

Exploiting the capabilities of two surveys in the redshift range $0.03 \leq z \leq 0.11$, Vulcani et al. (2012) investigated the dependence of the low-z GSMF on density, using a 5^{th} nearest neighbour approach. They found that density regulates the shape of the mass function at any mass above their mass limit, claiming that lower density regions host relatively a larger population of low-mass galaxies than higher density regions. However, when examining clusters in particular, using a 10^{th} nearest neighbour approach, the situation was found to be slightly different: in the highest density regions, the slope of the GSMF flattens out only at very low masses, suggestive of a sort of deficit of low-mass galaxies with respect to intermediate-mass ones compared to lower density regions. Moreover, they found that density determines not only the shape of the mass function, but also the highest mass encountered: the highest density regions host the most massive galaxies, which seem to be absent in the lowest density regions. Using the same surveys, Calvi et al. (2013) studied the dependence of the GSMF as a function of halo mass, finding that the mass functions of galaxies inside and outside clusters look indistinguishable. When comparing grouped, binary and ungrouped galaxies, they found that the GSMF of single galaxies was relatively richer in low-mass galaxies (i.e. showed a steeper slope) than any other subsample.

In another complementary study, making use of two surveys at intermediate redshifts in the range $0.3 \leq z \leq 0.8$, Vulcani et al. (2013) also analysed the dependence of the GSMF as a function of halo mass, identifying clusters, groups and ungrouped galaxies lying in the field. Except for the brightest cluster galaxies, they found that the GSMF is invariant, i.e. shows comparable values for $M^\star$ and α, from clusters to the field. Comparing the virialised regions of clusters and their outskirts, they also failed to detect any difference. In their view, this result confirmed that halo mass does not alter the shape of the mass distribution from clusters to ungrouped galaxies, since the outskirts of clusters can be considered as transition regions between the cluster virialised regions and the field. Their conclusions are quite surprising, considering that galaxies in halos with different masses are subject to different physical processes which can suppress SF, resulting in different mass growth rates and timescales. Nevertheless, at the redshifts considered, Vulcani et al. (2013) showed that most of the galaxy mass appears to have already been assembled, and that environment-dependent processes have had no significant influence on galaxy mass.

Guglielmo et al. (2018) also investigated the dependence of the GSMF on halo mass, identifying from the XXL survey a magnitude-complete groups and clusters (G&C) galaxy sample with redshifts $z \leq 0.6$, spanning a wide range of X-ray luminosities. Similarly to the results described above, they found no significant overall difference in the shape of the GSMF between galaxies belonging to the G&C sample and those that do not, also when binning in X-ray luminosity.

In a more recent work, O'Kane et al. (2024) investigated the dependence of the GSMF on large-scale environment using a mass-complete sample from the SDSS DR8 Main Galaxy Sample. When matching in local density, using a 3^{rd} nearest neighbour approach, as well as in stellar mass, they found that the differences observed as a function of the position in the cosmic web vanish, concluding that local density can fully explain the environmental effect of filaments.

Our results are inconsistent with the conclusions drawn by Vulcani et al. (2013), Calvi et al. (2013) and Guglielmo et al. (2018). In Sect. 6.1.3 we showed that the GSMF is clearly shaped by halo mass, since $M^\star$ clearly increases, and α_1 decreases with M_{halo}. The only result in agreement with ours is the steep value of α_2 observed by Calvi et al. (2013) in their ungrouped galaxy sample,

similar to ours (cf. Table 6.3). It is important to note here that Calvi et al. (2013) and Vulcani et al. (2013) find an excess of galaxies at $\log[M/(M_\odot\, h_{70}^{-2})] > 11.7$ in both cluster and group mass functions, with the Schechter function not able to adequately describe this behaviour.

On the other hand, the results from Vulcani et al. (2012) and O'Kane et al. (2024) seem to be compatible with ours, despite their use of a different definition of environment. Besides our findings regarding $M^\star$, as previously discussed, in Sects. 6.1.3 and 6.1.4 we also showed that at the highest halo masses, i.e. at $\log[M_{\rm halo}/(M_\odot\, h_{70}^{-1})] \gtrsim 13.5$, the GSMF is best described by a single Schechter function, in which $\alpha_1 = \alpha_2$. In other words, at these halo masses, the physical processes affecting galaxy formation and evolution seem to have a similar impact at low and intermediate masses. Moreover, we confirm that the most massive halos host the most massive galaxies.

Our clearest result is the evolution of $M^\star$, going from ungrouped to group environments (Sect. 6.1.2) as well as inside the groups as a function of halo mass (Sect. 6.1.3). We refer the reader to Robotham et al. (2006) and Robotham et al. (2010b) for consistent results on the variation of the luminosity function with group halo mass. The same behaviour was already observed by Baldry et al. (2006). Starting from a $z < 0.1$ SDSS sample and averaging between a $4^{\rm th}$ and a $5^{\rm th}$ nearest neighbour approach, they investigated the dependence of the low-z GSMF on projected density. They found that $M^\star$ varied from $10^{10.6}$ to $10^{11}\ M_\odot\, h_{70}^{-2}$ with increasing environmental density, with the fractional contribution of galaxies with $\log[M^\star/(M_\odot\, h_{70}^{-2})] \approx 11.5$ increasing by a factor of ~50. On the other hand, α did not vary strongly with environment, even if they claim that a standard Schechter function does not fit their entire mass range. When fitting with a double Schechter function with fixed $\alpha_2 = -1.5$, they found an overall steepening of α_1. This last result is also compatible with our findings: in Sect. 6.1.3 we also showed that α_1 steepens with increasing $M_{\rm halo}$.

7 Deconstructing the galaxy stellar mass function by star formation and environment

In this chapter, we present and discuss our results on deconstructing the GSMF by SF and environment. We analyse how the GSMF varies across star-forming and passive galaxies, centrals and satellites, and as a function of group halo mass. Finally, we compare our findings with previous studies to interpret them in the context of galaxy formation and evolution.

7.1 Results

In this section, we present our results on the variation of the GSMF as a function of the subsamples defined in Chapter 4: star-forming and passive galaxies (Sect. 7.1.1), and centrals and satellites (Sect. 7.1.2). Furthermore, we study the dependence of the GSMF on group halo mass $M_{\rm halo}$ (Sect. 7.1.3).

7.1.1 How the GSMF differs in star-forming and passive galaxies

We now investigate the GSMF in star-forming and passive galaxies. As discussed in Sect. 4.5, we implement a modified version of the method by Davies et al. (2019b) to separate the two populations in the $\log M$ – log SFR plane, using an iterative procedure that updates the linear regression fits and dividing line at each step until convergence. This approach removes any dependence on an arbitrary initial sSFR threshold.

In Fig. 7.1 we show the GSMFs for both our star-forming and passive galaxy populations, first using our full parent sample and then considering only galaxies inside and outside of groups (panels (a), (b) and (c), respectively). In panel (a), we also display the two Schechter components of each mass function as dashed lines. For the star-forming population, we note that the transition between the two components occurs at relatively high stellar masses compared to both the passive and global populations. In other words, in the mass range where the two Schechter components of the star-forming subsample intersect, both the passive and the total GSMFs are entirely dominated by the intermediate-mass component. As a result, the shape of the star-forming GSMF from low to intermediate masses is effectively governed by the low-mass component, while the intermediate-mass component primarily accounts for the exponential cut-off at the high-mass end. This behaviour makes the star-forming GSMF resemble a single Schechter function, which explains why previous works have typically found that a single component is a good description for such

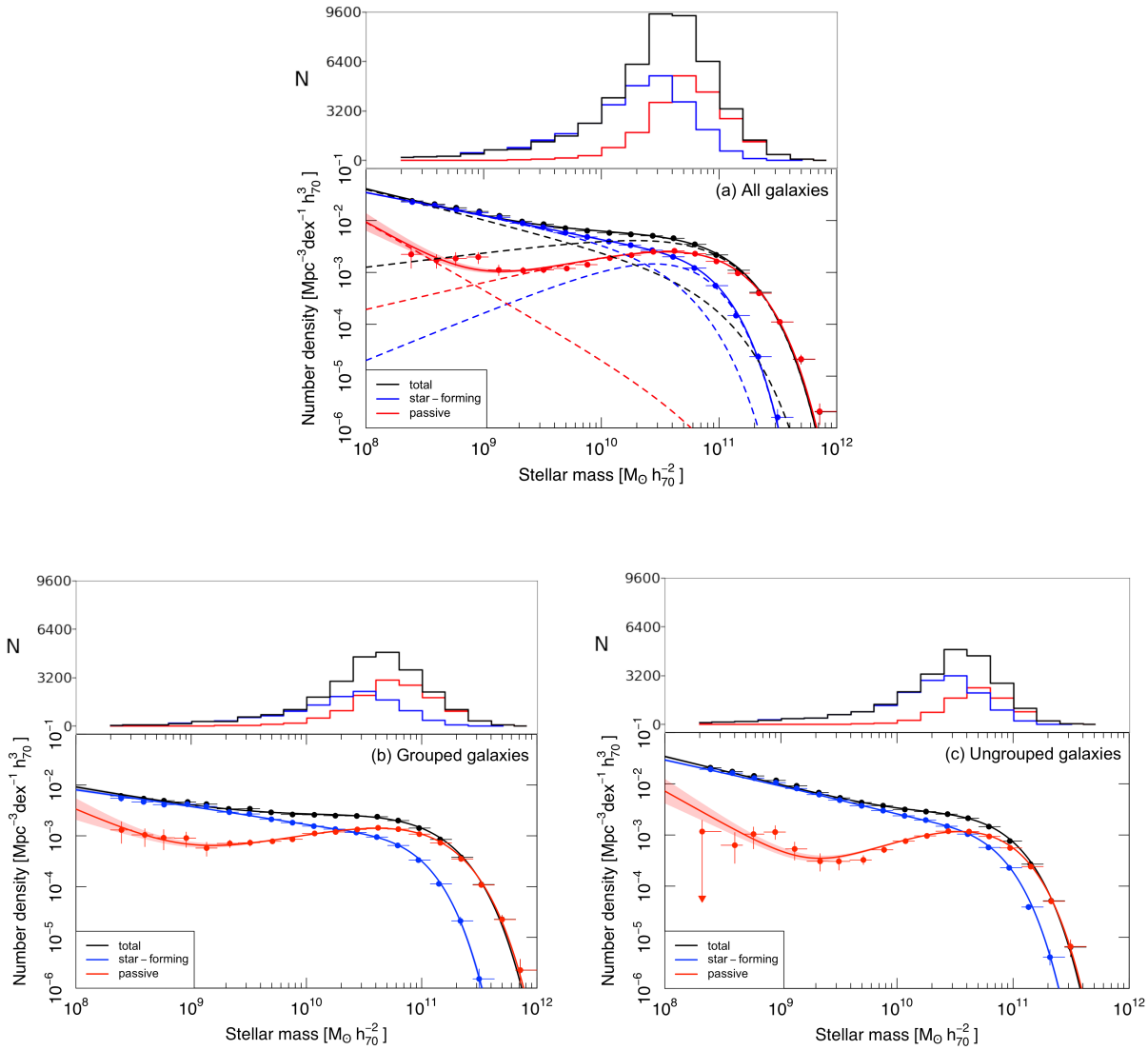

Figure 7.1: GSMFs for our total, star-forming and passive galaxy populations, as indicated in the legend. Panel (a) shows the full sample, whereas panels (b) and (c) show grouped and ungrouped galaxies, respectively. In each sub-figure, the lower panel shows the GSMFs, and the upper panel displays the raw number of galaxies as a function of stellar mass in each sample, as indicated. Dashed lines in panel (a) show the two individual Schechter components of each GSMF.

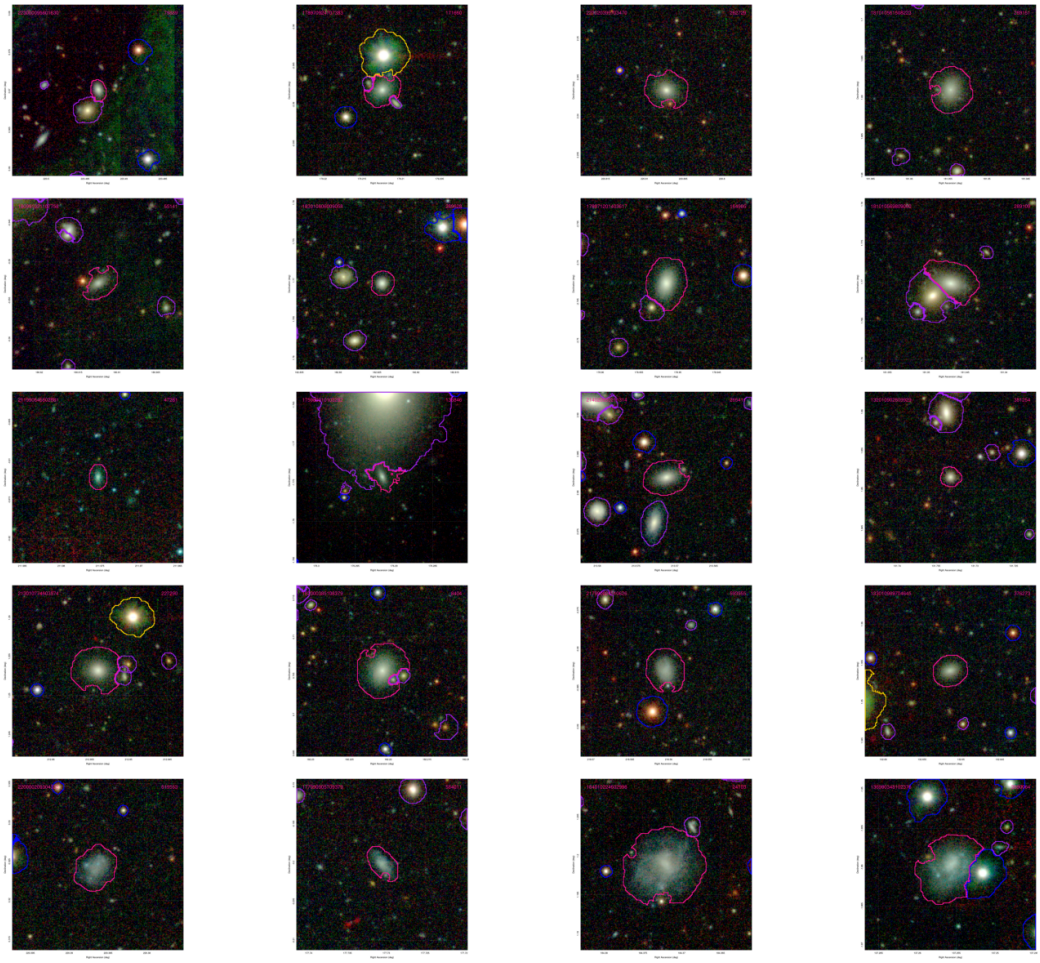

Figure 7.2: Images of the 20 randomly selected galaxies with $M_\star < 10^9 M_\odot$ visually inspected in this work. Corner IDs are shown in pink. Each image is $80'' \times 80''$, with an upper surface-brightness limit of 20 mag arcsec^{-2}. The overplotted segments highlight the target galaxy (pink), stars (blue), other galaxies (purple), and masked regions (yellow). The background is a composite *grz* colour image. Several objects, particularly those in the last row, display clear morphological signs of ongoing SF, despite being classified as passive in our analysis.

samples. Still, we find that the inclusion of a second component yields a slightly more accurate description, based on commonly used model selection criteria (see Sect. 7.2.1 for a more detailed discussion of this issue).

In contrast, for the passive galaxy population, we confirm the need for a double Schechter function, as we clearly observe a low-mass upturn consistent with several previous findings (Peng et al. 2010; Baldry et al. 2012; Weigel et al. 2016), although some other studies do not report this upturn (e.g. Taylor et al. 2015; Moffett et al. 2016b). This may be due in part to the method used to distinguish between star-forming and passive galaxies. The question thus arises whether the observed upturn may be due to an increased classification uncertainty towards the low-mass end.

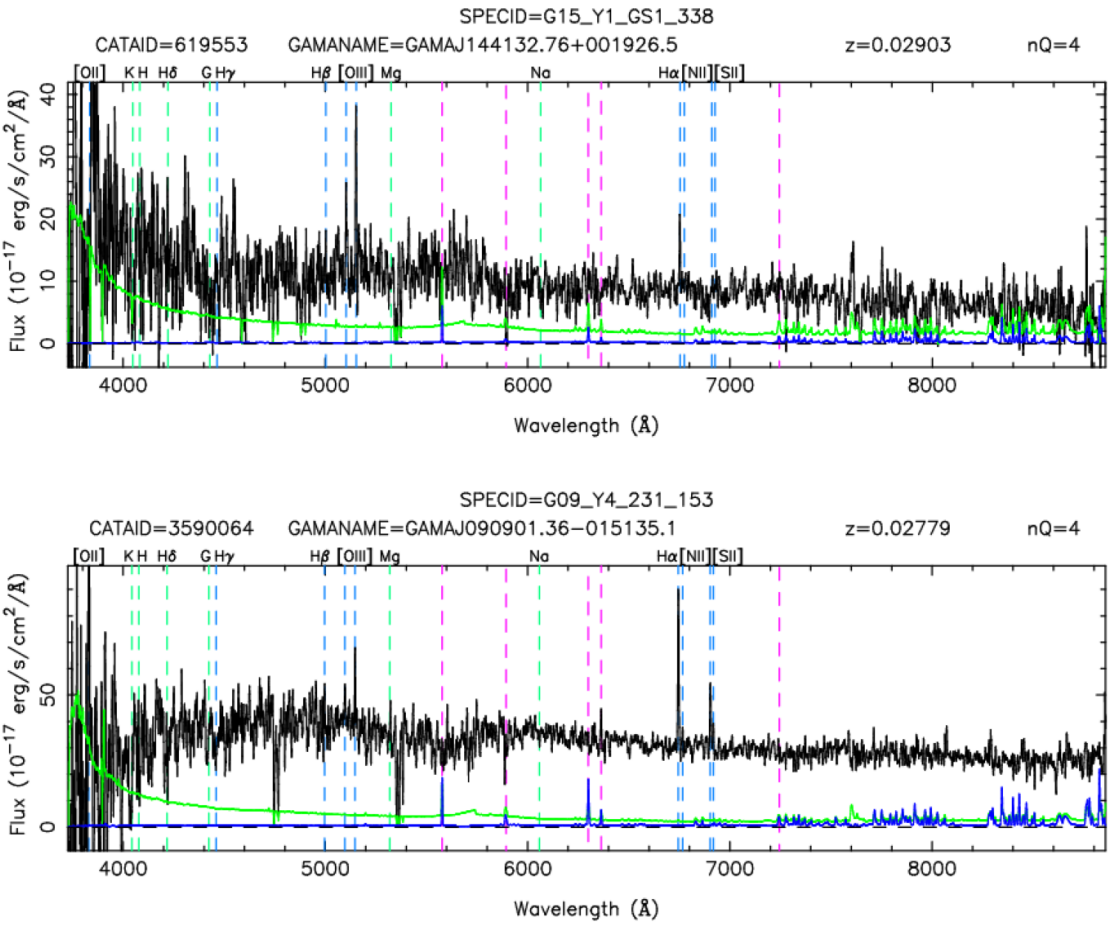

Figure 7.3: Example spectra of two galaxies classified as passive but showing clear evidence of ongoing SF. The black line shows the observed spectrum, the green line the 1σ uncertainty, and the blue line the sky spectrum (where available), smoothed over 5 pixels. The prominent Hα emission line confirms the presence of SF activity.

To investigate this, we visually inspected a random subsample of 20 galaxies with stellar masses below 10^9 $M_\odot$, examining both their images and spectra (Figs. 7.2 and 7.3, respectively). We find that ~20% of the galaxies classified as passive in this mass range show clear signs of ongoing SF. Although this result demonstrates that some level of contamination of the passive subsample by star-forming galaxies is present, it is not sufficient to account for the pronounced low-mass upturn that we observe in the passive GSMF (see panel (a) of Fig. 7.1).

The best-fit double Schechter parameters are tabulated in Table 7.1 and shown in Fig. 7.4. Following the approach of Project I, in these and similar tables and figures throughout this paper we only present our results regarding $M^\star$, α_1 and α_2, since we are more interested in any change of the shape of the mass function and less in its normalization.

We now investigate to what extent these results depend on the specific division between

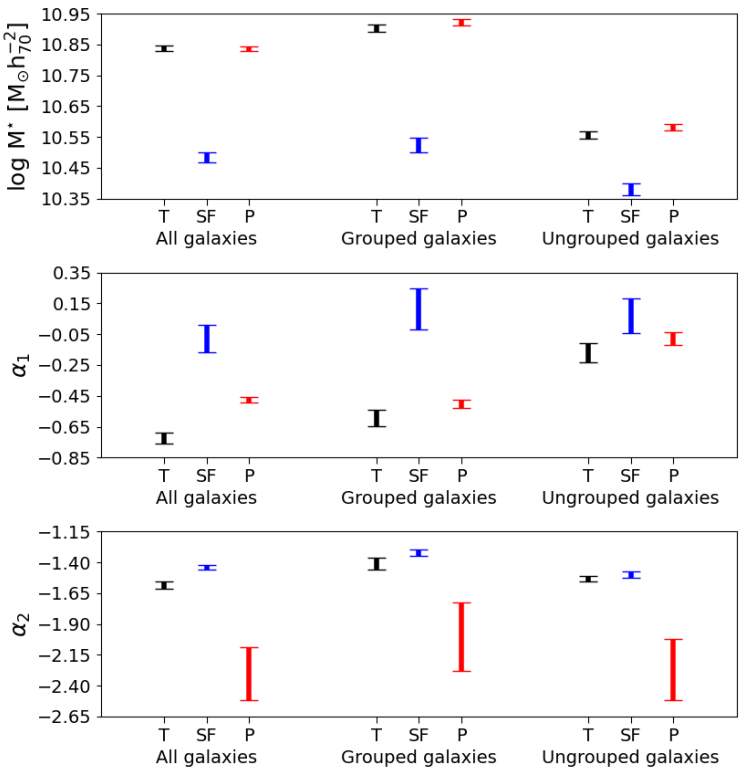

Figure 7.4: Best-fit double Schechter function parameters of the GSMFs shown in Fig. 7.1, using the same colour-coding. The x-axes distinguish between all, grouped, and ungrouped galaxies; within each sample, the three ticks correspond to the total (T), star-forming (SF), and passive (P) subsamples.

star-forming and passive galaxies, that is, how robust our best-fit double Schechter parameters are against small changes in the dividing line used to separate the two populations in Sect. 4.5. To address this, we perform the following experiment. We first identify the 1σ confidence region based on the posterior distribution of the slope and intercept defining our fiducial dividing line in the $\log M - \log \mathrm{SFR}$ plane. From this region, we randomly extract 100 different (slope, intercept) pairs. Each of these defines a slightly different separation between star-forming and passive galaxies. For each resulting star-forming subsample, we compute the corresponding GSMF and perform a double Schechter fit. This procedure allows us to estimate the sensitivity of the fitted parameters to small variations in the classification between the two populations. We find that the resulting uncertainty on $\log M^\star$ is ~ 0.02, i.e. of the same order of magnitude as the random error obtained using our fiducial dividing line (cf. Table 7.1), while the errors on α_1 and α_2 are subdominant in comparison (0.03 and 0.01, respectively). This test, performed on the star-forming population, suggests that our results are not significantly affected by small perturbations in the classification.

When considering our full parent sample as well as grouped and ungrouped galaxies, we find that the total GSMF is dominated by passive and star-forming galaxies at the high- and low-mass

Table 7.1: Best-fit double Schechter function parameters of the GSMFs of all, grouped, ungrouped, central, and satellite galaxies for different subsamples, as indicated.

All galaxy sample	$\log M^\star$ $(M_\odot\, h_{70}^{-2})$	α_1	α_2
total	10.84 ± 0.01	-0.72 ± 0.03	-1.58 ± 0.03
star-forming	10.48 ± 0.02	-0.08 ± 0.09	-1.44 ± 0.02
passive	10.83 ± 0.01	-0.48 ± 0.02	-2.30 ± 0.22
Grouped galaxy sample	$\log M^\star$ $(M_\odot\, h_{70}^{-2})$	α_1	α_2
total	10.90 ± 0.01	-0.59 ± 0.05	-1.41 ± 0.05
star-forming	10.52 ± 0.02	0.11 ± 0.13	-1.32 ± 0.03
passive	10.92 ± 0.01	-0.50 ± 0.03	-2.00 ± 0.28
Ungrouped galaxy sample	$\log M^\star$ $(M_\odot\, h_{70}^{-2})$	α_1	α_2
total	10.56 ± 0.01	-0.17 ± 0.06	-1.53 ± 0.02
star-forming	10.38 ± 0.02	0.07 ± 0.11	-1.50 ± 0.02
passive	10.58 ± 0.01	-0.08 ± 0.04	-2.27 ± 0.15
Central galaxy sample	$\log M^\star$ $(M_\odot\, h_{70}^{-2})$	α_1	α_2
total	10.85 ± 0.01	0.12 ± 0.06	-1.18 ± 0.05
star-forming	10.50 ± 0.03	0.64 ± 0.16	-1.05 ± 0.05
passive	10.84 ± 0.01	0.44 ± 0.13	...
Satellite galaxy sample	$\log M^\star$ $(M_\odot\, h_{70}^{-2})$	α_1	α_2
total	10.72 ± 0.02	-0.67 ± 0.10	-1.48 ± 0.07
star-forming	10.40 ± 0.03	0.13 ± 0.20	-1.43 ± 0.03
passive	10.74 ± 0.01	-0.66 ± 0.05	-1.92 ± 0.25

end, respectively (cf. Fig. 7.1). Notably, the characteristic mass $M^\star$ of the passive population almost coincides with that of the total sample in each case; in contrast, the low-mass slopes α_2 of the star-forming population are just slightly shallower compared to those of the total sample (cf. Fig. 7.4). We attribute these small discrepancies in $M^\star$ and α_2 to the use of different selection functions for the passive and star-forming subsamples, compared to the total populations. On the other hand, the star-forming population exhibits systematically lower $M^\star$ values compared to the total sample, while the passive population shows steeper (i.e. lower) α_2 values. Interestingly, the intermediate-mass slope α_1 of the total population is, in each case, steeper than those of the passive and star-forming components, and more closely resembles that of the passive population. These results confirm that star-forming and passive galaxies play a more prominent role in shaping the total GSMF at the low- and intermediate-to-high-mass regimes, respectively.

By comparing the grouped and ungrouped subsamples[1], we find that both star-forming and passive galaxies outside of groups show systematically lower $M^\star$ values than their counterparts residing in groups, as already expected from the results in Project I. This confirms that galaxies in groups are more likely to grow into more massive systems. In contrast, we observe that α_1 for passive galaxies is shallower outside of groups, indicating a relatively higher abundance of intermediate-mass passive objects. Furthermore, the low-mass slope α_2 is slightly steeper for both star-forming and passive galaxies outside of groups, suggesting a relatively lower abundance of low-mass galaxies.

Finally, we note that uncertainties on α_1 are relatively large for star-forming galaxies. This is because the two Schechter components intersect at relatively high masses, with the intermediate-mass component contributing significantly only at the high-mass end. As a result, its slope is poorly constrained. For passive galaxies, instead, the large errors on α_2 are due to the limited number of low-mass objects available. These results still hold in Sect. 7.1.3, where we further investigate the dependence of the GSMF on $M_{\rm halo}$ for both our star-forming and passive subsamples.

7.1.2 How the GSMF differs in central and satellites galaxies

We now investigate the GSMF in central and satellite galaxies. As discussed in Sect. 4.6, centrals and satellites are identified using the iterative method from the G^{3}C, which selects as central the brightest galaxy among the two closest to the group's centre of light. Following Vázquez-Mata et al. (2020), ungrouped galaxies are excluded from the central galaxy population.

In Fig. 7.5 we show the GSMFs for our central, satellite, and ungrouped galaxy populations, first considering the entire samples and then their subdivision into star-forming and passive galaxies (left- and right-hand panels, respectively). Their best-fit double Schechter parameters are tabulated in Table 7.1 and shown in Fig. 7.6.

When considering the entire samples, we find that the total GSMF is dominated by centrals and ungrouped galaxies at the high- and low-mass ends, respectively (cf. Fig. 7.5, left-hand panel). Notably, the characteristic mass $M^\star$ of central galaxies closely matches that of the total sample, with satellites and ungrouped galaxies showing progressively lower values. We note that

[1] In contrast to Project I, we do not apply any volume corrections here. Therefore, these are the actual mass functions, not the conditional ones.

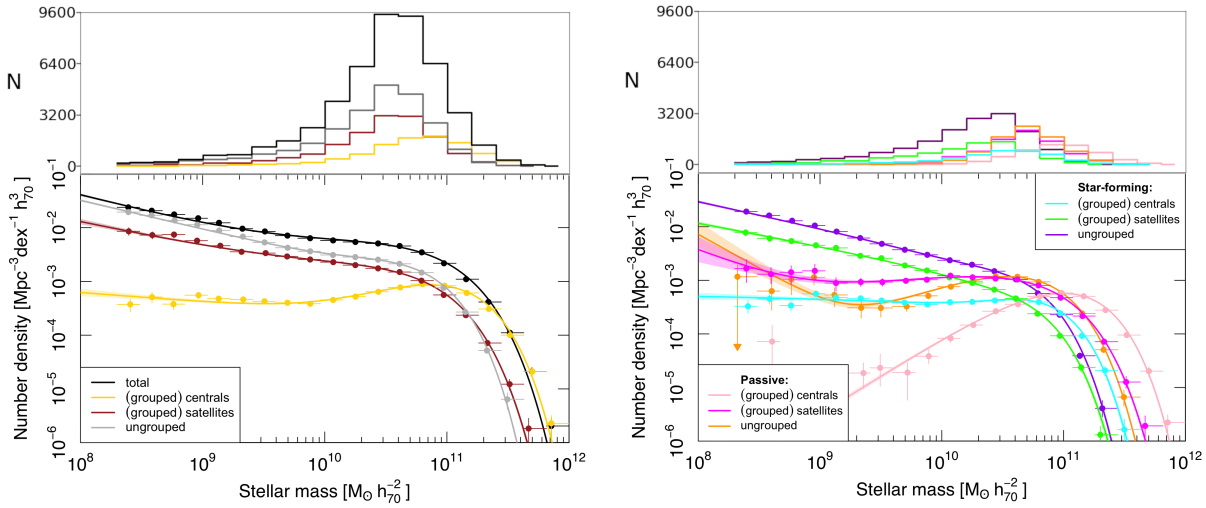

Figure 7.5: GSMFs for our total, central, satellite, and ungrouped galaxy populations, as indicated in the legend. The left-hand panel shows the GSMFs for each entire population, while the right-hand panel shows their subdivision into star-forming and passive galaxies. In each sub-figure, the lower panel shows the GSMFs, and the upper panel displays the raw number of galaxies as a function of stellar mass in each sample, as indicated.

the slightly higher $M^\star$ in centrals compared to the total sample is attributed to the use of different selection functions for the central and total populations. In contrast, the low-mass slope α_2 of ungrouped galaxies is very similar to that of the total sample, while satellites and centrals exhibit increasingly shallower slopes. This results in a decreasing trend for both $M^\star$ and α_2 from centrals to ungrouped galaxies (cf. Fig. 7.6). Interestingly, the intermediate-mass slope α_1 of satellites is in striking agreement with that of the total population, whereas both centrals and ungrouped galaxies show significantly higher (i.e. shallower) values. This may suggest that satellites play the dominant role in shaping the total GSMF in this stellar mass regime.

When splitting into star-forming and passive galaxies, we observe consistent trends across all populations. In each case, passive galaxies exhibit higher $M^\star$ values and steeper α_2 slopes compared to their star-forming counterparts (cf. Fig. 7.5, right-hand panel). The only exception is the α_2 values for central galaxies, since the passive subpopulation is best fit by a single Schechter function, for which only α_1 is defined. Specifically, we observe a decreasing trend for $M^\star$ from centrals to satellites to ungrouped galaxies, within both the star-forming and passive subpopulations. Notably, the $M^\star$ value of the central star-forming population is comparable to that of the all-star-forming galaxy sample, and the same holds for the passive central population with respect to the all-passive galaxy sample (cf. Table 7.1). We note that the slightly higher $M^\star$ values observed in centrals, both for the star-forming and passive subpopulations, are due to the use of different selection functions for the central and total populations.

This finding demonstrates that central star-forming and passive galaxies dominate the high-mass end of the corresponding total GSMFs. A similar trend is observed for α_2 within the star-

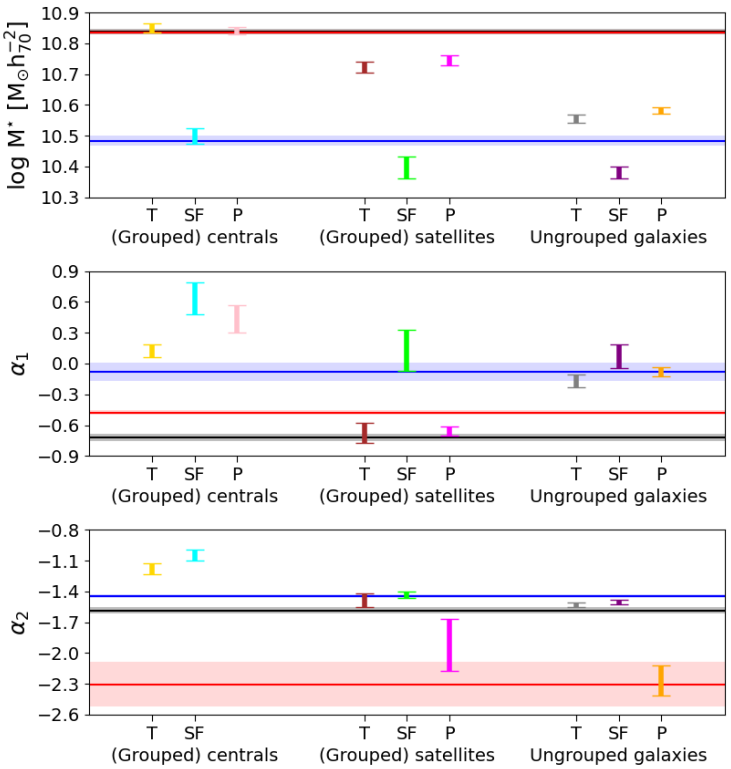

Figure 7.6: Best-fit double Schechter function parameters of the GSMFs shown in Fig. 7.5, using the same colour-coding. The x-axes distinguish between central, satellite, and ungrouped galaxies; within each sample, the three ticks correspond to the total (T), star-forming (SF), and passive (P) subsamples. The black, blue and red horizontal bands show the results for the full parent, all-star-forming and all-passive samples, respectively, taken from Fig. 7.4. These reference lines are meant to be compared only with the T, SF, and P values in each subsample, respectively.

forming subpopulation, with increasingly steeper slopes from centrals to satellites to ungrouped galaxies. For the passive subpopulation, although α_2 is not available for centrals, the slope still steepens from satellites to ungrouped galaxies. In particular, the α_2 value of the all-star-forming galaxy sample lies between those of the satellite and ungrouped populations, showing good agreement with both. In contrast, the all-passive galaxy sample exhibits a value of α_2 that is in striking agreement with that of the ungrouped passive population. These findings suggest that both satellite and ungrouped galaxies shape the low-mass end of the star-forming GSMF, whereas the passive GSMF in this regime is primarily shaped by ungrouped galaxies. For α_1, the trend remains consistent with the previous results only within the star-forming subpopulation, with increasingly steeper values from centrals to satellites to ungrouped galaxies. In particular, the α_1 value of the all-star-forming galaxy sample is comparable to those of the satellites and

ungrouped star-forming populations. For passive galaxies, the value of α_1 is closest to that of passive satellites, with centrals and ungrouped galaxies showing significantly higher values (i.e. shallower) values. We note that the difference in α_1 observed between the all-passive galaxy sample and the passive satellites is attributed to the use of different selection functions for the satellite and total populations. These findings suggest that both satellite and ungrouped galaxies shape the intermediate-mass regime of the star-forming GSMF, whereas the passive GSMF in this regime is predominantly shaped by satellite galaxies alone.

By comparing the grouped (both central and satellite) and ungrouped subsamples, we confirm the trends found in Sect. 7.1.1 regarding $M^\star$ and α_2. Isolated galaxies exhibit lower $M^\star$ and steeper α_2 values compared to galaxies in groups.

7.1.3 GSMF dependence on group halo mass

To study the dependence of the GSMF on group halo mass $M_{\rm halo}$, we are forced to discard 1055/11 579 (9.1%) of our groups for which the G^{3}C does not report any $M_{\rm dyn}$ values because the measured velocity dispersion of these groups is smaller than its error. These are overwhelmingly groups with multiplicity $N_{\rm FOF} = 2$. Our total sample now consists of 10 524 groups containing 34 931 galaxies.

We now bin galaxies according to the mass of the group that they belong to into four different bins in $\log[M_{\rm halo}/(M_\odot\, h_{70}^{-1})]$: $\leq$ 12.65, 12.65–13.3, 13.3–13.85, and $>$ 13.85. This choice is made to maintain approximately the same number of galaxies per bin. Our resulting GSMFs, colour-coded by $M_{\rm halo}$, are shown in Fig. 7.7. Panel (a) shows the GSMFs as a function of $M_{\rm dyn}$, while panels (b) and (c) further distinguish between passive and star-forming galaxies, and between central and satellite galaxies, respectively. Their best-fit double Schechter parameters are tabulated in Table 7.2 and shown in Fig. 7.8.

When we consider our entire grouped galaxy sample, we note that the characteristic mass $M^\star$ increases systematically with $M_{\rm dyn}$, indicating that more massive halos tend to host more massive galaxies. Both the intermediate-mass slope α_1 and the low-mass slope α_2 exhibit a similar trend, namely a mild steepening when moving from low- to intermediate-mass halos, followed by a progressive shallowing as $M_{\rm dyn}$ continues to increase. We note that the exceptionally high value of α_1 in the most massive halo bin reflects that the GSMF can be more accurately described by a single Schechter function, as the intermediate-mass component has negligible influence on the overall shape. Unsurprisingly, our findings are essentially identical with the main results of Project I, where we investigated the dependence of the GSMF on $M_{\rm halo}$ using four different halo mass estimators, despite the use of a different photometry and revised stellar mass estimates in the present analysis.

When we further distinguish between passive and star-forming galaxies, we observe distinct behaviours in the evolution of $M^\star$. Passive galaxies follow a consistent trend similar to the overall sample, with $M^\star$ increasing steadily as $M_{\rm dyn}$ grows. Star-forming galaxies show a similar trend, except for the highest halo mass bin where $M^\star$ actually decreases. This decline may reflect environmental effects suppressing SF in the most massive halos. However, passive galaxies show consistently higher $M^\star$ values than star-forming galaxies, confirming their tendency to be more massive at fixed halo mass. Regarding α_2, both populations exhibit a consistent trend similar

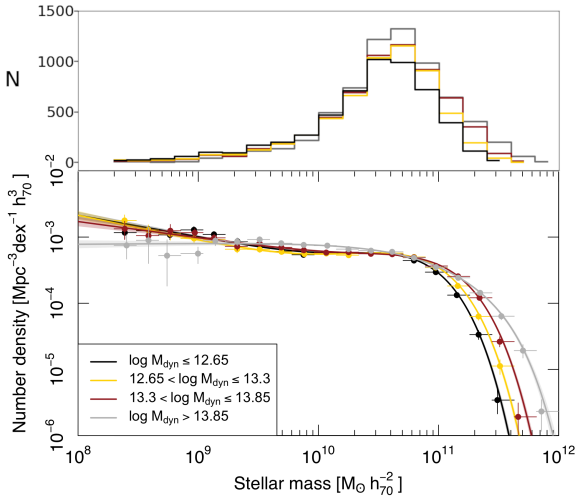

(a) All grouped galaxies

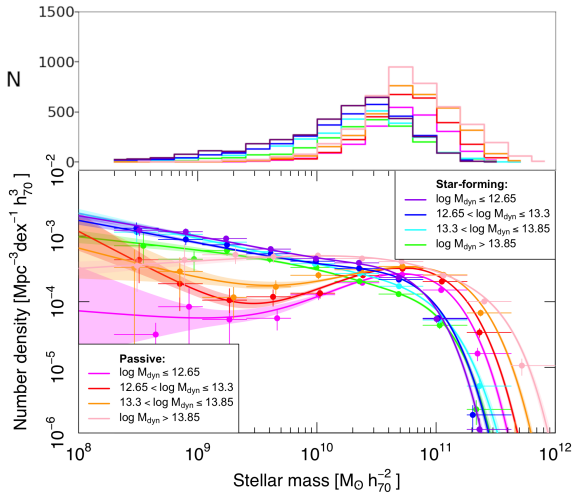

(b) Grouped passive vs star-forming galaxies

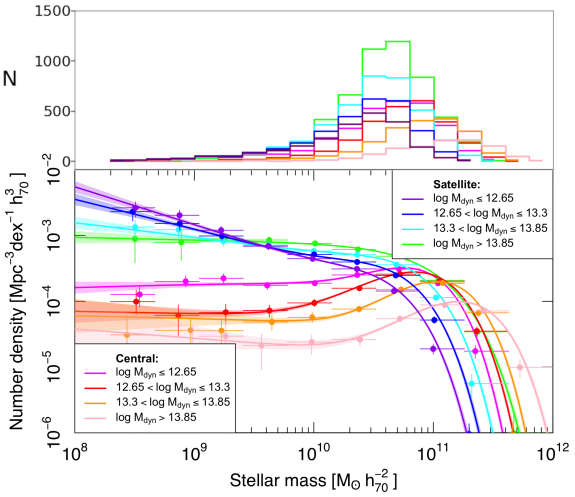

(c) Central vs satellite galaxies

Figure 7.7: GSMFs of our grouped galaxy subsample colour-coded by $M_{\rm halo}$, as indicated in the legend. Panel (a) shows the GSMFs as a function of $M_{\rm dyn}$, while panels (b) and (c) further distinguish between passive and star-forming galaxies, and between central and satellite galaxies, respectively. In each subfigure, the lower panel shows the GSMFs, and the upper panel displays the raw number of galaxies as a function of stellar mass in each sample, as indicated.

Table 7.2: Best-fit double Schechter function parameters of the GSMFs of grouped galaxies for different subsamples, as indicated.

All grouped galaxy sample	$\log M^\star$ $(M_\odot\, h_{70}^{-2})$	α_1	α_2
$\log(\frac{M_{\rm dyn}}{M_\odot h_{70}^{-1}}) \leq 12.65$	10.61 ± 0.02	0.07 ± 0.12	-1.32 ± 0.05
$12.65 < \log(\frac{M_{\rm dyn}}{M_\odot h_{70}^{-1}}) \leq 13.3$	10.71 ± 0.02	-0.14 ± 0.11	-1.38 ± 0.06
$13.3 < \log(\frac{M_{\rm dyn}}{M_\odot h_{70}^{-1}}) \leq 13.85$	10.82 ± 0.03	-0.06 ± 0.16	-1.24 ± 0.06
$\log(\frac{M_{\rm dyn}}{M_\odot h_{70}^{-1}}) > 13.85$	11.00 ± 0.06	0.95 ± 0.23	-0.99 ± 0.03
Grouped passive galaxy sample	$\log M^\star$ $(M_\odot\, h_{70}^{-2})$	α_1	α_2
$\log(\frac{M_{\rm dyn}}{M_\odot h_{70}^{-1}}) \leq 12.65$	10.63 ± 0.03	0.23 ± 0.21	-1.15 ± 0.49
$12.65 < \log(\frac{M_{\rm dyn}}{M_\odot h_{70}^{-1}}) \leq 13.3$	10.73 ± 0.02	-0.02 ± 0.07	-1.95 ± 0.29
$13.3 < \log(\frac{M_{\rm dyn}}{M_\odot h_{70}^{-1}}) \leq 13.85$	10.86 ± 0.03	-0.15 ± 0.17	-1.48 ± 0.31
$\log(\frac{M_{\rm dyn}}{M_\odot h_{70}^{-1}}) > 13.85$	10.95 ± 0.06	1.17 ± 0.29	-0.88 ± 0.05
Grouped star-forming galaxy sample	$\log M^\star$ $(M_\odot\, h_{70}^{-2})$	α_1	α_2
$\log(\frac{M_{\rm dyn}}{M_\odot h_{70}^{-1}}) \leq 12.65$	10.41 ± 0.04	0.28 ± 0.20	-1.30 ± 0.04
$12.65 < \log(\frac{M_{\rm dyn}}{M_\odot h_{70}^{-1}}) \leq 13.3$	10.51 ± 0.04	0.07 ± 0.23	-1.34 ± 0.06
$13.3 < \log(\frac{M_{\rm dyn}}{M_\odot h_{70}^{-1}}) \leq 13.85$	10.64 ± 0.06	-0.15 ± 0.29	-1.38 ± 0.05
$\log(\frac{M_{\rm dyn}}{M_\odot h_{70}^{-1}}) > 13.85$	10.49 ± 0.05	0.82 ± 0.27	-1.19 ± 0.06
Central galaxy sample	$\log M^\star$ $(M_\odot\, h_{70}^{-2})$	α_1	α_2
$\log(\frac{M_{\rm dyn}}{M_\odot h_{70}^{-1}}) \leq 12.65$	10.55 ± 0.03	0.83 ± 0.17	-0.95 ± 0.06
$12.65 < \log(\frac{M_{\rm dyn}}{M_\odot h_{70}^{-1}}) \leq 13.3$	10.67 ± 0.02	0.56 ± 0.13	-1.03 ± 0.13
$13.3 < \log(\frac{M_{\rm dyn}}{M_\odot h_{70}^{-1}}) \leq 13.85$	10.75 ± 0.03	0.67 ± 0.17	-1.04 ± 0.15
$\log(\frac{M_{\rm dyn}}{M_\odot h_{70}^{-1}}) > 13.85$	10.99 ± 0.04	0.71 ± 0.21	-1.14 ± 0.24
Satellite galaxy sample	$\log M^\star$ $(M_\odot\, h_{70}^{-2})$	α_1	α_2
$\log(\frac{M_{\rm dyn}}{M_\odot h_{70}^{-1}}) \leq 12.65$	10.36 ± 0.04	-0.11 ± 0.25	-1.57 ± 0.08
$12.65 < \log(\frac{M_{\rm dyn}}{M_\odot h_{70}^{-1}}) \leq 13.3$	10.43 ± 0.04	0.04 ± 0.23	-1.45 ± 0.08
$13.3 < \log(\frac{M_{\rm dyn}}{M_\odot h_{70}^{-1}}) \leq 13.85$	10.54 ± 0.04	0.10 ± 0.25	-1.22 ± 0.08
$\log(\frac{M_{\rm dyn}}{M_\odot h_{70}^{-1}}) > 13.85$	10.83 ± 0.06	-0.25 ± 0.28	-1.04 ± 0.07

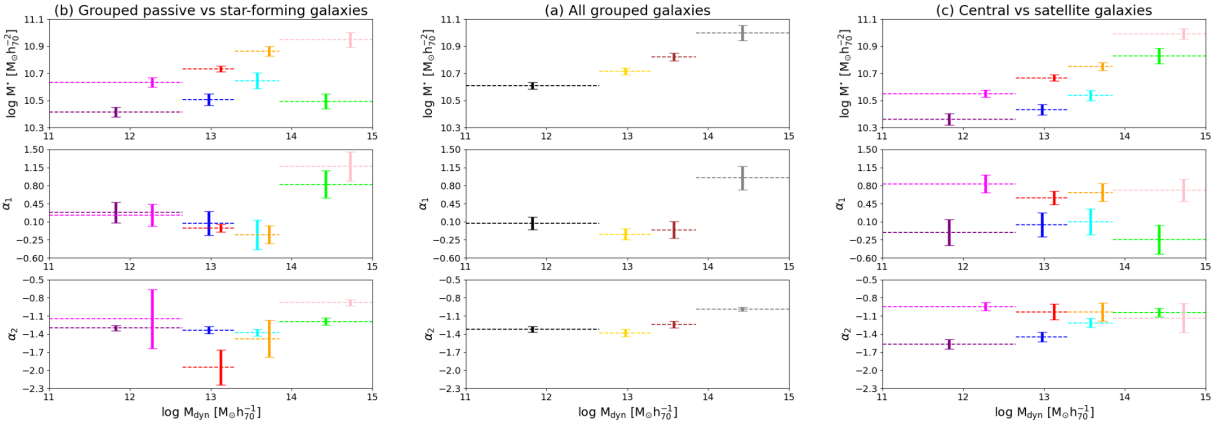

Figure 7.8: Best-fit double Schechter function parameters of the GSMFs shown in Fig. 7.7, using the same colour-coding by $M_{\rm halo}$. Panel (a) is displayed in the centre, while panels (b) and (c) are on the left and right, respectively. For clarity, the vertical error bars corresponding to the passive galaxies in the left-hand panel and the centrals in the right-hand panel have been slightly offset to the right.

to the overall sample, namely a steepening from low to intermediate halo masses, followed by a shallowing as $M_{\rm dyn}$ continues to increase. However, this trend is more pronounced in passive galaxies, which show a stronger steepening and subsequent flattening. In contrast, star-forming galaxies display a milder but more extended steepening, with the shallowing occurring only at the highest halo mass bin. Similarly, α_1 shows a comparable evolution for both star-forming and passive galaxies. In both cases, there is a steepening with increasing $M_{\rm dyn}$, followed by a shallowing at the most massive halos. As previously noted for the entire grouped galaxy sample, the exceptionally high values of α_1 in the highest halo mass bin likely indicate that the intermediate-mass component contributes negligibly to the shape of the GSMF. Consequently, those mass functions are better represented by a single Schechter function, with the intermediate-mass slope effectively losing its physical meaning.

When we separate galaxies into centrals and satellites, $M^\star$ still increases steadily with $M_{\rm dyn}$, regardless of the population, indicating that more massive halos host more massive galaxies. However, central galaxies show consistently higher values than satellites, confirming their tendency to be more massive at fixed halo mass. Regarding α_2, central galaxies exhibit a mild but progressive steepening as $M_{\rm dyn}$ increases. This indicates that the relative abundance of low-mass centrals gradually grows in more massive halos. In contrast, satellite galaxies show the opposite behaviour, namely α_2 becomes progressively shallower with increasing $M_{\rm dyn}$, indicating a relative decrease in the number of low-mass satellites in more massive halos. Concerning α_1, central galaxies follow a trend similar to that observed in the overall sample, with a steepening from low to intermediate halo masses, followed by a progressive shallowing as $M_{\rm dyn}$ continues to increase. In contrast, satellites exhibit the opposite trend, with α_1 becoming shallower as $M_{\rm dyn}$ increases and then steepening in the highest halo mass bin. These distinct behaviours for central and satellite galaxies presumably reflect different quenching mechanisms shaping these galaxy populations.

7.2 Discussion

In this section, we discuss and compare our results on the variation of the GSMF in star-forming and passive galaxies (Sect. 7.2.1), centrals and satellites (Sect. 7.2.2), and as a function of group halo mass (Sect. 7.2.3), in the context of other similar studies.

7.2.1 How the GSMF differs in star-forming and passive galaxies

Peng et al. (2010) present an empirical model describing galaxy evolution based on observations from the Sloan Digital Sky Survey (SDSS) and zCOSMOS, emphasizing the roles of mass and environment. The study demonstrates that the effects of mass and environment on galaxy quenching are fully separable up to redshift $z \sim 1$. This suggests distinct mechanisms are at play, where mass quenching is related to a galaxy's SFR, and environment quenching is linked to the growth of large-scale cosmic structures. The physical mechanism for mass quenching is not definitively known, but may involve feedback linked to SF or AGN. In contrast to the ongoing nature of mass quenching, environment quenching seems to be a "once-only" process, possibly related to satellite quenching as galaxies fall into larger DM halos. The fraction of quenched satellites ranges from 30% to 70%, depending on the environment (its impact is most evident at lower masses and in high-density regions). The combination of these two quenching processes, plus some additional quenching due to merging, naturally produces (1) a quasi-static single Schechter mass function for star-forming galaxies with an exponential cut-off at a value $M^\star$ that is set uniquely by the constant of proportionality between the SF and mass quenching rates, and (2) a double Schechter function for passive galaxies. Remarkably, the characteristic mass of the star forming population remains constant up to redshift $z \sim 2$, indicating a universal efficiency of mass quenching over cosmic time. For the passive population, the dominant component (at high masses) is produced by mass quenching and shares the same $M^\star$ as star-forming galaxies but has a low-mass slope $\alpha_{1,\mathrm{P}}$ differing by approximately $\alpha_{1,\mathrm{P}} - \alpha_{\mathrm{SF}} \approx 1$. The other component is produced by environment effects and has the same $M^\star$ and $\alpha_{2,\mathrm{P}}$ as star-forming galaxies, but lower amplitude depending on the environment, with high-density environments showing a stronger component. Post-quenching dry merging modifies the mass functions slightly in denser environments. Mergers shift $M^\star$ to slightly higher values and make $\alpha_{2,\mathrm{P}}$ slightly more negative, with a relationship of roughly $\alpha_{1,\mathrm{P}} - \alpha_{\mathrm{SF}} \approx 1.6$. However, the influence of dry mergers is relatively minor, resulting in mass increases of only $15\% - 40\%$ in the densest regions.

Several key predictions of the empirical model proposed by Peng et al. (2010) are not supported by our results. The only qualitative agreement that we observe is in the functional form of the GSMFs. Specifically, we confirm that both the total and the passive populations are best described by a double Schechter function fit, whereas the star-forming population is well approximated by a single Schechter function. Although we show that a double Schechter fit provides a marginally better representation, the transition between the two components occurs at very high stellar masses. As a consequence, the star-forming GSMF is dominated by its low-mass component across most of its mass range, and its overall shape closely resembles a single Schechter function, consistent with Peng et al. (2010). Nonetheless, our analysis shows that adding a second component produces a slight improvement in the fit, possibly reflecting early

signs of quenching at the intermediate-mass regime of the star-forming population. However, except for this structural similarity, our results diverge significantly from the predictions of Peng et al. (2010).

A comparison between the best-fit double Schechter function parameters from Peng et al. (2010) and our results is shown in Table 7.3. To investigate the role of environment in shaping the GSMF, we also compare our measurements for grouped and ungrouped galaxies with the high- and low-density bins (D4 and D1, respectively) presented by Peng et al. (2010). While our environmental classification is based on group membership within the GAMA survey, Peng et al. (2010) use local overdensity quartiles derived from the zCOSMOS sample, where density is estimated via the fifth nearest neighbour method. Although these approaches may trace different physical structures, they still provide a useful basis for a meaningful qualitative comparison of environmental effects on the GSMF.

First, contrary to their model's prediction that the characteristic stellar mass $M^\star$ should be the same for star-forming and passive galaxies, regardless of environment, we find much larger discrepancies between the two populations. Whereas Peng et al. (2010) report a difference of $\Delta M^\star \approx 0.05$ dex between their full star-forming and passive samples, and a maximum offset of $\Delta M^\star \approx 0.16$ dex when comparing their star-forming D1 and passive D4 bins, our results show significantly larger variations, with $\Delta M^\star \approx 0.35$ dex for our full samples and up to $\Delta M^\star \approx 0.54$ dex between our grouped and ungrouped subsamples. Similarly, the low-mass slope α_2, which in Peng et al. (2010) is nearly identical for star-forming and passive galaxies, both for the full samples and across different environments, differs substantially in our results. Regardless of our environmental classification (i.e. full sample, grouped, or ungrouped galaxies), we find that the α_2 value for passive galaxies is significantly steeper than those of star-forming and total populations, which instead display relatively similar values.

Interestingly, one prediction from Peng et al. (2010) that still holds in our results is the relation $\alpha_{1,\mathrm{P}} - \alpha_{\mathrm{SF}} \approx 1$, which we confirm for both our full sample (= 0.96) and our grouped galaxy population (= 0.82). However, this trend does not extend to ungrouped galaxies, for which $\alpha_{1,\mathrm{P}} - \alpha_{\mathrm{SF}} = 1.42$, suggesting that the connection between star-forming and passive slopes may be more sensitive to the environment than previously thought.

We note here that our classification of galaxies into star-forming and passive populations is based on direct measurements of SF activity via Hα emission, as opposed to broad-band photometric colours as used by Peng et al. (2010). This choice may partly account for the discrepancies that we observe in our results.

Finally, we have tested whether the differences in the $M^\star$ values between star-forming and passive galaxies could be driven by our choice of the fitting function (i.e. using a double instead of a single Schechter parametrization). When fitting the star-forming population with a single Schechter function, as done by Peng et al. (2010), the inferred $M^\star$ shifts to higher values, partially reducing the discrepancies with the passive population. Specifically, $M^\star$ increases from $10^{10.48}$ to $10^{10.74}$ $M_\odot$ for the full sample, from $10^{10.52}$ to $10^{10.80}$ $M_\odot$ for the grouped subsample, and from $10^{10.38}$ to $10^{10.68}$ $M_\odot$ for the ungrouped subsample. Although a significant mismatch with the $M^\star$ value of the passive population persists in all cases, a large part of the star-forming/passive $M^\star$ discrepancy rests on our choice of representing the star-forming population with a double Schechter function. Hence, the question arises as to how robust this choice is to variations of our

Table 7.3: Best-fit double Schechter function parameters of the GSMFs of blue/star-forming and red/passive galaxies for different works, as indicated. Ellipses in the α_1 column denote that a single Schechter function was used. Values of α_2 shown in parentheses without uncertainties were not fitted but just fixed to the global value adopted in the corresponding study.

Sample	$\log M^\star$ $(M_\odot\, h_{70}^{-2})$	α_1	α_2
Global – Peng et al. (2010)	10.67 ± 0.01	-0.52 ± 0.04	-1.56 ± 0.12
Global – Weigel et al. (2016)	10.79 ± 0.01	-0.79 ± 0.04	-1.69 ± 0.10
Global – this work	10.84 ± 0.01	-0.72 ± 0.03	-1.58 ± 0.03
Blue – Peng et al. (2010)	10.63 ± 0.01	...	-1.40 ± 0.01
Blue – Weigel et al. (2016)	10.60 ± 0.01	...	-1.21 ± 0.01
Star-forming – this work	10.48 ± 0.02	-0.08 ± 0.09	-1.44 ± 0.02
Red – Peng et al. (2010)	10.68 ± 0.01	-0.39 ± 0.03	(-1.56)
Red – Weigel et al. (2016)	10.77 ± 0.01	-0.45 ± 0.02	-2.46 ± 0.33
Passive – this work	10.83 ± 0.01	-0.48 ± 0.02	-2.30 ± 0.22
Blue D1 – Peng et al. (2010)	10.60 ± 0.01	...	-1.39 ± 0.02
Star-forming ungrouped – this work	10.38 ± 0.02	0.07 ± 0.11	-1.50 ± 0.02
Blue D4 – Peng et al. (2010)	10.64 ± 0.02	...	-1.41 ± 0.04
Star-forming grouped – this work	10.52 ± 0.02	0.11 ± 0.13	-1.32 ± 0.03
Red D1 – Peng et al. (2010)	10.61 ± 0.01	-0.36 ± 0.05	(-1.56)
Passive ungrouped – this work	10.58 ± 0.01	-0.08 ± 0.04	-2.27 ± 0.15
Red D4 – Peng et al. (2010)	10.76 ± 0.02	-0.55 ± 0.06	(-1.56)
Passive grouped – this work	10.92 ± 0.01	-0.50 ± 0.03	-2.00 ± 0.28

star-forming/passive classification method.

In Sect. 7.1.1 we already investigated the sensitivity of the fitted double Schechter function parameters to variations of our dividing line used to separate star-forming and passive galaxies. We now also test the robustness of the model selection in favour of the double Schechter function. For each of the 100 pairs extracted from the 1σ confidence region of our fiducial dividing line in the $\log M$ – log SFR plane, we perform the GSMF fit using both a single and a double Schechter function, and compute different model selection statistics such as the log-likelihood ratio test (LRT), the Bayesian information criterion (BIC; Schwarz 1978), the Akaike information criterion (AIC; Akaike 1974), and the Bayesian evidence[2].

[2]The LRT compares the goodness-of-fit of two nested models, where one (e.g. the single Schechter) is a special case of the other (e.g. the double Schechter) and is defined as: $\mathcal{R} = -2 \ln \mathcal{L}_{\rm single} + 2 \ln \mathcal{L}_{\rm double}$, where $\ln \mathcal{L}_{\rm single}$ and $\ln \mathcal{L}_{\rm double}$ represent the maximum log-likelihoods obtained from fitting the single and double Schechter functions, respectively. This statistic quantifies the improvement in fit when moving from the simpler to the more complex model. Hence, starting from the maximum log-likelihood $\ln \mathcal{L}$, the BIC is defined as $\mathrm{BIC} = -2 \ln \mathcal{L} + k \ln n$, while the AIC as $\mathrm{AIC} = 2k - 2 \ln \mathcal{L}$, where k is the number of model parameters and n the number of data points. The differences in BIC and AIC values between single and double Schechter models, RBIC and RAIC respectively,

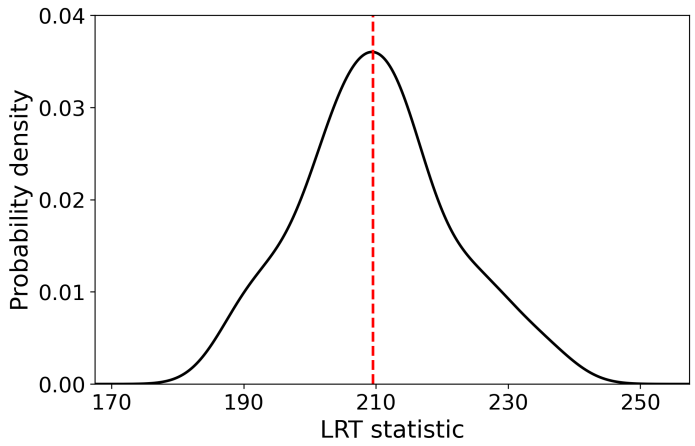

Figure 7.9: Distribution of the LRT statistic obtained from 100 star-forming subsamples. The red dashed line marks our observed LRT value, which lies near the peak of the simulated distribution. This compatibility suggests that the data are consistent with the double Schechter model representing the true distribution, whereas the single Schechter function fails to provide an accurate description.

The LRT values, as well as the differences in BIC and AIC between the single and double Schechter models, are consistently very high. According to the scale proposed by Jeffreys (1939), such values provide decisive evidence in support of the more complex model (i.e. double Schechter). Likewise, the strongly negative differences in Bayesian evidence further confirm that the double Schechter representation is robust to small changes in the classification process. In particular, we explore the distribution of the LRT statistic derived from the 100 different star-forming subsamples, and shown in Fig. 7.9. Our observed LRT value, shown as a red dashed line, lies near the peak of the simulated distribution, which exhibits no significant tails towards lower or higher values. This finding indicates that, regardless of how the dividing line is perturbed within the 1σ region, the double Schechter model reliably provides a significantly better fit to the data. Therefore, our preference for a double Schechter function is well justified and not an artefact of how we select star-forming and passive galaxies. We thus conclude that the discrepancies that we observe with the results of Peng et al. (2010) cannot be attributed to the functional form alone, but rather arise from real deviations in the assumptions of their model.

Taylor et al. (2015) investigate the GSMFs for their blue/star-forming (B-type) as well as red/passive (R-type) populations, based on a sample of $M_\star > 10^{8.7}\ M_\odot$ and $z < 0.12$ galaxies from the GAMA survey. The aim of this work is to show how different definitions of red and blue galaxies impact the resulting GSMFs. When modelling the GSMFs, they use a double Schechter function for both subsamples. For the B-type population, the secondary component detects a small deficit of galaxies observed in the range $10^{10} - 10^{10.3}\ M_\odot$, which corresponds to the apparent upturn observed in the overall GSMF. This results in a slightly more complex shape that cannot be fully described by a single Schechter function. For the R-type population, in contrast, the secondary component becomes negligible above $10^{9.5}\ M_\odot$, failing to reproduce the apparent

quantify the relative preference for one model over the other. Finally, the Bayesian evidence provides a fully Bayesian approach by integrating the likelihood over the prior distribution of the model parameters.

low-mass upturn in the red GSMF observed by Peng et al. (2010). This discrepancy is mainly due to broader selection criteria for the red population, which includes a significant number of star-forming galaxies with young stellar populations. Such misclassifications are particularly common at low masses, where red galaxies are intrinsically rare, and a simple colour cut would classify the reddest tail of the blue population as red galaxies. As a result, differences in selection criteria can lead to discrepancies of up to an order of magnitude in the inferred number densities of low-mass red galaxies. It is important to note, however, that Taylor et al. (2015) do detect a similar low-mass upturn in their R-type GSMF. This upturn is more pronounced when the B/R classification is based on the intrinsic, rather than the restframe, CMD. However, they do not consider this feature to be robust. Specifically, they find no conclusive statistical evidence that a second Schechter component is required to fit the red population, and they attribute the observed upturn to systematic uncertainties and selection effects.

We also confirm that the double Schechter function provides a better representation of both blue/star-forming and red/passive galaxies. However, we do not find strong evidence that the apparent upturn in the overall GSMF is primarily driven by the blue population. In contrast to Taylor et al. (2015), we clearly observe a low-mass upturn in the red population, which is more evident for ungrouped than grouped galaxies, but still present when considering the full passive sample (cf. Fig. 7.1). Although we confirm that the low-mass Schechter component of the red GSMF becomes negligible above $M_\star \approx 10^{9.5}\ M_\odot$, the upturn we observe may also be due to the fact that our sample extends down to $M_\star \approx 10^{8.3}\ M_\odot$, somewhat deeper than the limit of $10^{8.7}\ M_\odot$ adopted by Taylor et al. (2015). In comparison with previous works and with the results presented in this study, Taylor et al. (2015) find a significantly higher number of B-type galaxies at $M_\star \geq 10^{10}\ M_\odot$ and a much steeper decline in their GSMF at $M_\star \geq 10^{10.8}\ M_\odot$. As a result, the stellar mass at which the blue and red mass functions intersect shifts from 10^{10} – $10^{10.3}\ M_\odot$ to $\approx 10^{10.5}\ M_\odot$. In contrast, while the R-type GSMF remains relatively flat below $10^{10.5}\ M_\odot$ and is systematically lower at low masses compared to the red GSMFs available in the literature, we find excellent agreement at the very low-mass end in terms of number density between our all-passive GSMF and the R-type GSMF of Taylor et al. (2015). This consistency is particularly evident when the B/R classification is based on the intrinsic, rather than the restframe, CMD. The smooth decline of the R-type fraction toward lower stellar masses observed by Taylor et al. (2015) indicates that stellar mass is not the primary factor in determining galaxy type. In other words, while more massive galaxies are more likely to host older stellar populations, quenching cannot be attributed to stellar mass alone.

Weigel et al. (2016) present a comprehensive study of the GSMF at $0.02 \leq z \leq 0.06$, using data from the SDSS DR7. Their analysis investigates how the GSMF depends on various galaxy properties and environmental parameters. To this end, the main sample is divided into more than 130 subsamples based on morphology, colour, sSFR, central/satellite classification, halo mass, and local density. They do not impose any prior assumptions on the functional form of the mass functions. Instead, for each subsample, they independently evaluate both single and double Schechter fits and use a likelihood ratio test to identify the model that best describes the data. The classification of blue and red galaxies does not follow the method of Taylor et al. (2015), but rather relies on two linear cuts in the CMD, which identify blue, red, and intermediate green galaxies lying between the two cuts. Blue galaxies are generally well described by a single

Schechter function with a relatively steep low-mass slope, whereas red galaxies show an upturn at the low-mass end, which requires a double Schechter fit. Weigel et al. (2016) argue that different definitions of blue and red galaxies can significantly affect the shapes of the resulting GSMFs, particularly at the low-mass end. In fact, they find their blue and red GSMFs to be systematically lower than those presented by Peng et al. (2010) and Baldry et al. (2012), likely because they explicitly identify a green valley population, which reduces the number densities of both blue and red galaxies. Nevertheless, their GSMFs are more consistent with those of Taylor et al. (2015) and with our own, despite the use of a double Schechter function for the blue population in both our work and that of Taylor et al. (2015).

A direct comparison of the best-fit double Schechter parameters (Table 7.3) shows that the total and red GSMFs presented by Weigel et al. (2016) are remarkably consistent with our mass functions, and significantly closer than those reported by Peng et al. (2010). In particular, the values of $M^\star$ for both the total and red populations differ by $\approx$0.05 dex, whereas the slopes α_1 and α_2 are consistent within the uncertainties. This agreement is particularly notable given the differences in methodology and classification criteria. For the blue population, however, the discrepancy is more pronounced. Weigel et al. (2016) find a higher $M^\star$ and a significantly shallower α_2. This difference is attributed to our use of a double Schechter function, which provides a better fit to the mass function, particularly around the intermediate-mass regime, and likely results in a lower $M^\star$ and a steeper α_2.

7.2.2 How the GSMF differs in central and satellite galaxies

In a follow-up study, Peng et al. (2012) investigate the environmental effects on galaxy evolution, focusing on the quenching of satellite galaxies within SDSS groups. In their work, they distinguish between central (including isolated singletons) and satellite galaxies. They find that the environmental quenching effects identified in Peng et al. (2010) can be entirely attributed to the satellites, while central galaxies are affected only by internal, mass-dependent processes. For centrals, the red fraction depends solely on stellar mass and shows no dependence on environmental factors such as local overdensity or halo mass. This suggests that centrals undergo quenching through a process linked to their own mass only (i.e. mass quenching). In contrast, the red fraction of satellites increases with both stellar mass and local overdensity, but interestingly not with global group properties like richness or the parent DM halo mass. Moreover, the fraction of blue central galaxies that are quenched when they become satellites (the so-called "satellite quenching efficiency") is found to be largely independent of stellar mass but strongly dependent on local overdensity (which reflects a galaxy's position within the group) rather than the overall DM halo mass. The phenomenological model adopted in Peng et al. (2010) also predicts the GSMFs of star forming and passive centrals and satellites. In particular, the star forming population, whether it consists of centrals or satellites, follow a single Schechter function with the same $M^\star$, which is independent of halo mass (above $10^{12} M_\odot$). This confirms the universality of the mass-quenching process, which operates through the same physical mechanism for both types of galaxies, unaffected by their environment. For the passive population, centrals are well described by a single Schechter, whereas satellites require a double Schechter function, with one component attributed to mass quenching and the other to satellite quenching. Interestingly, the impact of

Table 7.4: Best-fit double Schechter function parameters of the GSMFs of central and satellite galaxies for different works, as indicated.

Sample	$\log M^\star$ $(M_\odot\, h_{70}^{-2})$	α_1	α_2
Centrals – Weigel et al. (2016)	10.80 ± 0.01	-0.51 ± 0.09	-1.16 ± 0.05
Centrals – this work	10.85 ± 0.01	0.12 ± 0.06	-1.18 ± 0.05
Satellites – Weigel et al. (2016)	10.71 ± 0.02	-0.84 ± 0.08	-1.83 ± 0.23
Satellites – this work	10.72 ± 0.02	-0.67 ± 0.10	-1.48 ± 0.07
Blue centrals – Peng et al. (2012)	10.61 ± 0.01	...	-1.32 ± 0.02
Star-forming centrals and ungrouped – this work	10.50 ± 0.02	-0.10 ± 0.10	-1.44 ± 0.02
Red centrals – Peng et al. (2012)	10.70 ± 0.02	-0.33 ± 0.04	...
Passive centrals and ungrouped – this work	10.84 ± 0.01	-0.26 ± 0.08	...
Blue satellite – Peng et al. (2012)	10.59 ± 0.02	...	-1.56 ± 0.03
Star-forming satellite – this work	10.40 ± 0.03	0.13 ± 0.20	-1.43 ± 0.03
Red satellite – Peng et al. (2012)	10.61 ± 0.02	-0.49 ± 0.08	(-1.5)
Passive satellite – this work	10.74 ± 0.01	-0.66 ± 0.05	-1.92 ± 0.25

post-quenching merging is found to be modest and affects mainly central galaxies, increasing the stellar masses of passive centrals by about 25% but not altering significantly the shape of the mass function.

If we adopt a similar classification, i.e. defining as centrals both central galaxies in groups and isolated singletons, we find that our results are broadly consistent with this framework. In terms of functional form, we show that the GSMF of the passive central population is well described by a single Schechter function, in line with the results of Peng et al. (2012), who associate this shape with only mass quenching. Similarly, the GSMFs of the star-forming population, whether centrals or satellites, can also be reasonably fitted with a single Schechter function. Although a double Schechter may offer a slightly more accurate fit, the α_1 values being very close to zero suggest that the intermediate-mass component does not play a significant role. Therefore, the only subsample that clearly requires a double Schechter function fit is the passive satellite population, as also shown by Peng et al. (2012), where the excess at low masses is attributed to environment (satellite) quenching.

In Table 7.4, we also provide a comparison of the best-fit double Schechter function parameters from Peng et al. (2012) with our results. Although the values differ, possibly due to differences in photometry, stellar mass estimation methods, and GSMF measurement techniques, the observed trends are in good qualitative agreement. The characteristic stellar mass $M^\star$ systematically increases from satellite to central galaxies, and from blue to red populations. In both studies, red centrals exhibit the highest values, followed by red satellites, blue centrals, and blue satellites. We find a difference in $M^\star$ of 0.10 dex between centrals and satellites, for both red and blue populations, compared to 0.09 dex and 0.02 dex, respectively, as reported by Peng

et al. (2012). For the low-mass slopes α_2 of the blue populations, we find similar values for blue centrals and satellites. In contrast, Peng et al. (2012) show a shallower and a steeper α_2 for blue centrals and satellites, respectively, indicating a stronger environmental dependence in the low-mass regime. This discrepancy might be attributed to the different fitting procedures: while we adopt a double Schechter function, Peng et al. (2012) use a single Schechter, which potentially influences the derived low-mass slope values. Interestingly, our intermediate-mass slope α_1 for red central galaxies is fully consistent with the value shown by Peng et al. (2012), within the uncertainties, confirming that a single Schechter function adequately describes this subsample. Finally, for the red satellite galaxies, we find that our values of α_1 and α_2 are significantly steeper than those reported by Peng et al. (2012). This indicates a more pronounced decline in the GSMF at both intermediate and low masses in our red satellite population. Nevertheless, we confirm that a double Schechter function remains the most appropriate fit, consistent with Peng et al. (2012).

In their study, Weigel et al. (2016) also find that the total GSMFs of both central and satellite galaxies are better described by a double Schechter function. For centrals, this is due to an excess of high-mass galaxies, which requires an additional high-mass component. Satellites, on the other hand, show a pronounced upturn at the low-mass end, which also requires an additional steeper component. This result is in contrast with Yang et al. (2009), who suggest that the satellite GSMF can be sufficiently fit by a single Schechter function. A direct comparison of the best-fit double Schechter parameters for central and satellite galaxies (Table 7.4) shows overall good agreement between our results and those of Weigel et al. (2016). The characteristic mass $M^\star$ differs by less than 0.05 dex in each subsample. Similarly, α_1 for satellites and α_2 for centrals are consistent within the uncertainties. However, we find a notably higher (i.e. less negative) value of α_1 for central galaxies, indicating a flatter slope at intermediate masses. For satellites, instead, our α_2 is significantly shallower than in Weigel et al. (2016), suggesting a less pronounced upturn at the low-mass end. These differences may be attributed to the different sample selection and group identification method. Nonetheless, the overall agreement in $M^\star$ and the general shape of the GSMFs confirm the consistency of the main trends across both studies.

When splitting both centrals and satellites into blue and red galaxies, Weigel et al. (2016) model all GSMFs using a single Schechter function. This approach is consistent with our results and those of Peng et al. (2012) for centrals and blue satellites, but not red satellites, for which a double Schechter is needed to capture the low-mass upturn. These differences may be attributed to their use of two colour cuts to explicitly define three separate populations (blue, green, and red) rather than just a binary classification. As a result, a significant fraction of objects falls into the green valley, reducing the number densities of both the blue and red samples. This also makes their results not directly comparable to our work or that of Peng et al. (2012), where no green population is explicitly defined. We note that Weigel et al. (2016) adopt a double Schechter function for both green centrals and green satellites. This suggests that the steep low-mass component that we observe in the red satellite subpopulation may instead be captured by their green subsample, making direct comparisons more challenging.

A complementary analysis by Davies et al. (2019b), based on the G^{3}C, investigates the passive fractions of central and satellite galaxies as a function of both stellar and halo mass. By taking the appropriate ratios of the GSMFs presented in Sect. 7.1.2, we are able to reproduce all of their results. Specifically, we confirm that the passive fractions of both centrals and satellites increase

with halo mass when considering all stellar masses, and also increase with stellar mass when considering all halo masses. Moreover, satellites exhibit higher passive fractions than centrals at fixed stellar mass for $\log[M/(M_\odot\, h_{70}^{-2})] < 11$, consistent with the environmental quenching scenario for low-mass satellites. Even when controlling for both stellar and halo mass, we find that satellite galaxies have systematically higher passive fractions than centrals, particularly at low stellar masses and in high-mass halos. These results are expected, as we adopt a similar method for separating star-forming and passive galaxies (see Sect. 4.5). This consistency confirms the robustness of our classification and supports the reliability of our derived GSMFs and their environmental trends.

7.2.3 GSMF dependence on group halo mass

Weigel et al. (2016) also investigate how the GSMF varies as a function of halo mass $M_{\rm halo}$. Although their analysis is based on only three bins, the identified trends are fully consistent with ours. In particular, they report a systematic increase of the characteristic mass $M^\star$ with $M_{\rm halo}$ and, for the low-mass slope α_2, a steepening from low to intermediate halo masses, followed by a shallower slope in the most massive halos. Moreover, they find that a single Schechter function better describes the GSMF in the highest halo mass bin. This confirms the behaviour we also observe, where the intermediate-mass component becomes negligible and the double Schechter fit effectively reduces to a single component. These trends for $M^\star$ and α_2 with $M_{\rm halo}$ are preserved when Weigel et al. (2016) split their sample into red and blue galaxies, although their classification explicitly identifies a green valley population in between. Specifically, they find a systematic increase in $M^\star$ as $M_{\rm halo}$ increases for both red and blue galaxies, with red galaxies still showing higher $M^\star$ values than their blue counterparts at fixed halo mass. Similarly, α_2 shows a steepening from low to intermediate halo masses, followed by a shallower value in the most massive halos. These trends are in excellent agreement with our findings when we divide galaxies into passive/red and star-forming/blue populations. Despite differences in data sets, sample selection, classification methods, and halo mass bins, our results on $M^\star$ and α_2 seem to be generally comparable with those of Weigel et al. (2016) across corresponding halo mass regimes.

In another study, Vázquez-Mata et al. (2020) investigate how the GSMFs of central and satellite galaxies depend on the host DM halo mass, using data from the GAMA survey. Central GSMFs are well described by log-normal functions, especially at high masses, for both blue and red populations. However, at low halo masses, they observe a slight excess of low-mass centrals, indicating that the log-normal function underestimates their abundance in this regime. In contrast, satellite GSMFs are generally well described by single Schechter functions. Nonetheless, at high halo masses, a slight excess of high-mass satellites is observed. Central galaxies show a clear increase in their characteristic stellar mass $M^\star$ with halo mass. At fixed halo mass, red centrals are systematically $\approx$0.2 dex more massive than blue centrals. Similarly, satellite galaxies exhibit an increase in their characteristic stellar mass as halo mass grows. This reflects the mass–richness correlation in galaxy groups, where more massive haloes host both more numerous and more massive satellites. While the general trends are consistent with previous studies, Vázquez-Mata et al. (2020) find a stronger dependence of the characteristic stellar mass of both centrals and satellites on halo mass compared to Yang et al. (2009), likely due to differences in group definitions

and halo mass estimates. In addition, they do not confirm the systematic steepening of the satellite GSMF low-mass slope with halo mass reported by Yang et al. (2009), in either blue or red populations. Instead, they find the steepest slopes in the lowest-mass haloes, suggesting that faint, low-mass satellite galaxies are relatively more abundant in low-mass environments. Finally, they show that the fraction of red galaxies increases with halo mass. Further evidence for environmental quenching comes from the observed increment in the red-to-blue galaxy ratio within groups since $z \sim 0.3$, compared to the field. This suggests that group environments continuously quench SF in infalling galaxies.

Although Vázquez-Mata et al. (2020) model central and satellite GSMFs using different functional forms than those adopted in this work, a meaningful comparison with our results is still possible. First, we confirm the increase of $M^\star$ with $M_{\rm halo}$ for both central and satellite galaxies. Specifically, our $M^\star$ values for satellites in all halo mass bins agree well with those reported by Vázquez-Mata et al. (2020), despite differences in binning and data sets. For centrals, their $M^\star$ values tend to be slightly higher than ours, especially in the most massive halos. Nevertheless, both studies consistently find that, at fixed halo mass, central galaxies are more massive than satellites. Regarding the low-mass end slope, both analyses report a general shallowing of the GSMF with increasing halo mass. In Vázquez-Mata et al. (2020), this trend is not strictly monotonic, as the slope slightly steepens in their highest halo mass bin, but the overall behaviour is still comparable. On the other hand, our α values are systematically steeper across all bins, which may be attributed to our use of a double Schechter function, as well as to differences in binning and data sets.

8 Conclusions and Outlook

In this doctoral thesis, we employed the equatorial GAMA II dataset at $z \leq 0.213$ to construct multiple GSMFs. To this end, we made use of various GAMA data products: stellar masses (Sect. 2.5.1; Taylor et al. 2011; Robotham et al. 2020), the G^{3}C (2.5.2) for the identification of groups (Robotham et al. 2011), the FC (2.5.3) for the identification of the filaments (Alpaslan et al. 2014), and the Hα-derived SFRs (Sect. 2.5.4; Davies et al. 2016). Our magnitude-limited parent galaxy sample (the selection of which is summarised in Table 3.1) consists of 88,093 galaxies and 11,725 groups for Project I, and 82,936 galaxies and 11,579 groups for Project II. In Project I, these numbers are reduced to 50,089 galaxies and 10,429 groups after applying a single redshift-dependent stellar mass limit (5.2). In contrast, in Project II we re-derived the stellar mass limit for each subsample to account for completeness, a refinement that produced results consistent with those obtained using a global selection function.

For our analysis, we employed the Modified Maximum Likelihood (MML) method, as documented in Obreschkow et al. (2018), a Bayesian approach to fitting distribution functions without binning, while accounting for measurement errors, selection effects, and large-scale structure. Implemented via the DFTOOLS package, the MML method iteratively adjusts for observational biases to obtain well-constrained parameters.

Our global GSMF is well described by a double Schechter function with the following parameters: $\log[M^\star/(M_\odot\, h_{70}^{-2})] = 10.76 \pm 0.01$, $\Phi_1^\star = (3.72 \pm 0.09) \times 10^{-3}$ Mpc$^{-3}\, h_{70}^3$, $\alpha_1 = -0.86 \pm 0.03$, $\Phi_2^\star = (0.13 \pm 0.05) \times 10^{-3}$ Mpc$^{-3}\, h_{70}^3$ and $\alpha_2 = -1.72 \pm 0.06$. As shown in Fig. 6.12, our global GSMF agrees well with the GMSFs of prominent previous GAMA and SDSS studies, with the differences being smaller than a factor of 2 over the mass range 10^8 to $3 \times 10^1 1\ M_\odot\, h_{70}^{-2}$.

We began by investigating the variation of the low-redshift GSMF as a function of four different environmental properties: orthogonal distance to the nearest filament, $D_{\perp,\mathrm{min}}$ (in Section 6.1.1), group membership (6.1.2), group halo mass, M_{halo} (6.1.3), and the combination of group branch order BO and group number of connecting links N_{links} (6.1.4).

- We noted first that the GSMF of filament galaxies shows a small change in $M^\star$ as the size of the filaments is varied, whereas the void GSMF does not change its shape at all. In other words, the filament and void mass function do not depend strongly on how big or small we make the filaments (see Fig. 6.1). We did, however, detect a significant difference between the filament and void GSMFs, in each double Schechter function parameter. This difference vanishes though as soon as the grouped galaxies are removed from filament samples, as shown in Fig. 6.2. On the other hand, in Section 6.1.2 we showed that the shape of the GSMF changes significantly between our total group and ungrouped galaxy samples. We therefore concluded that the mass function is not strongly affected by how close (or far) a galaxy is to a filament, but rather by its membership of a group or not. The apparent difference between the filament and void GSMFs is thus entirely attributable to a much

higher fraction of grouped galaxies in filaments compared to voids.

- We thus studied the dependence of the GSMF on group halo mass $M_{\rm halo}$, using both a dynamical and a luminosity-based halo mass estimator. For the dynamical halo mass estimates we found that the characteristic mass of the GSMF, $M^\star$, increases with $M_{\rm halo}$, while the intermediate mass slope, α_1, decreases (cf. Table 6.4 and Fig. 6.7). Furthermore, at the highest halo masses, the intermediate and low mass slopes of the GSMF become very similar, such that the GSMF is best described by a single Schechter function in this halo mass regime. While the results using the luminosity-based halo mass estimator are less conclusive, they are nevertheless consistent with those derived from the dynamical halo mass estimator. Extending this analysis across different galaxy populations, we confirmed that $M^\star$ systematically increases with $M_{\rm halo}$ for passive, star-forming, centrals and satellite galaxies, confirming that more massive halos host more massive galaxies (cf. Fig. 7.8). For α_2, we observed opposite trends in centrals and satellites: it steepens with $M_{\rm halo}$ in centrals, but becomes progressively shallower in satellites, reflecting a relative decline in the number of low-mass satellites in more massive halos. Star-forming and passive galaxies exhibit consistent trends in all double Schechter parameters, though passive galaxies are systematically more massive.

Combining these results, we thus concluded that the GSMF primarily depends on halo mass, while the the larger-scale environment plays a secondary role at best. While this finding is inconsistent with some previous studies (Vulcani et al. 2013; Calvi et al. 2013; Weigel et al. 2016; Guglielmo et al. 2018; Vázquez-Mata et al. 2020), our clear evidence that the most massive halos host the most massive galaxies in particular is clearly consistent with others (Baldry et al. 2006; Vulcani et al. 2012; O'Kane et al. 2024).

Having said that, it would be incorrect to claim that the GSMF is entirely oblivious to the existence of filaments. After all, it is the filament environment in which, to a large extent, the halo mass distribution is established, which in turn determines the distribution of galaxy stellar masses. In this sense, the influence of filaments on the GSMF is simultaneously fundamental and indirect. This picture is further corroborated by our observation that the group GSMF is almost entirely independent of the groups' location within the filamentary structure, as measured by the group branch order and the group number of connecting links, except that the GSMF of highly connected groups is best described by a single Schechter function.

We further deconstructed the low-redshift GSMF by separating galaxies according to their star formation activity and environment, examining how it varies across different galaxy populations (star-forming vs passive galaxies in Sect. 7.1.1, and centrals vs satellites in Sect. 7.1.2) and as a function of halo mass (Sect. 7.1.3).

- We noted first that the GSMFs of star-forming and passive galaxies show distinct shapes: passive galaxies require a double Schechter function to capture the low-mass bump, while the star-forming population appears well approximated by a single Schechter function due to its high-mass cut-off being dominated by the intermediate-mass component. Nonetheless, we find that a double Schechter provides a slightly more accurate description also for the star-forming sample. Our results confirm that the total GSMF is dominated by star-forming galaxies at the low-mass end and by passive galaxies in the intermediate-to-high-mass regime (cf. Fig. 7.1). We also tested the robustness of our star-forming/passive GSMFs

against small variations of the star-forming/passive classification by varying the dividing line in the log M − log SFR plane within its 1σ confidence region. The resulting uncertainties in the double Schechter function parameters were similar or smaller to the random errors, confirming that our results are robust against small perturbations in the classification. Comparing galaxies inside and outside of groups, we found that galaxies in groups have higher $M^\star$ and shallower α_2 for both our star-forming and passive populations, indicating, respectively, that more massive systems preferentially form in groups and that groups host a relatively lower abundance of low-mass galaxies.

- We then examined the GSMFs of central and satellite galaxies. We found that central and ungrouped galaxies dominate the high- and low-mass end of the total GSMF, respectively (cf. Fig. 7.5). $M^\star$ shows a decreasing trend from centrals to satellites to ungrouped galaxies, consistently across the full, star-forming, and passive samples. A similar trend is observed for α_2, with steeper values for isolated systems, although for passive centrals the fit requires only a single Schechter component (cf. Fig. 7.6). Interestingly, α_1 of satellites closely matches that of the total population, suggesting that satellites play a key role in shaping the intermediate-mass regime of the total GSMF. When separating by SF activity, we find that central star-forming and passive galaxies dominate the high-mass ends of their respective GSMFs. In contrast, the low-mass end of the star-forming GSMF is shaped by both satellite and ungrouped galaxies, while that of the passive GSMF is primarily shaped by ungrouped galaxies. These trends confirm and extend the environmental dependencies observed specifically for star-forming and passive systems: galaxies in groups show higher $M^\star$ and shallower α_2 values compared to their ungrouped counterparts.

The only qualitative agreement with the empirical model of Peng et al. (2010) lies in the overall functional form: star-forming galaxies are well described by a single Schechter function (with marginal improvement from a second component), while passive and total populations require a double Schechter function. Beyond this, several key aspects of their model are not supported by our findings. First, $M^\star$ is not constant across different galaxy types or environments. Second, α_2 is significantly steeper for passive galaxies, in contrast to their assumption of similar slopes for star-forming and passive galaxies. The relation $\alpha_{1,\mathrm{P}} - \alpha_{\mathrm{SF}} \approx 1$ holds in our grouped, but not ungrouped environments, suggesting a stronger environmental dependence than originally proposed. Part of the mismatch arises from differences in classification methods, as we rely on Hα-derived SFR measurements rather than photometric colours. While adopting a single Schechter fit for star-forming galaxies reduces some discrepancies, it does not entirely remove them. Additionally, model selection criteria (e.g., LRT; Fig. 7.9) strongly favour a double Schechter function for the star-forming population, confirming that the observed discrepancies with Peng et al. (2010) cannot be attributed to the functional form alone, but rather arise from real deviations from the assumptions of their model.

On the other hand, our results agree well with those of Weigel et al. (2016), particularly for passive galaxies, both in terms of $M^\star$ and α_2. In contrast, the lack of a low-mass upturn in the red GSMF reported by Taylor et al. (2015) is not confirmed in our analysis, which reveals a clear low-mass component in passive galaxies down to $M_\star \sim 10^{8.3}\ M_\odot$.

Our central and satellite populations exhibit distinct mass functions, in agreement with the environmental quenching scenario proposed by Peng et al. (2012). Passive centrals are well

described by a single Schechter function, indicating that their quenching is primarily mass-driven and largely independent of environment. In contrast, passive satellites require a double Schechter function, reflecting an additional low-mass subpopulation quenched by environmental processes. The star-forming populations of both centrals and satellites are generally consistent with a single Schechter form, supporting the universality of mass quenching across different environments. These findings qualitatively agree with previous studies (Peng et al. 2012; Weigel et al. 2016), despite some quantitative differences likely due to methodology and sample selection. Moreover, we reproduce the enhanced passive fractions in satellites at fixed stellar and halo mass observed by Davies et al. (2019b), supporting the importance of environment in suppressing SF. Overall, these findings demonstrate that galaxy environment plays a crucial role in shaping the low-mass end of the GSMF, particularly through satellite quenching, while mass quenching dominates for centrals.

In summary, our comprehensive analysis demonstrates that the low-redshift GSMF is predominantly shaped by the mass of the host DMH. While the large-scale environment, such as filaments and voids, has a secondary influence, its effect is largely indirect, operating through the halo mass distribution. By separating galaxies according to their SF activity and distance from the group centre, we identify distinct quenching mechanisms at play: mass quenching dominates in central galaxies, whereas environmental quenching plays a significant role in shaping the satellite population, particularly at low stellar masses. These results reveal the complex interplay between internal galaxy properties and their surrounding environment in driving galaxy evolution.

Looking ahead, extending this framework to higher redshifts and incorporating additional physical parameters, such as gas content or morphological features, will be crucial to further disentangle the relative contributions of mass and environment across cosmic time, particularly around the peak of cosmic SF activity ($z \sim 2$–3). Achieving this requires deeper spectroscopic surveys and high-quality multi-wavelength photometry to probe fainter galaxies while ensuring accurate stellar mass and SFR measurements. Upcoming facilities, such as the Euclid mission and the Wide Area VISTA Extragalactic Survey (WAVES), will provide wide-field spectroscopy and deep imaging, enabling detailed studies of LSS, halo mass, and low-mass galaxy populations. Complementary radio, millimetre, and FIR observations will allow simultaneous exploration of gas content, SF, and morphological evolution, providing a more complete view of the processes driving galaxy evolution and quenching mechanisms. Advances in statistical methods and modelling will further improve corrections for observational biases and enable direct comparison with simulations. Together, these developments will build on the framework established in this doctoral thesis and allow for a deeper understanding of the interplay between halo mass, environment, and internal galaxy processes across cosmic time.

9 Bibliography

Abazajian, K. N., Adelman-McCarthy, J. K., Agüeros, M. A., et al. 2009, ApJ Suppl., 182, 543

Abbas, U. & Sheth, R. K. 2006, MNRAS, 372, 1749

Adelman-McCarthy, J. K., Agüeros, M. A., Allam, S. S., et al. 2008, ApJ Suppl., 175, 297

Akaike, H. 1974, IEEE Transactions on Automatic Control, 19, 716

Alam, S., Zu, Y., Peacock, J. A., & Mandelbaum, R. 2019, MNRAS, 483, 4501

Alpaslan, M., Driver, S., Robotham, A. S. G., et al. 2015, MNRAS, 451, 3249

Alpaslan, M., Robotham, A. S. G., Driver, S., et al. 2014, MNRAS, 438, 177

Annunziatella, M., Biviano, A., Mercurio, A., et al. 2014, A&A, 571, A80

Aragon Calvo, M. A., Neyrinck, M. C., & Silk, J. 2019, The Open Journal of Astrophysics, 2, 7

Aragón-Calvo, M. A., van de Weygaert, R., & Jones, B. J. T. 2010, MNRAS, 408, 2163

Arnouts, S., Walcher, C. J., Le Fèvre, O., et al. 2007, A&A, 476, 137

Artale, M. C., Zehavi, I., Contreras, S., & Norberg, P. 2018, MNRAS, 480, 3978

Bahé, Y. M. & McCarthy, I. G. 2015, MNRAS, 447, 969

Baldry, I. K., Alpaslan, M., Bauer, A. E., et al. 2014, MNRAS, 441, 2440

Baldry, I. K., Balogh, M. L., Bower, R. G., et al. 2006, MNRAS, 373, 469

Baldry, I. K., Driver, S. P., Loveday, J., et al. 2012, MNRAS, 421, 621

Baldry, I. K., Glazebrook, K., Brinkmann, J., et al. 2004, ApJ, 600, 681

Baldry, I. K., Glazebrook, K., & Driver, S. P. 2008, MNRAS, 388, 945

Baldry, I. K., Liske, J., Brown, M. J. I., et al. 2018, MNRAS, 474, 3875

Baldry, I. K., Robotham, A. S. G., Hill, D. T., et al. 2010, MNRAS, 404, 86

Balogh, M., Eke, V., Miller, C., et al. 2004a, MNRAS, 348, 1355

Balogh, M. L., Baldry, I. K., Nichol, R., et al. 2004b, ApJ Let., 615, L101

Balogh, M. L., McGee, S. L., Mok, A., et al. 2016, MNRAS, 456, 4364

Balogh, M. L. & Morris, S. L. 2000, MNRAS, 318, 703

Barsanti, S., Owers, M. S., Brough, S., et al. 2018, ApJ, 857, 71

Baugh, C. M. 2006, Reports on Progress in Physics, 69, 3101

Behroozi, P. S., Wechsler, R. H., & Conroy, C. 2013, ApJ, 770, 57

Bell, E. F. & de Jong, R. S. 2001, ApJ, 550, 212

Bell, E. F., McIntosh, D. H., Barden, M., et al. 2004a, ApJ Let., 600, L11

Bell, E. F., McIntosh, D. H., Katz, N., & Weinberg, M. D. 2003, ApJ Suppl., 149, 289

Bell, E. F., Wolf, C., Meisenheimer, K., et al. 2004b, ApJ, 608, 752

Bellhouse, C., Jaffé, Y. L., Hau, G. K. T., et al. 2017, ApJ, 844, 49

Bellstedt, S., Driver, S. P., Robotham, A. S. G., et al. 2020a, MNRAS, 496, 3235

Bellstedt, S., Robotham, A. S. G., Driver, S. P., et al. 2020b, MNRAS, 498, 5581

Benson, A. J., Bower, R. G., Frenk, C. S., et al. 2003, ApJ, 599, 38

Berlind, A. A. & Weinberg, D. H. 2002, ApJ, 575, 587

Bharadwaj, S., Bhavsar, S. P., & Sheth, J. V. 2004, ApJ, 606, 25

Bialas, D., Lisker, T., Olczak, C., Spurzem, R., & Kotulla, R. 2015, A&A, 576, A103

Birnboim, Y. & Dekel, A. 2003, MNRAS, 345, 349

Birnboim, Y., Padnos, D., & Zinger, E. 2016, ApJ Let., 832, L4

Blanton, M. R., Eisenstein, D., Hogg, D. W., Schlegel, D. J., & Brinkmann, J. 2005, ApJ, 629, 143

Blanton, M. R., Hogg, D. W., Bahcall, N. A., et al. 2003, ApJ, 594, 186

Bluck, A. F. L., Mendel, J. T., Ellison, S. L., et al. 2016, MNRAS, 462, 2559

Blumenthal, G. R., da Costa, L. N., Goldwirth, D. S., Lecar, M., & Piran, T. 1992, ApJ, 388, 234

Blumenthal, G. R., Faber, S. M., Primack, J. R., & Rees, M. J. 1984, Nature, 311, 517

Bond, J. R., Kofman, L., & Pogosyan, D. 1996, Nature, 380, 603

Bond, J. R. & Myers, S. T. 1996, ApJ Suppl., 103, 1

Borch, A., Meisenheimer, K., Bell, E. F., et al. 2006, A&A, 453, 869

Borzyszkowski, M., Porciani, C., Romano-Díaz, E., & Garaldi, E. 2017, MNRAS, 469, 594

Boselli, A., Fossati, M., & Sun, M. 2022, A&A Rev., 30, 3

Boselli, A. & Gavazzi, G. 2006, PASP, 118, 517

Bower, R. G., Benson, A. J., Malbon, R., et al. 2006, MNRAS, 370, 645

Bower, R. G., McCarthy, I. G., & Benson, A. J. 2008, MNRAS, 390, 1399

Brammer, G. B., Whitaker, K. E., van Dokkum, P. G., et al. 2011, ApJ, 739, 24

Bremer, M. N., Phillipps, S., Kelvin, L. S., et al. 2018, MNRAS, 476, 12

Brinchmann, J., Charlot, S., White, S. D. M., et al. 2004, MNRAS, 351, 1151

Brinchmann, J. & Ellis, R. S. 2000, ApJ Let., 536, L77

Brough, S., Croom, S., Sharp, R., et al. 2013, MNRAS, 435, 2903

Brown, T., Catinella, B., Cortese, L., et al. 2017, MNRAS, 466, 1275

Bulichi, T.-E., Davé, R., & Kraljic, K. 2024, MNRAS, 529, 2595

Bundy, K., Ellis, R. S., & Conselice, C. J. 2005, ApJ, 625, 621

Bundy, K., Ellis, R. S., Conselice, C. J., et al. 2006, ApJ, 651, 120

Calvi, R., Poggianti, B. M., Vulcani, B., & Fasano, G. 2013, MNRAS, 432, 3141

Campbell, D., van den Bosch, F. C., Hearin, A., et al. 2015, MNRAS, 452, 444

Caputi, K. I., Cirasuolo, M., Dunlop, J. S., et al. 2011, MNRAS, 413, 162

Cattaneo, A., Dekel, A., Faber, S. M., & Guiderdoni, B. 2008, MNRAS, 389, 567

Cautun, M., van de Weygaert, R., Jones, B. J. T., & Frenk, C. S. 2014, MNRAS, 441, 2923

Chen, Y.-C., Ho, S., Mandelbaum, R., et al. 2017, MNRAS, 466, 1880

Chester, C. & Roberts, M. S. 1964, AJ, 69, 635

Cimatti, A., Daddi, E., & Renzini, A. 2006, A&A, 453, L29

Colberg, J. M., Krughoff, K. S., & Connolly, A. J. 2005, MNRAS, 359, 272

Cole, S., Lacey, C. G., Baugh, C. M., & Frenk, C. S. 2000, MNRAS, 319, 168

Colless, M., Dalton, G., Maddox, S., et al. 2001, MNRAS, 328, 1039

Conroy, C. & Wechsler, R. H. 2009, ApJ, 696, 620

Conselice, C. J., Blackburne, J. A., & Papovich, C. 2005, ApJ, 620, 564

Cooper, M. C., Gallazzi, A., Newman, J. A., & Yan, R. 2010, MNRAS, 402, 1942

Cooray, A. 2006, MNRAS, 365, 842

Cooray, A. & Sheth, R. 2002, Phys. Rep., 372, 1

Cora, S. A., Vega-Martínez, C. A., Hough, T., et al. 2018, MNRAS, 479, 2

Cox, T. J., Dutta, S. N., Di Matteo, T., et al. 2006, ApJ, 650, 791

Croton, D. J., Farrar, G. R., Norberg, P., et al. 2005, MNRAS, 356, 1155

Croton, D. J., Gao, L., & White, S. D. M. 2007, MNRAS, 374, 1303

Croton, D. J., Springel, V., White, S. D. M., et al. 2006, MNRAS, 365, 11

da Cunha, E., Charmandaris, V., Díaz-Santos, T., et al. 2010, A&A, 523, A78

Daddi, E., Dickinson, M., Morrison, G., et al. 2007a, ApJ, 670, 156

Daddi, E., Dickinson, M., Morrison, G., et al. 2007b, ApJ, 670, 156

Darvish, B., Sobral, D., Mobasher, B., et al. 2014, ApJ, 796, 51

Das, A., Pandey, B., & Sarkar, S. 2023, Research in Astronomy and Astrophysics, 23, 115018

Davé, R., Anglés-Alcázar, D., Narayanan, D., et al. 2019, MNRAS, 486, 2827

Davidzon, I., Bolzonella, M., Coupon, J., et al. 2013, A&A, 558, A23

Davidzon, I., Ilbert, O., Laigle, C., et al. 2017, A&A, 605, A70

Davies, L. J. M., Driver, S. P., Robotham, A. S. G., et al. 2016, MNRAS, 461, 458

Davies, L. J. M., Fuentealba-Fuentes, M. F., Wright, R. J., et al. 2025a, MNRAS, 541, 3220

Davies, L. J. M., Lagos, C. d. P., Katsianis, A., et al. 2019a, MNRAS, 483, 1881

Davies, L. J. M., Robotham, A. S. G., Driver, S. P., et al. 2015, MNRAS, 452, 616

Davies, L. J. M., Robotham, A. S. G., Lagos, C. d. P., et al. 2019b, MNRAS, 483, 5444

Davies, L. J. M., Thorne, J. E., Bellstedt, S., et al. 2025b, MNRAS, 541, 573

Davis, M., Efstathiou, G., Frenk, C. S., & White, S. D. M. 1985, ApJ, 292, 371

De Lucia, G., Poggianti, B. M., Aragón-Salamanca, A., et al. 2004, ApJ Let., 610, L77

De Lucia, G., Springel, V., White, S. D. M., Croton, D., & Kauffmann, G. 2006, MNRAS, 366, 499

de Ravel, L., Kampczyk, P., Le Fèvre, O., et al. 2011, arXiv e-prints, arXiv:1104.5470

Dekel, A. & Birnboim, Y. 2006, MNRAS, 368, 2

Dekel, A., Birnboim, Y., Engel, G., et al. 2009, Nature, 457, 451

Dekel, A. & Rees, M. J. 1994, ApJ Let., 422, L1

Dekel, A. & Silk, J. 1986, ApJ, 303, 39

Di Matteo, T., Springel, V., & Hernquist, L. 2005, Nature, 433, 604

Dickinson, M., Papovich, C., Ferguson, H. C., & Budavári, T. 2003, ApJ, 587, 25

Doroshkevich, A., Tucker, D. L., Allam, S., & Way, M. J. 2004, A&A, 418, 7

Dressler, A. 1980, ApJ, 236, 351

Drinkwater, M. J., Jurek, R. J., Blake, C., et al. 2010, MNRAS, 401, 1429

Driver, S. P., Allen, P. D., Graham, A. W., et al. 2006, MNRAS, 368, 414

Driver, S. P., Bellstedt, S., Robotham, A. S. G., et al. 2022, MNRAS, 513, 439

Driver, S. P., Hill, D. T., Kelvin, L. S., et al. 2011, MNRAS, 413, 971

Driver, S. P., Norberg, P., Baldry, I. K., et al. 2009, Astronomy and Geophysics, 50, 5.12

Driver, S. P., Robotham, A. S. G., Bland-Hawthorn, J., et al. 2013, MNRAS, 430, 2622

Driver, S. P., Wright, A. H., Andrews, S. K., et al. 2016, MNRAS, 455, 3911

Drory, N., Bundy, K., Leauthaud, A., et al. 2009, ApJ, 707, 1595

Drory, N., Salvato, M., Gabasch, A., et al. 2005, ApJ Let., 619, L131

Duncan, K., Conselice, C. J., Mortlock, A., et al. 2014, MNRAS, 444, 2960

Eardley, E., Peacock, J. A., McNaught-Roberts, T., et al. 2015, MNRAS, 448, 3665

Efstathiou, G., Frenk, C. S., White, S. D. M., & Davis, M. 1988, MNRAS, 235, 715

Einasto, M., Kipper, R., Tenjes, P., et al. 2022, A&A, 668, A69

Elbaz, D., Daddi, E., Le Borgne, D., et al. 2007, A&A, 468, 33

Ellis, S. C., Driver, S. P., Allen, P. D., et al. 2005, MNRAS, 363, 1257

Ellison, S. L., Patton, D. R., Mendel, J. T., & Scudder, J. M. 2011, MNRAS, 418, 2043

Ellison, S. L., Patton, D. R., Simard, L., & McConnachie, A. W. 2008, AJ, 135, 1877

Ellison, S. L., Patton, D. R., Simard, L., et al. 2010, MNRAS, 407, 1514

Faber, S. M. 1973, ApJ, 179, 731

Faber, S. M., Willmer, C. N. A., Wolf, C., et al. 2007, ApJ, 665, 265

Fakhouri, O., Ma, C.-P., & Boylan-Kolchin, M. 2010, MNRAS, 406, 2267

Faltenbacher, A. & White, S. D. M. 2010, ApJ, 708, 469

Fang, J. J., Faber, S. M., Koo, D. C., & Dekel, A. 2013, ApJ, 776, 63

Foltz, R., Wilson, G., Muzzin, A., et al. 2018, ApJ, 866, 136

Fontana, A., Pozzetti, L., Donnarumma, I., et al. 2004, A&A, 424, 23

Fontana, A., Salimbeni, S., Grazian, A., et al. 2006, A&A, 459, 745

Fontanot, F., De Lucia, G., Monaco, P., Somerville, R. S., & Santini, P. 2009, MNRAS, 397, 1776

Fossati, M., Fumagalli, M., Boselli, A., et al. 2016, MNRAS, 455, 2028

Galárraga-Espinosa, D., Aghanim, N., Langer, M., & Tanimura, H. 2021, A&A, 649, A117

Gallazzi, A., Charlot, S., Brinchmann, J., White, S. D. M., & Tremonti, C. A. 2005, MNRAS, 362, 41

Gao, L., Springel, V., & White, S. D. M. 2005, MNRAS, 363, L66

Gao, L. & White, S. D. M. 2007, MNRAS, 377, L5

González, R. E. & Padilla, N. D. 2009, MNRAS, 397, 1498

González, V., Labbé, I., Bouwens, R. J., et al. 2011, ApJ Let., 735, L34

Gott, III, J. R., Jurić, M., Schlegel, D., et al. 2005, ApJ, 624, 463

Grazian, A., Fontana, A., Santini, P., et al. 2015, A&A, 575, A96

Grootes, M. W., Tuffs, R. J., Popescu, C. C., et al. 2017, AJ, 153, 111

Guglielmo, V., Poggianti, B. M., Moretti, A., et al. 2015, MNRAS, 450, 2749

Guglielmo, V., Poggianti, B. M., Vulcani, B., et al. 2018, A&A, 620, A7

Gunawardhana, M. L. P., Hopkins, A. M., Bland-Hawthorn, J., et al. 2013, MNRAS, 433, 2764

Gunawardhana, M. L. P., Hopkins, A. M., Sharp, R. G., et al. 2011, MNRAS, 415, 1647

Gunn, J. E. & Gott, III, J. R. 1972, ApJ, 176, 1

Guo, Q., White, S., Li, C., & Boylan-Kolchin, M. 2010, MNRAS, 404, 1111

Gupta, A., Tran, K.-V., Cohn, J., et al. 2020, ApJ, 893, 23

Han, J., Eke, V. R., Frenk, C. S., et al. 2015, MNRAS, 446, 1356

Henriques, B. M. B., White, S. D. M., Thomas, P. A., et al. 2015, MNRAS, 451, 2663

Hirschmann, M., De Lucia, G., Wilman, D., et al. 2014, MNRAS, 444, 2938

Hoosain, M., Blyth, S.-L., Skelton, R. E., et al. 2024, MNRAS, 528, 4139

Hopkins, A. M., Miller, C. J., Nichol, R. C., et al. 2003, ApJ, 599, 971

Hopkins, P. F., Bundy, K., Croton, D., et al. 2010, ApJ, 715, 202

Hopkins, P. F., Cox, T. J., Hernquist, L., et al. 2013, MNRAS, 430, 1901

Hopkins, P. F., Cox, T. J., Kereš, D., & Hernquist, L. 2008, ApJ Suppl., 175, 390

Hopkins, P. F., Cox, T. J., Younger, J. D., & Hernquist, L. 2009, ApJ, 691, 1168

Humason, M. L., Mayall, N. U., & Sandage, A. R. 1956, AJ, 61, 97

Ilbert, O., McCracken, H. J., Le Fèvre, O., et al. 2013, A&A, 556, A55

Ilbert, O., Salvato, M., Le Floc'h, E., et al. 2010, ApJ, 709, 644

Jõeveer, M., Einasto, J., & Tago, E. 1978, MNRAS, 185, 357

Jablonka, J. & Arimoto, N. 1992, A&A, 255, 63

Jaffé, Y. L., Poggianti, B. M., Moretti, A., et al. 2018, MNRAS, 476, 4753

Jeffreys, H. 1939, Theory of Probability

Jiang, F., Dekel, A., Kneller, O., et al. 2019, MNRAS, 488, 4801

Jones, D. H., Read, M. A., Saunders, W., et al. 2009, MNRAS, 399, 683

Kaiser, N. 1984, ApJ Let., 284, L9

Kajisawa, M., Ichikawa, T., Tanaka, I., et al. 2009, ApJ, 702, 1393

Kauffmann, G., Heckman, T. M., White, S. D. M., et al. 2003, MNRAS, 341, 33

Kauffmann, G., White, S. D. M., Heckman, T. M., et al. 2004, MNRAS, 353, 713

Kawinwanichakij, L., Papovich, C., Quadri, R. F., et al. 2017, ApJ, 847, 134

Kelvin, L. S., Driver, S. P., Robotham, A. S. G., et al. 2014, MNRAS, 444, 1647

Kennicutt, Jr., R. C. 1998a, Ann. Rev. A&A, 36, 189

Kennicutt, Jr., R. C. 1998b, ApJ, 498, 541

Kereš, D., Katz, N., Fardal, M., Davé, R., & Weinberg, D. H. 2009, MNRAS, 395, 160

Kereš, D., Katz, N., Weinberg, D. H., & Davé, R. 2005, MNRAS, 363, 2

Kitzbichler, M. G. & White, S. D. M. 2007, MNRAS, 376, 2

Knobel, C., Lilly, S. J., Kovač, K., et al. 2013, ApJ, 769, 24

Knobel, C., Lilly, S. J., Woo, J., & Kovač, K. 2015, ApJ, 800, 24

Kodama, T., Smail, I., Nakata, F., Okamura, S., & Bower, R. G. 2001, ApJ Let., 562, L9

Kovač, K., Lilly, S. J., Knobel, C., et al. 2014, MNRAS, 438, 717

Kraljic, K., Arnouts, S., Pichon, C., et al. 2018, MNRAS, 474, 547

Kuutma, T., Tamm, A., & Tempel, E. 2017, A&A, 600, L6

Lacerna, I. & Padilla, N. 2011, MNRAS, 412, 1283

Lagos, C. d. P., Tobar, R. J., Robotham, A. S. G., et al. 2018, MNRAS, 481, 3573

Laigle, C., Pichon, C., Arnouts, S., et al. 2018, MNRAS, 474, 5437

Lara-López, M. A., Hopkins, A. M., López-Sánchez, A. R., et al. 2013, MNRAS, 434, 451

Larson, R. B. 1974, MNRAS, 169, 229

Larson, R. B. & Tinsley, B. M. 1978, ApJ, 219, 46

Larson, R. B., Tinsley, B. M., & Caldwell, C. N. 1980, ApJ, 237, 692

Lavaux, G. & Wandelt, B. D. 2010, MNRAS, 403, 1392

Lee, K.-S., Ferguson, H. C., Wiklind, T., et al. 2012, ApJ, 752, 66

Lemson, G. & Kauffmann, G. 1999, MNRAS, 302, 111

Li, C. & White, S. D. M. 2009, MNRAS, 398, 2177

Li, H., Wang, H., Mo, H. J., et al. 2023, ApJ, 942, 44

Li, Y., Mo, H. J., & Gao, L. 2008, MNRAS, 389, 1419

Liske, J., Baldry, I. K., Driver, S. P., et al. 2015, MNRAS, 452, 2087

Liske, J., Lemon, D. J., Driver, S. P., Cross, N. J. G., & Couch, W. J. 2003, MNRAS, 344, 307

Madau, P., Ferguson, H. C., Dickinson, M. E., et al. 1996, MNRAS, 283, 1388

Malavasi, N., Arnouts, S., Vibert, D., et al. 2017, MNRAS, 465, 3817

Mannucci, F., Cresci, G., Maiolino, R., Marconi, A., & Gnerucci, A. 2010, MNRAS, 408, 2115

Marasco, A., Crain, R. A., Schaye, J., et al. 2016, MNRAS, 461, 2630

Marchesini, D., van Dokkum, P. G., Förster Schreiber, N. M., et al. 2009a, ApJ, 701, 1765

Marchesini, D., van Dokkum, P. G., Förster Schreiber, N. M., et al. 2009b, ApJ, 701, 1765

Marinoni, C. & Hudson, M. J. 2002, ApJ, 569, 101

McGee, S. L., Bower, R. G., & Balogh, M. L. 2014, MNRAS, 442, L105

McIntosh, D. H., Guo, Y., Hertzberg, J., et al. 2008, MNRAS, 388, 1537

Menci, N., Fontana, A., Giallongo, E., Grazian, A., & Salimbeni, S. 2006, ApJ, 647, 753

Mo, H., van den Bosch, F., & White, S. 2010, Frontmatter (Cambridge University Press), i–iv

Mo, H. J. & White, S. D. M. 1996, MNRAS, 282, 347

Mo, H. J., Yang, X., van den Bosch, F. C., & Jing, Y. P. 2004, MNRAS, 349, 205

Moffett, A. J., Ingarfield, S. A., Driver, S. P., et al. 2016a, MNRAS, 457, 1308

Moffett, A. J., Ingarfield, S. A., Driver, S. P., et al. 2016b, MNRAS, 457, 1308

Moffett, A. J., Lange, R., Driver, S. P., et al. 2016c, MNRAS, 462, 4336

Moore, B., Katz, N., Lake, G., Dressler, A., & Oemler, A. 1996, Nature, 379, 613

Moore, B., Lake, G., Quinn, T., & Stadel, J. 1999, MNRAS, 304, 465

Mortlock, A., Conselice, C. J., Bluck, A. F. L., et al. 2011, MNRAS, 413, 2845

Moster, B. P., Somerville, R. S., Maulbetsch, C., et al. 2010, ApJ, 710, 903

Moustakas, J., Coil, A. L., Aird, J., et al. 2013, ApJ, 767, 50

Muldrew, S. I., Croton, D. J., Skibba, R. A., et al. 2012, MNRAS, 419, 2670

Musso, M., Cadiou, C., Pichon, C., et al. 2018, MNRAS, 476, 4877

Muzzin, A., Marchesini, D., Stefanon, M., et al. 2013, ApJ, 777, 18

Naab, T., Johansson, P. H., & Ostriker, J. P. 2009, ApJ Let., 699, L178

Nandra, K., Georgakakis, A., Willmer, C. N. A., et al. 2007, ApJ Let., 660, L11

Nantais, J. B., Muzzin, A., van der Burg, R. F. J., et al. 2017, MNRAS, 465, L104

Nantais, J. B., van der Burg, R. F. J., Lidman, C., et al. 2016, A&A, 592, A161

Navarro, J. F., Abadi, M. G., & Steinmetz, M. 2004, ApJ Let., 613, L41

Navarro, J. F., Frenk, C. S., & White, S. D. M. 1997, ApJ, 490, 493

Netzer, H. 2009, MNRAS, 399, 1907

Noeske, K. G., Weiner, B. J., Faber, S. M., et al. 2007, ApJ Let., 660, L43

Novikov, D., Colombi, S., & Doré, O. 2006, MNRAS, 366, 1201

Obreschkow, D., Murray, S. G., Robotham, A. S. G., & Westmeier, T. 2018, MNRAS, 474, 5500

O'Kane, C. J., Kuchner, U., Gray, M. E., & Aragón-Salamanca, A. 2024, MNRAS

Oppenheimer, B. D., Davé, R., Kereš, D., et al. 2010, MNRAS, 406, 2325

Pan, D. C., Vogeley, M. S., Hoyle, F., Choi, Y.-Y., & Park, C. 2012, MNRAS, 421, 926

Pandey, B. & Sarkar, S. 2020, MNRAS, 498, 6069

Pannella, M., Hopp, U., Saglia, R. P., et al. 2006, ApJ Let., 639, L1

Panter, B., Heavens, A. F., & Jimenez, R. 2004, MNRAS, 355, 764

Papovich, C., Bassett, R., Lotz, J. M., et al. 2012, ApJ, 750, 93

Papovich, C., Kawinwanichakij, L., Quadri, R. F., et al. 2018, ApJ, 854, 30

Parente, M., Ragone-Figueroa, C., López, P., et al. 2024, ApJ, 966, 154

Park, C., Choi, Y.-Y., Kim, J., et al. 2012, ApJ Let., 759, L7

Pasha, I., Mandelker, N., van den Bosch, F. C., Springel, V., & van de Voort, F. 2023, MNRAS, 520, 2692

Patton, D. R., Torrey, P., Ellison, S. L., Mendel, J. T., & Scudder, J. M. 2013, MNRAS, 433, L59

Paz, D. J., Stasyszyn, F., & Padilla, N. D. 2008, MNRAS, 389, 1127

Peng, Y., Maiolino, R., & Cochrane, R. 2015, Nature, 521, 192

Peng, Y.-j., Lilly, S. J., Kovač, K., et al. 2010, ApJ, 721, 193

Peng, Y.-j., Lilly, S. J., Renzini, A., & Carollo, M. 2012, ApJ, 757, 4

Pérez-González, P. G., Rieke, G. H., Villar, V., et al. 2008, ApJ, 675, 234

Pillepich, A., Springel, V., Nelson, D., et al. 2018, MNRAS, 473, 4077

Pimbblet, K. A. 2005, MNRAS, 358, 256

Pimbblet, K. A., Drinkwater, M. J., & Hawkrigg, M. C. 2004, Monthly Notices of the Royal Astronomical Society, 354, L61

Planck Collaboration, Ade, P. A. R., Aghanim, N., et al. 2016, A&A, 594, A13

Plionis, M., Basilakos, S., & Ragone-Figueroa, C. 2006, ApJ, 650, 770

Poggianti, B. M., Moretti, A., Gullieuszik, M., et al. 2017, ApJ, 844, 48

Pogosyan, D., Bond, J. R., Kofman, L., & Wadsley, J. 1996, in American Astronomical Society Meeting Abstracts, Vol. 189, American Astronomical Society Meeting Abstracts, 13.03

Pozzetti, L., Bolzonella, M., Lamareille, F., et al. 2007, A&A, 474, 443

Pozzetti, L., Bolzonella, M., Zucca, E., et al. 2010, A&A, 523, A13

Press, W. H. & Schechter, P. 1974, ApJ, 187, 425

Quadri, R. F., Williams, R. J., Franx, M., & Hildebrandt, H. 2012, ApJ, 744, 88

Ramachandra, N. S. & Shandarin, S. F. 2015, MNRAS, 452, 1643

Ramakrishnan, S., Paranjape, A., Hahn, O., & Sheth, R. K. 2019, MNRAS, 489, 2977

Reeves, A. M. M., Balogh, M. L., van der Burg, R. F. J., et al. 2021, MNRAS, 506, 3364

Roberts, M. S. & Haynes, M. P. 1994, Ann. Rev. A&A, 32, 115

Robotham, A., Driver, S. P., Norberg, P., et al. 2010a, PASA, 27, 76

Robotham, A., Phillipps, S., & De Propris, R. 2008, ApJ, 672, 834

Robotham, A., Phillipps, S., & de Propris, R. 2010b, MNRAS, 403, 1812

Robotham, A., Wallace, C., Phillipps, S., & De Propris, R. 2006, ApJ, 652, 1077

Robotham, A. S. G., Bellstedt, S., Lagos, C. d. P., et al. 2020, MNRAS, 495, 905

Robotham, A. S. G., Davies, L. J. M., Driver, S. P., et al. 2018, MNRAS, 476, 3137

Robotham, A. S. G., Driver, S. P., Davies, L. J. M., et al. 2014, MNRAS, 444, 3986

Robotham, A. S. G., Norberg, P., Driver, S. P., et al. 2011, MNRAS, 416, 2640

Rodríguez-Medrano, A. M., Springel, V., Stasyszyn, F. A., & Paz, D. J. 2024, MNRAS, 528, 2822

Rodríguez-Puebla, A., Avila-Reese, V., Yang, X., et al. 2015, ApJ, 799, 130

Roediger, E. & Brüggen, M. 2007, MNRAS, 380, 1399

Rudnick, G., Rix, H.-W., Franx, M., et al. 2003, ApJ, 599, 847

Ruggiero, R. & Lima Neto, G. B. 2017, MNRAS, 468, 4107

Sandage, A., Tammann, G. A., & Yahil, A. 1979, ApJ, 232, 352

Santini, P., Fontana, A., Grazian, A., et al. 2012, A&A, 538, A33

Sarron, F., Adami, C., Durret, F., & Laigle, C. 2019, A&A, 632, A49

Saunders, W., Bridges, T., Gillingham, P., et al. 2004, in Society of Photo-Optical Instrumentation Engineers (SPIE) Conference Series, Vol. 5492, Ground-based Instrumentation for Astronomy, ed. A. F. M. Moorwood & M. Iye, 389–400

Schaefer, A. L., Croom, S. M., Allen, J. T., et al. 2017, MNRAS, 464, 121

Schaefer, A. L., Croom, S. M., Scott, N., et al. 2019, MNRAS, 483, 2851

Scharré, L., Sorini, D., & Davé, R. 2024, MNRAS, 534, 361

Schaye, J., Crain, R. A., Bower, R. G., et al. 2015, MNRAS, 446, 521

Schaye, J., Kugel, R., Schaller, M., et al. 2023, MNRAS, 526, 4978

Schechter, P. 1976, ApJ, 203, 297

Schmidt, M. 1968, ApJ, 151, 393

Schwarz, G. 1978, Annals of Statistics, 6, 461

Shankar, F., Lapi, A., Salucci, P., De Zotti, G., & Danese, L. 2006, ApJ, 643, 14

Sharp, R., Saunders, W., Smith, G., et al. 2006, in Society of Photo-Optical Instrumentation Engineers (SPIE) Conference Series, Vol. 6269, Ground-based and Airborne Instrumentation for Astronomy, ed. I. S. McLean & M. Iye, 62690G

Shen, S., Mo, H. J., White, S. D. M., et al. 2003, MNRAS, 343, 978

Sheth, R. K. & van de Weygaert, R. 2004, MNRAS, 350, 517

Singh, A., Mahajan, S., & Bagla, J. S. 2020, MNRAS, 497, 2265

Smith, G. A., Saunders, W., Bridges, T., et al. 2004, in Society of Photo-Optical Instrumentation Engineers (SPIE) Conference Series, Vol. 5492, Ground-based Instrumentation for Astronomy, ed. A. F. M. Moorwood & M. Iye, 410–420

Sobral, D., Best, P. N., Smail, I., et al. 2011, MNRAS, 411, 675

Somerville, R. S. & Davé, R. 2015, Ann. Rev. A&A, 53, 51

Somerville, R. S., Hopkins, P. F., Cox, T. J., Robertson, B. E., & Hernquist, L. 2008, MNRAS, 391, 481

Song, H., Laigle, C., Hwang, H. S., et al. 2021, MNRAS, 501, 4635

Sotillo-Ramos, D., Lara-López, M. A., Pérez-García, A. M., et al. 2021, MNRAS, 508, 1817

Springel, V., White, S. D. M., Jenkins, A., et al. 2005, Nature, 435, 629

Stevens, A. R. H. & Brown, T. 2017, MNRAS, 471, 447

Strateva, I., Ivezić, Ž., Knapp, G. R., et al. 2001, AJ, 122, 1861

Strauss, M. A., Weinberg, D. H., Lupton, R. H., et al. 2002, AJ, 124, 1810

Taylor, E. N., Hopkins, A. M., Baldry, I. K., et al. 2015, MNRAS, 446, 2144

Taylor, E. N., Hopkins, A. M., Baldry, I. K., et al. 2011, MNRAS, 418, 1587

Teimoorinia, H., Bluck, A. F. L., & Ellison, S. L. 2016, MNRAS, 457, 2086

Tempel, E. & Libeskind, N. I. 2013, ApJ Let., 775, L42

Thacker, R. J., MacMackin, C., Wurster, J., & Hobbs, A. 2014, MNRAS, 443, 1125

Tinker, J. L., Leauthaud, A., Bundy, K., et al. 2013, ApJ, 778, 93

Tojeiro, R., Eardley, E., Peacock, J. A., et al. 2017, MNRAS, 470, 3720

Tomczak, A. R., Quadri, R. F., Tran, K.-V. H., et al. 2014, ApJ, 783, 85

Tonry, J. L., Blakeslee, J. P., Ajhar, E. A., & Dressler, A. 2000, ApJ, 530, 625

Toomre, A. 1977, in Evolution of Galaxies and Stellar Populations, ed. B. M. Tinsley & D. C. Larson, Richard B. Gehret, 401

Tran, K.-V. H., Papovich, C., Saintonge, A., et al. 2010, ApJ Let., 719, L126

Tremonti, C. A., Moustakas, J., & Diamond-Stanic, A. M. 2007, ApJ Let., 663, L77

Treyer, M., Kraljic, K., Arnouts, S., et al. 2018, MNRAS, 477, 2684

Trussler, J., Maiolino, R., Maraston, C., et al. 2020, MNRAS, 491, 5406

Tully, R. B., Mould, J. R., & Aaronson, M. 1982, ApJ, 257, 527

Tuominen, T., Nevalainen, J., Tempel, E., et al. 2021, A&A, 646, A156

van de Sande, J., Croom, S. M., Bland-Hawthorn, J., et al. 2021, MNRAS, 508, 2307

van den Bosch, F. C., Aquino, D., Yang, X., et al. 2008, MNRAS, 387, 79

van den Bosch, F. C., Yang, X., Mo, H. J., et al. 2007, MNRAS, 376, 841

van der Burg, R. F. J., McGee, S., Aussel, H., et al. 2018, A&A, 618, A140

van der Burg, R. F. J., Muzzin, A., Hoekstra, H., et al. 2013, A&A, 557, A15

van der Wel, A. 2008, ApJ Let., 675, L13

Vázquez-Mata, J. A., Loveday, J., Riggs, S. D., et al. 2020, MNRAS, 499, 631

Viola, M., Cacciato, M., Brouwer, M., et al. 2015, MNRAS, 452, 3529

Vulcani, B., Poggianti, B. M., Fasano, G., et al. 2012, MNRAS, 420, 1481

Vulcani, B., Poggianti, B. M., Moretti, A., et al. 2019, MNRAS, 487, 2278

Vulcani, B., Poggianti, B. M., Oemler, A., et al. 2013, A&A, 550, A58

Wagner, C. R., Courteau, S., Brodwin, M., et al. 2017, ApJ, 834, 53

Wake, D. A., van Dokkum, P. G., & Franx, M. 2012, ApJ Let., 751, L44

Wang, E., Wang, H., Mo, H., et al. 2018a, ApJ, 860, 102

Wang, E., Wang, H., Mo, H., et al. 2018b, ApJ, 864, 51

Wang, L., Weinmann, S. M., De Lucia, G., & Yang, X. 2013, MNRAS, 433, 515

Wang, W., Wang, P., Guo, H., et al. 2024, MNRAS, 532, 4604

Wechsler, R. H., Zentner, A. R., Bullock, J. S., Kravtsov, A. V., & Allgood, B. 2006, ApJ, 652, 71

Weigel, A. K., Schawinski, K., & Bruderer, C. 2016, MNRAS, 459, 2150

Weinmann, S. M., Kauffmann, G., van den Bosch, F. C., et al. 2009, MNRAS, 394, 1213

Weinmann, S. M., van den Bosch, F. C., Yang, X., & Mo, H. J. 2006, MNRAS, 366, 2

Wetzel, A. R., Tinker, J. L., & Conroy, C. 2012, MNRAS, 424, 232

Wetzel, A. R., Tinker, J. L., Conroy, C., & van den Bosch, F. C. 2013, MNRAS, 432, 336

White, S. D. M. & Frenk, C. S. 1991, ApJ, 379, 52

White, S. D. M. & Rees, M. J. 1978, MNRAS, 183, 341

Williams, R. J., Quadri, R. F., Franx, M., van Dokkum, P., & Labbé, I. 2009, ApJ, 691, 1879

Winkel, N., Pasquali, A., Kraljic, K., et al. 2021, MNRAS, 505, 4920

Wolf, C., Aragón-Salamanca, A., Balogh, M., et al. 2009, MNRAS, 393, 1302

Woo, J., Dekel, A., Faber, S. M., & Koo, D. C. 2015, MNRAS, 448, 237

Woo, J., Dekel, A., Faber, S. M., et al. 2013, MNRAS, 428, 3306

Wright, A. H., Robotham, A. S. G., Bourne, N., et al. 2016, MNRAS, 460, 765

Wright, A. H., Robotham, A. S. G., Driver, S. P., et al. 2017, MNRAS, 470, 283

Xu, X., Zehavi, I., & Contreras, S. 2021, MNRAS, 502, 3242

Yang, X., Mo, H. J., & van den Bosch, F. C. 2003, MNRAS, 339, 1057

Yang, X., Mo, H. J., & van den Bosch, F. C. 2009, ApJ, 695, 900

Yang, X., Mo, H. J., van den Bosch, F. C., et al. 2007, ApJ, 671, 153

Yang, X., Zhang, Y., Lu, T., et al. 2017, ApJ, 848, 60

York, D. G., Adelman, J., Anderson, John E., J., et al. 2000, AJ, 120, 1579

Zehavi, I., Contreras, S., Padilla, N., et al. 2018, ApJ, 853, 84

Zel'dovich, Y. B. 1970, A&A, 5, 84

Zentner, A. R., Hearin, A., van den Bosch, F. C., Lange, J. U., & Villarreal, A. S. 2019, MNRAS, 485, 1196

Zhang, Y., Yang, X., Faltenbacher, A., et al. 2009, ApJ, 706, 747

Zhang, Y., Yang, X., Wang, H., et al. 2015, ApJ, 798, 17

Zhang, Y., Yang, X., Wang, H., et al. 2013, ApJ, 779, 160

Zheng, H., Bose, S., Frenk, C. S., et al. 2024, MNRAS, 528, 7300

Zheng, Z., Berlind, A. A., Weinberg, D. H., et al. 2005, ApJ, 633, 791

Zinger, E., Dekel, A., Kravtsov, A. V., & Nagai, D. 2018, MNRAS, 475, 3654